The fabrication of a high temperature superconducting magnet and critical current characterisation of the component Bi(_2)Sr(_2)Ca(_2)Cu(_3)O(_x) tapes and filaments in high magnetic fields

Adrian Bernard Sneary

How to cite:

Sneary, Adrian Bernard (2000) The fabrication of a high temperature superconducting magnet and critical current characterisation of the component Bi(_2)Sr(_2)Ca(_2)Cu(_3)O(_x) tapes and filaments in high magnetic fields. Doctoral thesis, Durham University.

The Fabrication of a High Temperature Superconducting Magnet and Critical Current Characterisation of the Component $Bi_2Sr_2Ca_2Cu_3O_x$ Tapes and Filaments in High Magnetic Fields

Adrian Bernard Sneary

A thesis submitted in partial fulfilment of the requirements for the degree of Doctor of Philosophy

Department of Physics
University of Durham
2000

Abstract

The transport critical current density (J_c) of a 37 filament Bi-2223/Ag tape has been measured as a function of field and temperature from 4.2 K up to 90 K. Data have been obtained over a large current range from 10 mA up to 100 A and in fields up to 23 T with the tape in 3 orientations with respect to field. These comprehensive data have been used to test the predictions of the flux creep and weak link models used to explain J_c in Bi-2223 tapes.

The $J_c(B,T)$ dependence of optimised Bi-2223 tapes has been calculated using a curved film model. The model assumes perfect grain connectivity and that the local superconducting properties are equivalent to those in the best reported thin films. A comparison between the calculations and measured $J_c(B,T)$ dependencies suggest that in high fields at 20 K, J_c in presently available industrially processed tapes is only a factor of 8 below the performance of ideal fully optimised tapes.

Transport measurements have been made on Bi-2223 single filaments extracted from an alloy sheathed multifilamentary tape in liquid nitrogen at 77 K in fields up to 300 mT with the field aligned parallel and perpendicular to the a-b planes. Further $J_c(B,T)$ data have been taken in a variable temperature insert at temperatures between 60 to 90 K in fields up to 15 T. In a study of the electric field-current density (E-J) characteristics of the c-axis orientated data at 77 K, negative curvature is observed in traces below 280 mT. However, the 280 mT trace exhibits both positive and negative curvature in different current regimes in contrast to the predictions of standard theory.

A laboratory scale Bi-2223 superconducting magnet producing a maximum field of 1.29 T at 4.2 K has been designed and fabricated. The magnet comprises 6 resin impregnated double wound pancakes with a 40 mm bore fabricated via the react and wind route. Critical current density measurements have been made as a function of magnetic field, angle and strain at 4.2 K and 77 K on short samples of the constituent tape. The E-J characteristics of all component coils have been measured and a comparison with short sample data shows that minimal additional damage occurred beyond that produced by the bending strain on the tape and the long length variation in J_c. Sufficient detail is provided for the non-specialist to assess the potential use of brittle superconducting tapes for magnet technology and construct a laboratory scale magnet.

Declaration and Copyright

I hereby declare that the work contained within this thesis is my own original work and nothing that is the result of collaboration unless otherwise stated. No part of this thesis has been submitted for a degree or other qualification at this or any other university.

A.B. Sneary, December 2000

Acknowledgements

Throughout the course of this study many people have provided invaluable assistance and I welcome this opportunity to express my gratitude.

Above all, I am indebted to my supervisor, Dr DP Hampshire, for his constant guidance, support and enthusiasm during my PhD and for providing an excellent working environment. I thank the Engineering and Physical Sciences Research Council and BICC General for providing financial support through the CASE award scheme and Professors BK Tanner and MR Pennington for allowing me the use of the Department of Physics facilities. I would also like to thank my industrial supervisor Dr CM Friend for his interest in this work and for supplying the Bi-2223 tape used in this thesis.

I would like to thank Harry Jones and Pete Richens from Oxford University for their advice on coil winding and Richard Prowse for technical support during my placement at BICC General. My thanks go to JC Vallier for allowing me use of the High Field Facility in Grenoble. I also thank Phil Armstrong, George Teasdale, Steve Lishman and all the mechanical workshop staff for their professional workmanship, Mike Lee and Vicki Greener in the Audio-Visual group and Pauline Russel for excellent technical drawings. I would like to acknowledge Karen Brazier for her help with Maple V, Dr AW Brinkman and Andrew Yates helping with gold sputtering, Norman Thompson, John Dobson and Davey Pattinson for technical support and Doctors Tom Hase and Ian Daniel for always being happy to help.

I would also like to thank Simon Keys, Nigel Leigh, Dan Read and Mike Beasley for making the long working hours bearable and all my other friends and colleagues who have made my time in Durham most enjoyable; Andrea Li Bassi, John Clarke, Brian Fulthorpe, Nancy-Ann Hackman, Najib Cheggour, Gwyn Ashcroft, Stuart Dailey, Nicola Morley, Hongjun Niu, George Carty and David Taylor.

Contents

Chapter 1

Introduction

Superconductivity is a fascinating area of science with materials exhibiting zero resistance and macroscopic quantum properties. However the interest in superconducting materials extends far beyond the research laboratory with the materials being an integral part of many commercial applications including magnetic resonance imaging (MRI) and nuclear magnetic resonance (NMR) technology. The high current densities and zero resistance of these materials facilitate the production of high, stable and uniform magnetic fields using low power consumption. The Nobel Prize winning discovery of the high temperature superconducting oxides in the 1980s created the possibility for superconducting applications operating at liquid nitrogen temperatures. Problems associated with the high temperature superconductors (HTS) include their brittle nature and high degree of anisotropy of the superconducting parameters.

Significant advances in HTS tape processing have resulted in critical current densities as high as 6.9 x 10^4 A.cm^{-2} being reported in short samples of Bi-2223 tapes. Further increases in the current density of these materials will require an understanding of the factors determining the critical current density (J_c) within the microstructure. Many models have been proposed in the literature to predict the mechanisms determining J_c. However the implications of these models can only be rigorously tested through comprehensive studies of the field, temperature and angular dependencies of J_c of these materials. Measurement of the superconducting parameters within tapes is further complicated by the ohmic contribution from the low resistance sheath. The true superconducting properties can most reliably be measured using single filaments extracted from the tapes. $J_c(B,T,\theta)$ measurements also facilitate a comparison between the present performance and the potential performance of the materials as measured in thin films and provide predictions of the practical uses of the superconductor.

Presently the main commercial application of superconductors is magnets for MRI. The design and fabrication of superconducting magnet systems is a specialist science with the strong J_c dependencies on strain, angle and magnitude of applied field and anisotropy having important implications on the performance of the system. The majority of superconducting magnets are currently produced using low temperature superconductors. However HTS technology is rapidly emerging with high performance tapes being produced over kilometre lengths and cryocooled magnets generating fields up to 7.25 T at 20 K. As HTS technology becomes more widely available the opportunity for compact laboratory scale magnet systems operating between 1 – 5 T will become increasingly attractive for the research community.

This thesis studies the $J_c(B,T)$ dependence of multifilamentary Bi-2223 superconducting tapes and filaments up to T_c in high magnetic fields and describes the design, fabrication and performance of a 1.29 T Bi-2223 magnet operating at 4.2 K. The fundamental theories of superconductivity are presented in Chapter 2 before a more detailed description of the theories associated with the high temperature superconducting materials in Chapter 3. Comprehensive $J_c(B,T)$ data has been taken on short samples of Bi-2223 tapes at temperatures between 4.2 and 90 K in fields up to 15 T with the tape in 3 orientations with respect to field. These state of the art data are presented in Chapter 4 including a preliminary analysis. In Chapter 5 the electric field – current density (E-J) characteristics of single filaments extracted from the Bi-2223 tape are studied at 77 K as a function of field and angle. $J_c(B,T)$ data on the same samples are also presented in this chapter at high temperatures and fields. In Chapter 6 the $J_c(B,T)$ tape measurements from Chapter 4 are analysed in terms of the flux-creep and weak link diffraction models. Calculations of $J_c(B,T)$ of a Bi-2223 curved film are also presented in Chapter 6. These calculations predict the performance of a Bi-2223 superconductor comprising perfectly connected grains of thin film quality for different levels of grain alignment. These calculations represent the maximum obtainable performance of Bi-2223 tapes assuming that state of the art thin films represent the optimum superconducting parameters. These calculations are compared with the tape J_c values to assess the quality of the grains, grain alignment and grain boundaries in industrially manufactured tapes. The calculations also offer an insight into the potential use of these materials in high field applications.

An introduction to design and fabrication considerations of superconducting magnets is presented in Chapter 7. In Chapter 8 the fabrication and performance of a first generation HTS magnet is presented. The magnet was constructed from 6 double wound pancakes with a bore diameter of 98 mm via the react and wind route. Details of the electrical performance at 4.2 and 77 K and an introductory study of the factors limiting the maximum field are presented. The experience and technological knowledge gained from the first generation magnet facilitated the design and fabrication of a state of the art Bi-2223 magnet system producing 1.29 T at 4.2 K presented in Chapter 9. A detailed description of the design issues and fabrication procedure are presented detailing the choices available in fabricating a laboratory sized system for varying operational requirements. All component sections of the magnet were electrically tested at 4.2 and 77 K. A series of short sample $J_c(B,\theta,\varepsilon)$ measurements of the constituent tape taken at 4.2 K and field profile calculations have facilitated a comparison between the measured and predicted performance of the magnet system. This comparison showed that no damage was caused to the conductor above that due to the bending strain incurred on the tape during the react and wind process. Some suggestions for future work are presented in Chapter 10.

Chapter 2

Superconductivity

2.1 Introduction

This chapter introduces the superconducting state and the fundamental theories of superconductivity. A brief description of the discovery of the superconducting phase is presented before the properties characterising a superconducting material. The critical parameters are discussed in Section 2.4 and the difference between Type I and Type II superconductors are explained in Section 2.5. The macroscopic theory of superconductivity is presented in Section 2.7 and the microscopic theories of London and Ginzburg-Landau are presented in Sections 2.8 and 2.9 respectively. Theories more specific to high temperature superconductors can be found in Chapter 3 of this thesis.

2.2 Discovery of Superconductivity

Having liquefied Helium [1], Onnes investigated the resistance of metals at temperatures approaching absolute zero. In 1911 he observed the resistance of mercury dropped discontinuously to zero at 4.19 K [2]. He later named this the superconductive state.

Many elements and compounds have been found to possess superconducting properties but until 1986 superconductivity was thought to be a low temperature phenomenon. In 1986 a new class of superconductor was discovered containing copper oxide planes [3]. In 1987 $YBa_2Cu_3O_{7-\delta}$ (YBCO) was the first material found to have a superconducting transition temperature (T_c) above the boiling point of nitrogen [4].

2.3 Zero resistance and the Meissner State

The first fundamental property of a superconductor is the disappearance of dc electrical resistance below T_c. Persistent current experiments have produced resistances at least 10^{10} times lower than copper at room temperature in both low temperature [5] and copper oxide superconductors [6,7].

The second fundamental property is the complete exclusion of flux from the bulk of the conductor when cooled from the normal state to below the critical temperature in a small magnetic field. This perfect diamagnetism was first observed in 1933 and is called the Meissner effect [8].

2.4 Critical Parameters

Superconductivity is destroyed above the characteristic critical temperature (T_c). All superconductors have a characteristic critical field, B_c for Type I superconductors and B_{c2} for Type II superconductors. Superconductivity can only exist in fields below these values. Finally the superconducting state can only support currents below the critical current density (J_c).

2.5 Type I and Type II Superconductors

Superconductors can be divided into two classes depending on the way in which the superconducting to normal transition proceeds with increasing field below T_c.

A Type I superconductor remains in the Meissner state in a background field below its characteristic critical field (B_c). On increasing the field above B_c magnetic flux completely penetrates the sample and the normal state resistance of the sample returns. Above B_c the internal field is equal to the external field and the magnetic moment of the sample is zero.

In a Type II superconductor the magnetic field is completely excluded up to the characteristic lower critical field (B_{c1}). At B_{c1} magnetic flux penetrates the sample in

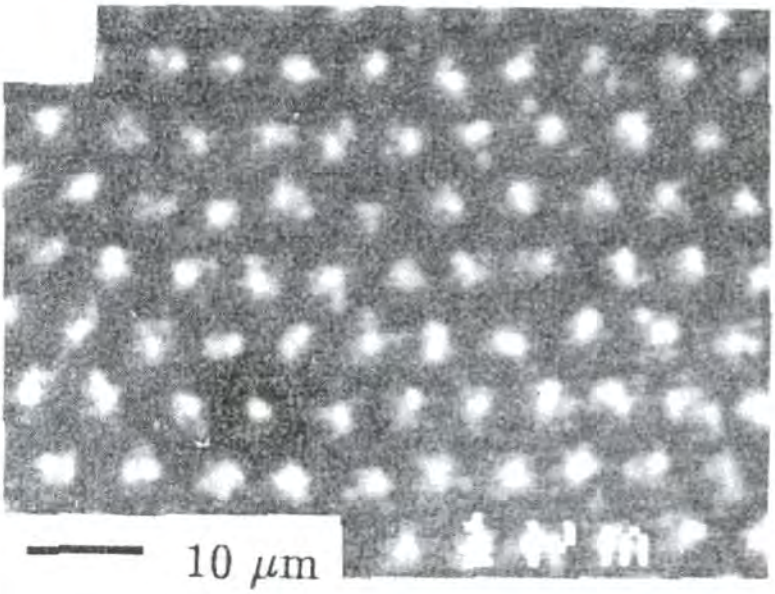

Figure 2.1 A Bitter pattern showing the vortices in a $Bi_2Sr_2Ca_2Cu_3O_{8+x}$ single crystal[9].

the form of quantised flux lines producing a mixed state of superconducting and normal regions within the bulk of the sample. The sample remains in the mixed state until the upper critical field (B_{c2}) when the sample returns to its normal state. All commercially useful superconductors are of the Type II variety.

2.6 Flux lines and the Shubnikov Phase

In 1957 Abikosov [10] proposed that for a Type II superconductor in a field between B_{c1} and B_{c2} magnetic flux penetrates the sample in the form of quantised flux lines or vortices. The sample is said to be in the Shubnikov or mixed phase. These flux lines are vortices of normal conducting material within the superconductor and are arranged in a regular lattice. To minimise free energy the flux lines position themselves at the corners of equilateral triangles as shown in Figure 2.1. The amount of flux associated with each vortex is

$$\Phi_0 = \frac{h}{2e} = 2.07 \times 10^{-15}\,Tm^2 \qquad \textbf{(2.1)}$$

2.7 BCS Theory

In 1957, Bardeen, Cooper and Schrieffer (BCS) proposed a microscopic theory to explain superconductivity [11]. The theory is based on electrons interacting via the lattice [12,13].

When an electron passes in close proximity to a positively charged ion there is a momentary attraction which modifies the vibration of the ion. The ion may then interact with another electron producing a net attraction between the electrons via a virtual phonon. Cooper had previously postulated that an attractive force between two electrons would bind the electrons in a pair at temperatures approaching absolute zero [14]. These bound electrons are referred to as Cooper pairs and interact over a distance of the BCS coherence length (ξ_{co}) of typical dimension 10^2 nm to 10^3 nm. Electrons in a Cooper pair have equal and opposite spin and momentum. On applying a potential a Cooper pair can not interact with the lattice and change momentum since it would occupy a forbidden quantum state. A Cooper pair can therefore pass through a lattice without interaction with the lattice and hence exhibits zero resistance. The energy required to break the pair is the binding energy. BCS theory makes several important predictions including the temperature dependence of both the thermodynamic critical field and specific heat.

2.8 London Equations

Soon after the discovery of the Meissner effect [8], Fritz and Heinz London proposed a qualitative description of the screening currents around the edge of the superconductor and the distribution of magnetic field inside this layer [15]. The first London equation describes the zero resistance state of a superconductor

$$\boldsymbol{E} = \mu_0 \lambda_L \frac{\partial \boldsymbol{J}_s}{\partial t} \tag{2.2}$$

where

$$\lambda_L{}^2 = \frac{\mathrm{m_s}}{\mu_0 n_s \mathrm{e_s}{}^2} \tag{2.3}$$

J_s, m_s, n_s and e_s are the current density, mass, number density and charge of the supercurrent respectively. The parameter λ_L is the London penetration depth.

The second London equation describes the penetration of a magnetic field into a superconductor

$$\boldsymbol{B} = -\mu_0 \lambda_L^2 \nabla \times \boldsymbol{J} \qquad \textbf{(2.4)}$$

which when combined with the Maxwell equation $\nabla \times \boldsymbol{B} = \mu_0 \boldsymbol{J}$ gives

$$\nabla^2 \boldsymbol{B} = \frac{1}{\lambda_L^2} \boldsymbol{B} \qquad \textbf{(2.5)}$$

Thus the magnetic field decays exponentially upon penetrating a superconducting sample. The London equations predict that the magnetic field penetrates to a depth λ_L inside a superconducting sample.

2.9 Ginzburg-Landau Theory

Ginzburg-Landau theory [16] is a generalisation of the London theory. It is based on Landau's theory of second order phase transitions [17] and uses quantum mechanics to predict the effect of magnetic field on superconducting materials. The main extension over the London theory is that whereas London assumed a constant density of superelectrons, n_s, Ginzburg and Landau allow the density to vary spatially.

Ginzburg and Landau introduced an order parameter $\psi(\mathrm{r})$ with values between 0 and 1, defined as 0 in a normal conducting region and increasing to 1 in a fully superconducting region at 0 K. $\psi(r)$ is related to the density of superconducting charges, n_s, by

$$n_S(r) = |\psi(r)|^2 \qquad \textbf{(2.6)}$$

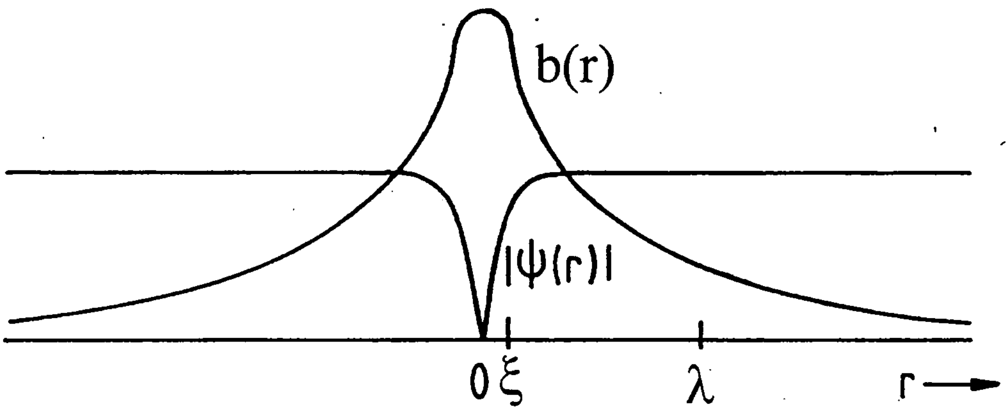

Figure 2.2 Magnetic field (b) and order parameter (ψ) as a function of distance from an isolated flux line of radius ξ, as predicted by Ginzburg-Landau theory [18].

Assuming the transition is second order, the free energy density of the superconducting state can be written as a power series in $|\psi(r)|^2$

$$f_s = f_n + \alpha|\psi(r)|^2 + \frac{\beta}{2}|\psi(r)|^4 + \frac{1}{2m_e}|(-i\hbar\nabla - 2eA)\psi|^2 + \frac{1}{2\mu_0}|\boldsymbol{B}_e - \boldsymbol{B}_i|^2 \quad (2.7)$$

where f_n represents the free energy density in the normal state, α and β are constants, m_e is the mass of an electron, A is the vector potential of the magnetic field and $\boldsymbol{B}_e$ and $\boldsymbol{B}_i$ are the external and internal fields respectively. In Equation (2.7), the penultimate term is the energy density associated with any local variation in B_i and $\psi(r)$ and the final term represents the energy density required to exclude the flux from the bulk of the superconductor.

The Ginzburg-Landau equations are obtained by integrating Equation (2.7) over the volume of the sample and minimising the resulting function with respect to ψ and A

$$\alpha\psi + \beta|\psi|^2 + \frac{1}{2m_e}(i\hbar\nabla - 2eA)^2\psi = 0 \qquad \textbf{(2.8)}$$

$$J_s = -\frac{ie\hbar}{m_e}\left(\psi^* \nabla\psi - \psi\nabla\psi^*\right) - \frac{4e^2}{m_e}|\psi|^2 A \qquad \textbf{(2.9)}$$

The coherence length (ξ_{GL}) is obtained by solving these equations. The coherence length is the distance over which the order parameter changes from 0 to 1 at a normal-superconducting interface. The decisive parameter in Ginzburg-Landau theory is the ratio of penetration depth to coherence length and is known as the Ginzburg-Landau parameter, κ.

$$\kappa = \frac{\lambda}{\xi_{GL}} \qquad \textbf{(2.10)}$$

Type I and Type II superconductors are distinguished by the magnitude of κ. For Type I superconductors $\kappa < 1/\sqrt{2}$ and for Type II superconductors $\kappa > 1/\sqrt{2}$.

2.10 Temperature dependence of B_{c2}

The temperature dependence of B_c is predicted by BCS theory to be

$$B_c(t) = B_c(0)\left(1-t^2\right) \qquad \textbf{(2.11)}$$

however for $T \approx T_c$ a better fit to the data can be given by

$$B_c(t) = 1.73 B_c(0)(1-t) \qquad \textbf{(2.12)}$$

where $t = T / T_c$[18]. Using $B_{c2} = \sqrt{2}\kappa B_c$ and a constant value of $\kappa(T)$ the temperature dependence of B_{c2} is given by

$$B_{c2}(t) = B_{c2}(0)\left(1-t^2\right). \qquad \textbf{(2.13)}$$

References for Chapter 2

[1] Onnes H 1908 *Comm. Leiden NR* **11** 168

[2] Onnes H 1911 *Comm. Leiden* **120b**

[3] Bednorz J and Muller K 1986 *Z. Phys. B - Condensed Matter* **64** 189-193

[4] Wu M, Ashburn J, Torng C, Hor P, Meng R, Gao L, Huang Z, Wang Y, and Chu C 1987 *Phys. Rev. Lett.* **58** 908-910

[5] Quinn D and Ittner W 1962 *Journal of Applied Physics* **33** 748-749

[6] Kedves F, Meszaros S, Vad K, Halasz G, Keszei B, and Mihaly L 1987 *Solid State Communications* **63** 991-992

[7] Yeh W-J, Chen L, Xu F, Bi B, and Yang P 1987 *Physical Review B* **46** 2414-2416

[8] Meissner W and Ochsenfeld R 1933 *Naturwissenschaften* **21** 787-788

[9] Grigorieva I 1994 *Superconductor Science and Technology* **7** 161-176

[10] Abrikosov A 1957 *Soviet Physics JETP* **5** 1174-1182

[11] Bardeen J, Cooper L, and Schrieffer J 1957 *Physical Review* **108** 1175-1204

[12] Frohlich H 1950 *Physical Review* **79** 845-856

[13] Bardeen J 1950 *Physical Review* **80** 567-574

[14] Cooper L 1956 *Physical Review* **104** 1189-1190

[15] London F and London H 1934 *Proc Roy Soc* **A149** 71-88

[16] Ginzburg V and Landau L 1950 *Zh. Eksp. Teor. Fiz* **20** 1064

[17] Landau V 1937 *Sow. Phys.* **11** 545-555

[18] Tinkham M, *Introduction to superconductivity* (McGraw-Hill, Inc., 1996).

Chapter 3

High Temperature Superconductivity

3.1 Introduction

This chapter focuses on the high temperature superconductors (HTS). Firstly the crystal structure and anisotropy of the materials is presented as widely discussed in the literature. Due to the high degree of anisotropy in the HTS systems, the isotropic Ginzburg-Landau (GL) model of superconductivity does not adequately describe the materials. The anisotropic G-L and Lawrence-Doniach theories, the dimensional crossover and their implications on the angular dependence of B_{c2} are presented in Section 3.3. In the following section the flux line lattice is introduced and flux pinning is discussed. Some LTS flux pinning theories are described before some of the current transfer models more recently published to describe the HTS materials. The effects of thermal activation of flux lines are presented in Section 3.5 through the flux creep and vortex glass models. Finally the mean-field magnetic phase diagram is presented before the more complicated version describing HTS materials explained in terms of the vortex-glass model.

3.2 Discovery, structure and anisotropy of fundamental parameters

Before 1986 superconductivity was thought to be a low temperature phenomenon with a highest observed critical temperature of 23 K[1]. Theoretical calculations only predicted superconductivity below 30 K using a Debye temperature of 100 – 500 K in the BCS equation for T_c[2]. In 1986 Bednorz and Muller[3] discovered superconductivity in the La-Ba-Cu-O system at 35 K. This discovery triggered an explosion of interest in copper oxide materials. In 1987 superconductivity was observed in the Y-Ba-Cu-O system up to 92 K[4]. Higher critical temperatures have since been observed in the Bi-Sr-Ca-Cu-O [5], Tl-Ba-Ca-Cu-O [6] and Hg-Ba-Ca-Cu-O[7] systems. Further work established three distinct superconducting phases of the Bi-Sr-Ca-Cu-O series[8-10].

Phase	T_c
$Y_1Ba_2Cu_3O_7$	92 K
$Bi_2Sr_2Ca_2Cu_3O_{10}$	110 K
$Tl_2Ba_2Ca_2Cu_3O_{10}$	115 K
$HgBa_2Ca_2Cu_3O_8$	133 K

Table 3.1. Critical temperatures of a selection of HTS materials. More comprehensive lists have been published[11,12].

All high temperature superconductors have a highly anisotropic structure, as shown in Figure 3.1. CuO_2 planes are a common feature occurring singly or in groups and are individually separated by metal oxide atoms. The groups of CuO_2 planes are intercalated by X-O layers, where X = La, Ba, Cu, Tl, Hg, Bi or Pb depending on the compound. It is currently believed that superconductivity predominantly occurs in the CuO_2 planes while the intercalating layers act as charge reservoirs[13]. The structural anisotropy is translated into anisotropy in most physical properties of the high temperature superconductors. An evaluation of anisotropy in the Y-Ba-Cu-O system has been made through studies of upper[14-23] [16,24-34] and lower[27,34-45] critical field, critical current density[46-54], resistivity[14,15,21-23,26,31,55-57], heat capacity[58-61] and penetration depth[40,42,62-65]. A greater degree of anisotropy has been observed in the Bi-Sr-Ca-Cu-O system through studies of upper [19,33,66-73] and lower[42,45,74-77] critical field, critical current density[78-86], resistivity[66,68,73,87-95], torque magnetometry[96] and penetration depth [42,97-102].

The greater level of anisotropy within the Bi-Sr-Ca-Cu-O system compared with Y-Ba-Cu-O has been clearly observed and is presented in Table 3.2. However conflicting experimental values of the superconducting parameters have been measured within each material series. Reasons for the discrepancy in these values may include a variation in sample quality. The exact sample stoichiometry is not always specified producing another reason for disagreement. In addition most groups have used the WHH theory[103] to extrapolate $B_{c2}(0)$. The success of the

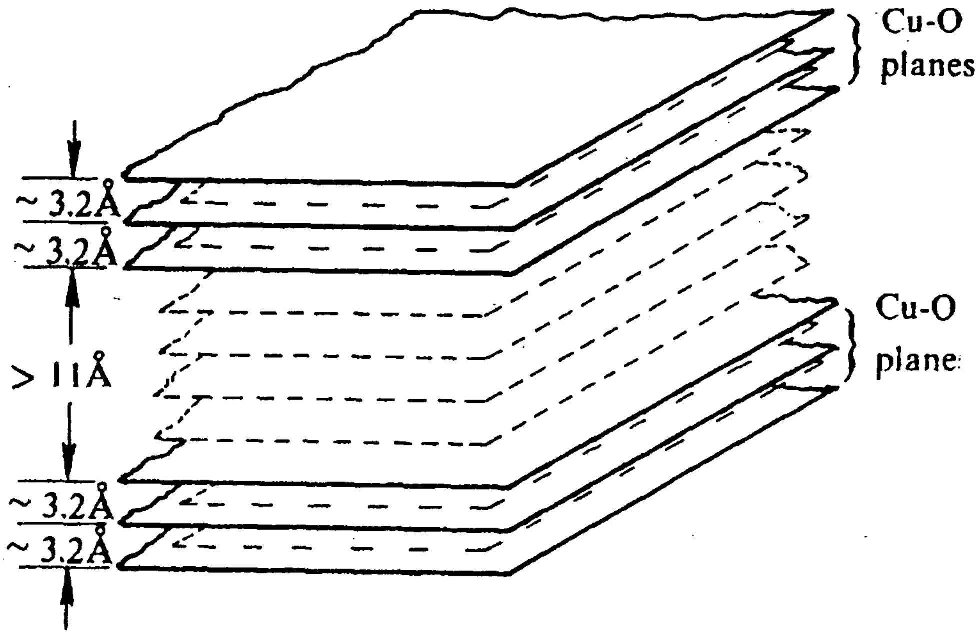

Figure 3.1. A schematic representation of the crystal structure of $Bi_2Sr_2Ca_2Cu_3O_x$ with groups of three CuO_2 planes[104]. The individual planes are separated by Ca layers and the groups of CuO_2 planes are separated by layers of BiO and SrO.

WHH predictions is strongly reliant on an accurately measured $-dB_{c2}/dT$ gradient close to T_c. Due to small distributions in T_c between the grains there is a changing gradient close to T_c which may affect the accuracy of the $B_{c2}(0)$ extrapolation. Conflicting values of the superconducting parameters may also be expected from different experimental techniques. Magnetisation data measures the response of the bulk of a sample while a resistivity trace relies upon a single percolation path through the sample. For these reasons, higher experimental values of B_{c2} may be expected from resistivity data. The thermal fluctuation effects close to T_c are responsible for the characteristic broad transitions seen in the resistivity data. Although most groups have defined T_c as the temperature at which $\rho = 0.5\ \rho_{normal}$, errors may be incurred in the analysis due to these broad transitions. For these reasons the magnetisation data may be most reliable. It is clear from the table that the level of anisotropy reported by magnetisation measurements is generally higher than by resistivity. In reviewing the literature the data believed to be most reliable has been presented in Table 3.3.

Material	**Sample**	**Measurement**	B_{c2} (*T*)		ξ(Å)		γ
			$B_{c2//c}$	$B_{c2//ab}$	ξ_c	ξ_{ab}	
$YBa_2Cu_3O_{7-\delta}$[28]	Film	R			25	8	3.1
$YBa_2Cu_3O_7$[17]	Film	Jc	73	237	21.2	6.5	3.3
$YBa_2Cu_3O_x$[24,31]	Crystal	R	56	190	24	7	3.4
$YBa_2Cu_3O_7$[105]	Crystal	R	61	222	23	< 6.3	3.6
$YBa_2Cu_3O_{7-\delta}Br_y$[14]	Crystal	R	78	313	21	5.1	4.1
$YBa_2Cu_3O_{7-\delta}$[27]	Crystal	M	87	380	20	4.5	4.4
$YBa_2Cu_3O_{7-x}$[15]	Crystal	R	118	510	17	3.9	4.4
$YBa_2Cu_3O_{7-x}$[25]	Crystal	M	29	140			4.8
$YBa_2Cu_3O_{7-\delta}$[18]	Crystal	M	122	674	16.4	3.0	5.5
$YBa_2Cu_3O_{7-y}$[21,22]	Crystal	R	35	160-210	31	5.1	6
$YBa_2Cu_3O_{7-x}$[16]	Crystal	M	64	400	22	3.6	6.1
$YBa_2Cu_3O_{7-\delta}$[36]	Crystal	M	35	230			6.6
$YBa_2Cu_3O_{7-x}$[20]	Crystal	M	34	240	31	4.3	7.2
$Bi_{2.2}Sr_2Ca_{0.8}Cu_2O_{8+\delta}$ [73]	Crystal	M / R	32	260			8.1
$Bi_2Sr_2CaCu_2O_y$[67]	Crystal	R	21	400			19.0
$Bi_{2.2}Sr_2Ca_{0.8}Cu_2O_{8+\delta}$ [66]	Crystal	R	22 (44)	533 (2640)			24.2
$Bi_2Sr_2Ca_2Cu_3O_x$[68]	Whisker	R	39	1210			31

Table 3.2. A review of B_{c2} and coherence lengths for the HTS from published work. R and M denote measurements taken by resistivity and magnetisation experiments respectively.

Parameters	**$YBa_2Cu_3O_7$ (s = 11.68 Å)[106]** //a-b plane	 //c-axis	**$Bi_2Sr_2Ca_2Cu_3O_{10}$ (s = 18 Å)[107]** //a-b plane	 //c-axis
T_c (K)	92		110	
$\xi(0)$ (Å)	16.4 [18]	3 [18]	29 [68]	0.93 [68]
$\lambda(0)$ (Å)	1415 [62]	7000 [62]	2000 [108]	10000 [108]
$B_{c1}(0)$ (mT)	18 [37]	53 [37]	11[a] [74]	33[a] [74]
$B_{c2}(0)$ (T)	674 [18]	122 [18]	1210 [68]	39 [68]
γ	3-6		3-31	

Table 3.3. Superconducting parameters for $YBa_2Cu_3O_7$ and $Bi_2Sr_2Ca_2Cu_3O_{10}$. s is the spacing between the groups of CuO_2 planes. [a] denotes data taken at 4.2 K.

3.3 Anisotropy and dimensionality

3.3.1 Ginzburg-Landau anisotropy

The anisotropic Ginzburg-Landau (G-L) theory[109] is a generalisation of the isotropic G-L model. The superconductor is treated as a continuum but with different properties along the principle axes. The Cooper pair mass is replaced by an effective mass tensor which has elements m_i, where i = 1, 2, 3 correspond to the a, b and c axes respectively. The elements are normalised such that $(m_a m_b m_c)^{1/3}=1$. The corresponding penetration depths and coherence lengths can be written as

$$\lambda_i = \lambda(m_i)^{1/2} \text{ where } \lambda = (\lambda_a \lambda_b \lambda_c)^{1/3} \tag{3.1}$$

and

$$\xi_i = \xi/(m_i)^{1/2} \text{ where } \xi = (\xi_a \xi_b \xi_c)^{1/3} \tag{3.2}$$

The anisotropic G-L theory can be used to describe an anisotropic superconductor within the 3-D limit as defined by $\xi_{i,j,k} > s$, where s is the distance between superconducting layers. The anisotropy of the critical fields can be expressed within the anisotropic approximation as $B_{c2}=\Phi_0/2\pi\xi_i\xi_j$, where the relevant values of $\xi_{i,j}$ are those for the two axes perpendicular to the field direction. Therefore the expressions for the upper critical field with field applied parallel to the a, b and c axes are

$$B_{c2//a} = \frac{\phi_0}{2\pi\xi_\beta\xi_\chi};\ B_{c2//b} = \frac{\phi_0}{2\pi\xi_\alpha\xi_\chi};B_{c2//c} = \frac{\phi_0}{2\pi\xi_\beta\xi_\chi} \qquad \textbf{(3.3)}$$

respectively. In high temperature superconductors, $m_c >> m_a \approx m_b$ and therefore anisotropy in the a-b plane is generally neglected. The expressions for upper critical field become $B_{c2//ab} = \frac{\phi_0}{2\pi\xi_{\alpha\beta}\xi_\chi}$ and $B_{c2//c} = \frac{\phi_0}{2\pi\xi_{\alpha\beta}^{\ 2}}$ for field applied parallel to the a-b planes and c-axis respectively.

The dimensionless anisotropy parameter, γ, is used to express the degree of anisotropy in a material where

$$\gamma = \left(\frac{m_c}{m_{ab}}\right)^{1/2} = \frac{\lambda_c}{\lambda_{ab}} = \frac{\xi_{ab}}{\xi_c} = \frac{B_{c2//ab}}{B_{c2//c}} = \frac{B_{c1//c}}{B_{c1//ab}} \qquad \textbf{(3.4)}$$

The angular dependence of B_{c2} within the 3-D limit can be described by

$$\left(\frac{B_{c2}(\theta)\sin\theta}{B_{c2//c}}\right)^2 + \left(\frac{B_{c2}(\theta)\cos\theta}{B_{c2//ab}}\right)^2 = 1 \qquad \textbf{(3.5)}$$

where θ is the angle between the magnetic field and the a-b plane.

3.3.2 Crossover to two dimensional behaviour

An implicit assumption of the Ginzburg Landau theory is that all characteristic lengths of superconductivity are larger than the spacing between the superconducting layers. The smallest length in the anisotropic G-L theory is $\xi_c(T)$ and this length can be compared with the distance between the superconducting layers, s. At temperatures sufficiently close to T_c, $\xi_c >> s$ and therefore use of the anisotropic G-L theory is justified. As the temperature is reduced the length of ξ_c is reduced to a limiting value. If that limit is less than s at a specific temperature the 3-D continuum approximation is replaced by 2-D behaviour of individual layers. The anisotropic G-L theory does not incorporate this crossover from 3-D to 2-D behaviour.

3.3.3 Lawrence-Doniach Theory

Lawrence and Doniach (L-D) proposed a successful theory to treat the crossover between 2-D and 3-D behaviour in layered superconducting materials[110]. This theory has since been extended[111-114] and considered for high temperature superconductors[115,116]. L-D approximate the layered superconductor as an array of weakly coupled 2-D superconducting layers. The model assumes the G-L equations apply within the layers while the layers are coupled along the c-axis via Josephson tunnelling. When $\xi_c < s$ Josephson coupling is weak and the material exhibits 2-D layered behaviour. In the strong inter layer coupling case and as T approaches T_c, where ξ_c becomes large compared with the interlayer spacing, the theory reduces to the anisotropic G –L theory.

L-D showed the temperature of the transition from a two-dimensional to a three-dimensional lattice is

$$T_{2D-3D} = T_c\left[1-\frac{1}{\gamma^2}\left(\frac{2\xi_{ab}(0)}{s}\right)^2\right] \qquad \textbf{(3.6)}$$

The angular dependence of B_{c2} in the 2-D limit is predicted by Tinkham[117]

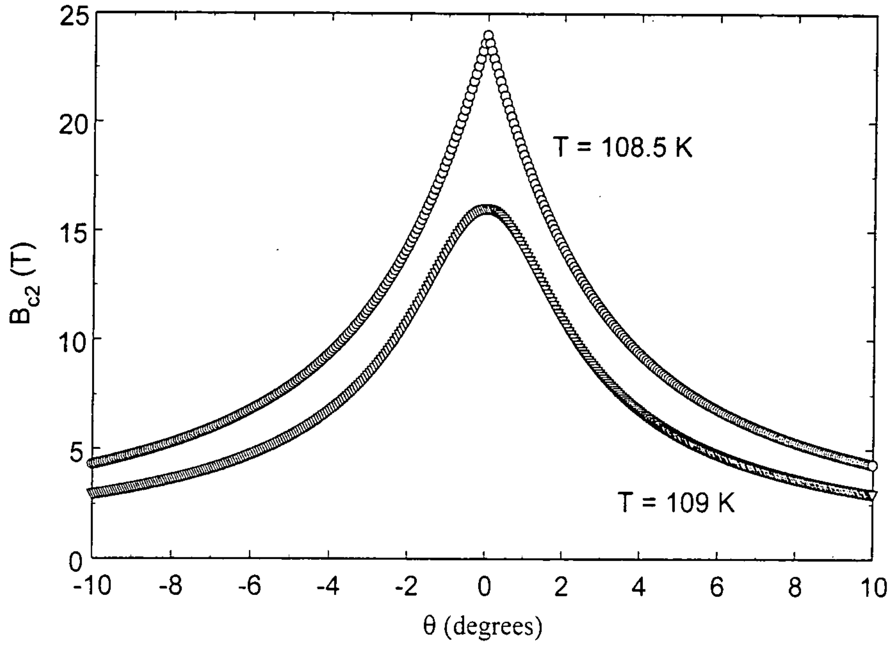

Figure 3.2. Angular dependence of B_{c2} for Bi-2223 above and below crossover temperature. The angular dependence is calculated using equations 3.5 and 3.7 for the 3-D and 2-D cases respectively. The anisotropy parameters are taken from Table 3.3.

$$\left|\frac{B_{c2}(\theta)\sin\theta}{B_{c2//c}}\right| + \left(\frac{B_{c2}(\theta)\cos\theta}{B_{c2//ab}}\right)^2 = 1. \tag{3.7}$$

3.3.4 Observations and predictions of the dimensional crossover

The dimensional crossover was first studied in intercalated layered LTS systems[118-120] and artificially prepared systems[121-124] where layer thickness and separation can be controlled. The highly anisotropic nature of the superconducting cuprates has led to studies of the coupling in both the Y-Ba-Cu-O[101,125-129] and Bi-Sr-Ca-Cu-O[82,94,101,130-134] systems including investigations on HTS materials with artificially introduced insulating layers between superconducting planes[126-128] and systems modelling HTS materials[135]. Inserting the values for s and $\xi_z(0)$ from Table 3.3 into Equation 3.6, crossover behaviour is predicted at $0.99T_c$ (108.9 K) for $Bi_2Sr_2Ca_2Cu_3O_x$ and $0.78T_c$ (71.8 K) for $YBa_2Cu_3O_7$. B_{c2} at these temperatures has been predicted using Equation 2.13. In Figure 3.2 the predicted angular dependencies of B_{c2} from Equations 3.5 and 3.7 are presented just above and below the dimensional cross-over temperature of $Bi_2Sr_2Ca_2Cu_3O_x$ (108.9 K). The models are only distinguishable when the field is applied at angles close to a-b planes, the 2-D model predicts a cusp for θ close to zero and the 3-D model predicts a rounder peak.

3.4 Flux line lattice

3.4.1 Flux pinning centres

In a type II superconductor for fields between B_{c1} and B_{c2} flux lines penetrate the sample. The introduction of imperfections to a superconducting material, typically through defects or grain boundaries, produces preferentially favourable positions for the flux lines thus disrupting the order within the flux line lattice, these positions are known as pinning centres. Typical examples of pinning centres are magnetic interactions, due to the interaction of surfaces between a normal and superconducting material, and core interactions, superconducting pinning centres producing local variations in T_c or κ, δT_c, and $\delta\kappa$ interactions respectively. $\delta\kappa$ interactions are caused by variations in the electron mean free path resulting in a local variation in the Ginzburg-Landau parameter. Vortex motion depends on the strength, density and distribution of pinning centres, on the elastic or plastic response of the vortex lattice and the homogeneity of the superconducting material.

3.4.2 Critical current density

On application of a transport current, flux lines are subjected to a Lorentz force per unit volume, $\boldsymbol{J} \times \boldsymbol{B}$. This force density can be supported by the pinning centres up to a critical current density, $\boldsymbol{J_c}$, such that

$$\boldsymbol{F_p} = \boldsymbol{J_c} \times \boldsymbol{B} \tag{3.8}$$

where $\boldsymbol{F_p}$ is the pinning density of the material.

As the current density is increased above J_c the flux lines move through the material dissipating heat. Therefore, J_c defines the useful limit for superconducting applications. Theoretically, the maximum current density that can be carried by a superconductor is the depairing current density, J_d. At this depairing current density the kinetic energy of the electrons is equal to the energy gap and any subsequent increase in current will destroy the superelectrons, driving the superconductor normal.

3.4.3 Bean Model

The Bean model[136,137] is widely used to describe the field and current distribution within a randomly pinned superconductor. Bean assumes that any current flowing in the superconductor will flow at the critical current density, J_c, thus defining the critical state. J_c was originally assumed to be independent of magnetic field. The Bean profile within a superconductor is shown in Figure 3.3 for a sequence of applied fields.

When a field above B_{c1} is applied to the sample, flux penetrates the sample a distance d determined by the strength and number density of the pinning sites, where $d = B/\mu_0 J_c$. The current flows within this depth at J_c, represented by the gradient in the Bean profile. On increasing the field sufficiently, the magnetic flux completely penetrates the sample. On decreasing the field the reversal in applied field induces

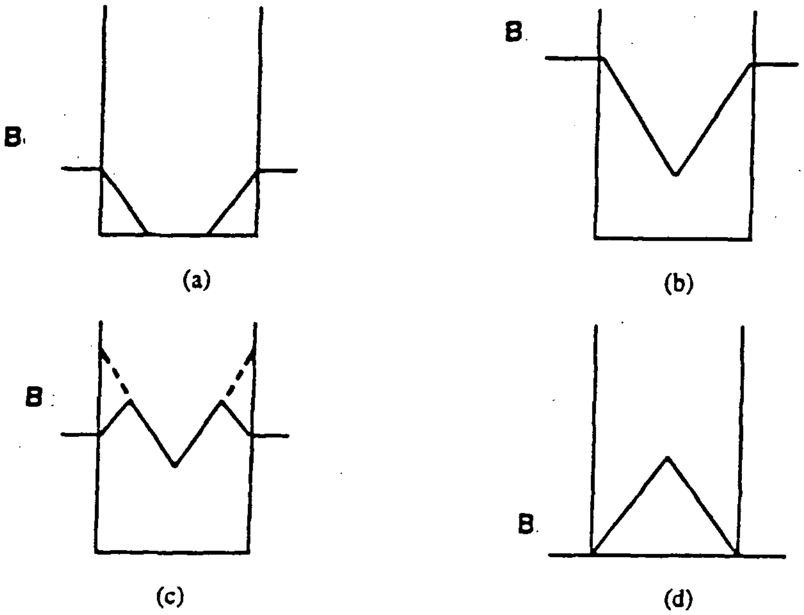

Figure 3.3. The field distribution within a superconductor for a series of applied fields[138].

screening currents that flow in the opposite direction but are still required to flow at J_c, this produces a change in sign of the gradient in the profile. On returning to zero applied field, flux remains trapped in the superconductor by the pinning sites.

3.4.4 Rigidity of the flux line lattice

Vortex-vortex interactions are responsible for the elastic rigidity of the flux line lattice. The elastic properties of the lattice can be described by the shear modulus, C_{66}, tilt modulus, C_{44}, and compression modulus C_{11}. For uniform distortions the elastic moduli of the triangular flux line lattice are given by Brandt[139]

$$C_{11} - C_{66} = B^2 \partial^2 F / \partial B^2 \qquad (3.9)$$

$$C_{44} = B \partial F / \partial B \qquad (3.10)$$

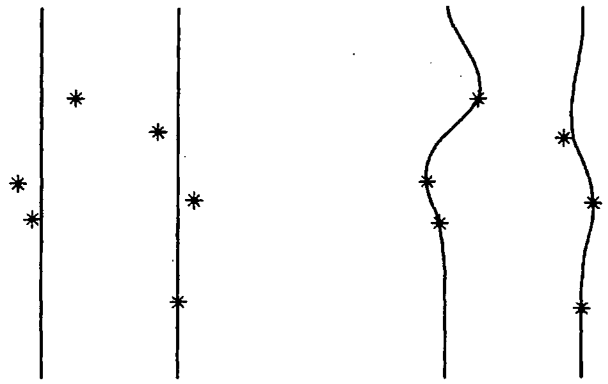

Stiff vortex lattice Soft vortex lattice

Figure 3.4. Comparison of vortex pinning in lattices of varying rigidity[140].

$$C_{66} \approx \left(B\phi_0 / 16\pi\lambda^2\mu_0\right)\left(1-\frac{1}{2\kappa^2}\right)(1-b)^2\left(1-0.58b+0.29b^2\right) \qquad \textbf{(3.11)}$$

where $b=B/B_{c2}$. Equation 3.9 is the modulus for isotropic compression and $\partial F/\partial B$ is the applied field which is in equilibrium with the flux line lattice at induction B. The effectiveness of pinning centres depends largely on the rigidity of the lattice. A stiff vortex lattice does not adjust to random pinning sites. However in a soft lattice, with weaker vortex-vortex interactions, the fluxons will adjust such that they sink deeply within the pinning potentials producing a stronger pinned system, as shown in Figure 3.4.

3.4.5 Scaling laws for J_c

3.4.5.1 Fietz-Webb scaling law

Fietz and Webb proposed the first scaling law for pinning in type II superconductors[141] after a series of measurements on niobium-titanium and niobium-tantalum alloys. By measuring experimental J_c and pinning force density values due to dislocation pinning over a wide range of temperatures and fields they found a scaling relation of the form

$$F_p(B,T) = \alpha_p(T)B_{c2}{}^n(T)b^p(1-b)^q \qquad \textbf{(3.12)}$$

where b is reduced field, B/B_{c2}. This work led to the observation that if the normalised pinning force density, F_p/F_{pmax}, is plotted as a function of reduced field, data at different temperatures sit on the same curve.

3.4.5.2 The Kramer model

Kramer developed a pinning theory based on several experimental observations[142]; i) a peak in $F_p(b)$ is a universal feature of all pinning force density curves; ii) for a given sample, a plot of normalised pinning force density as a function of reduced field produces a single curve at any temperature[141]; iii) metallurgical treatment effects the height and position of the peak in $F_p(b)$; iv) the functional form of $F_p(b)$ at high b is not affected by metallurgical treatment. Kramer considered the strength of pinning sites within a material with respect to the shear strength of the flux line lattice. At low field Kramer predicted that the movement of flux lines is due to the depinning of flux lines from the weak pinning sites, under the action of the Lorentz force. Strong pins are strong enough to compensate the Lorentz force at the highest fields, in this case the shear stresses around these pins due to the Lorentz forces and fluxon-fluxon interactions exceed the shear strength of the flux line lattice. Therefore at high fields fluxon motion is due to the shearing of the flux line lattice around the strong pins. An important implication from this work is that increasing the number density of defects will not increase J_c at high fields.

The Kramer model predicts the pinning force density as

$$\boldsymbol{F}_p = \boldsymbol{J}_c \times \boldsymbol{B} = \alpha b^{1/2}(1-b)^2 \qquad \textbf{(3.13)}$$

where $b=B/B_{c2}$ and α is a constant. B_{c2} is often predicted using the straight line Kramer extrapolation

$$J_c^{1/2}B^{1/4} = \alpha(1-b)\,. \tag{3.14}$$

3.4.6 The pinning force

3.4.6.1 Single mechanism pinning

The work of Dew-Hughes[143] predicts many functional forms of the pinning force density due to different mechanisms operating in materials. Both the Kramer[142] and Fietz-Webb[141] models are predicted by Dew-Hughes. The flux line lattice is assumed to be plastic, leading to the maximum possible pinning force. The pinning force per unit volume due to a single pinning interaction is given by

$$F_p = \eta L f_p \tag{3.15}$$

where f_p is the pinning force per unit length of pinned flux line, L is the length of flux line per unit length that is directly pinned and η is an efficiency factor determined by the extent to which its neighbours in the flux lattice allow a flux line to relax toward its position of maximum pinning.

Dew-Hughes modelled the functional form of the pinning force for superconducting and normal pins of point, surface and volume geometry due to magnetic and core interactions. Each pinning mechanism produces a different functional form of the pinning force. Comparison of experimental data with this work enables the dominating pinning mechanism within the sample to be determined.

3.4.6.2 Collective pinning

The presence of random pinning centres destroys the long-range order in the flux line lattice. In the simplest case each pinning centre would exert its maximum pinning force on the vortex lattice and hence the total pinning force in a given volume would simply be a summation of all pinning sites. However, this scenario is not usually observed in real systems in intermediate or high fields. This problem of the summation of elementary pinning forces was first solved by the theory of collective pinning[144].

Larkin and Ovchinnikov proposed that short range order remains within a certain volume V_c, containing randomly positioned pinning centres. On applying a current below J_c, the flux lines experience a Lorentz force against the pinning sites leading to a displacement of the volume V_c of a distance less than ξ. In magnetic fields where elastic deformations of the flux line lattice are important the volume V_c equals $R_c^2L_c$ where R_c and L_c are the transverse and longitudinal lengths of the region in which there is short range order. The lengths can be described by

$$R_c \propto \frac{C_{66}^{3/2}C_{44}^{1/2}a_0^2}{n_p f_p^2}\,;\, L_c \propto \frac{C_{66}C_{44}a_0^2}{n_p f_p^2} \tag{3.16}$$

where C_{66} and C_{44} are the elastic moduli of the flux line lattice, a_0 is the spacing of the flux line lattice, n_p is the density of pinning centres and f_p is the pinning force of an individual pinning centre. The critical current density in this regime is given as

$$J_c \propto \frac{n_p^2 f_p^4}{Ba_0^3 C_{44} C_{66}^2} \tag{3.17}$$

If the lengths R_c and L_c remain greater than the lattice spacing a_0 and the deformations remain elastic, collective pinning acts on the flux lines within the volume V_c. Once the deformations become plastic individual vortex-pin pinning dominates. The presence of collective pinning depends on the strength of pinning forces f_p and the number density of pinning sites n_p. Generally strong lattice deformation leads to individual vortex-pin interactions while short range order promotes collective pinning.

In a material containing pinning centres of average strength, direct summation of pinning sites is appropriate both at low fields, where the vortex-vortex interaction is negligible, and close to B_{c2}, where the vortex lattice is completely flexible. Collective pinning exists in intermediate fields. A large concentration of weak pinning sites leads to collective pinning at all fields. Large randomly orientated pinning centres producing large deformations of the vortex lattice cause individual vortex-pin interactions to dominate.

3.4.7 Current transfer models

3.4.7.1 Brick Wall model

The brick-wall model[145] describes the percolative path of the current through the microstructure of HTS materials. The model assumes a brick wall type configuration of highly anisotropic grains. The c-axis of all grains is normal to the tape surface while the a and b axes of the grains are randomly orientated within the plane of the tape. The thickness of the grains is assumed small compared with their length and width. Grain boundaries are assumed to act as weak links. The small cross-sectional area of the interface between grains in the a-b directions result in low current carrying capacity and are assumed to carry negligible current. However, the large cross-sectional area of the interfaces between grains in the c-axis enables higher currents to be supported. For this reason the current path between the grains is directed solely through the c-axis Josephson junctions while current flows in the a-b plane within the grains. The current density in the brick-wall model is therefore limited by the intergranular j_c in the c-direction. The model predicts an initial drop in J_c at low fields followed by plateau up to high field and indicates that decreasing the thickness of the grains increases the plateau value of J_c. A similar J_c dependence on field has been observed in HTS materials at low temperatures[146,147].

3.4.7.2 Railway Switch model

The railway switch model[80] directly correlates the critical current density with observed microstructural features within HTS. The c-axes of the grains are misaligned at small angles ($\theta < 15^0$) to the normal to the tape surface. The a-b planes of the grains are randomly orientated as in the brick-wall model. The fundamental elements of the model are frequent small-angle grain boundaries between the c-axes of the grains exhibiting a high degree of crystalline perfection[147]. The field dependence of the critical current through the grain boundaries is assumed similar to the dependence within the grains allowing the current to always pass along the a-b planes within the grains. The overall J_c of the tape is determined by the grain which experiences the largest field component in the c-direction. The strong connectivity between the grains and the low normal state grain boundary resistance are assumed responsible for the high J_c values of the HTS and low resistivity above T_c respectively.

3.4.7.3 Percolation model

The percolation model[148] proposes that current flows along percolative paths across small-angle grain boundaries in a similar way to the railway-switch model. The c-axes of the grains are orientated randomly with respect to the tape normal and there is no preferential alignment of a-b axes. The model assumes that small angle grain boundaries between 10 – 20° have j_c close to the intergranular value and assumes that $j_c = 0$ across grain boundaries for $\theta > 20^0$. The model predicts that large J_c values can be observed in materials with only a small fraction of grain boundaries at small angles by combining the best aspects of 2D and 3D current flow. The percolative model predicts tape I_c between 3-30 % of single crystal performance.

3.4.7.4 Weak-link diffraction model

The work by Hampshire[149] investigates why J_c in bulk polycrystalline superconductors is less than 1 % of the depairing current density J_d. Hampshire proposes that with strong intragranular pinning a barrier has been reached to further increases in J_c of order $\ln(\kappa)/2\kappa^2$ less than the depairing current, J_d. The model assumes that superconducting samples can be modelled by describing the grain boundaries as normal weak links acting as diffracting barriers and assumes no pinning operates on flux lines moving along grain boundaries. Diffraction effects are caused by wave-like properties of superconducting electrons and can be described by the geometry of a multiple junction squid. The functional form of J_c is given by

$$J_c(B,T) = \alpha(T)\left(1-\frac{B}{B_{c2}(T)}\right)\exp\left(-\frac{B}{\beta(T)}\right) \qquad \textbf{(3.18)}$$

where $\alpha(T)$ is essentially the depairing current density multiplied by a diffraction term and $\beta(T)$ characterises the suppression of the order parameter by the magnetic field at grain boundaries. The $(1-B/B_{c2}(T))$ term is due to the suppression of the order parameter inside the grains. Good agreement is found between the J_c values predicted by this weak link diffraction model and high field experimental data.

3.4.7.5 Summary of HTS pinning

Many other groups have determined functional forms of J_c or F_p to fit their data. Examples are a proposed a logarithmic function to model data between 20 – 77 K up to high fields [150] and a unified materials equation based on the Anderson-Kim model [151,152]. Determination of the pinning mechanism in HTS materials is a continued source of study, several workers have found evidence for pinning mechanisms in YBCO caused by fluctuations in the charge carrier mean free path (δl pinning) near a lattice defect [153,154] and the ideal pinning centre for HTS materials is suggested to be superconducting with different properties from the bulk [155].

3.5 Thermally activated flux line dynamics

3.5.1 Flux creep

The inclusion of thermal fluctuations in the phenomenology of type II superconductors affects the dynamical behaviour of the flux line lattice. Anderson and Kim predicted at finite temperatures flux lines or flux bundles would move under a flux gradient by thermally activated flux jumps between pinning sites [156,157]. This flux motion is found to reduce logarithmically with time. This phenomenon is known as flux creep. Therefore the flux creep model predicts for $J < J_c$ a finite resistivity exists for any temperature above absolute zero. For $J > J_c$ the sample enters the flux flow regime as depinning occurs. In HTS materials due to the short coherence length flux creep is observed at lower temperatures and currents. At higher temperatures the effect of thermal activation becomes more pronounced and deviations from the logarithmic decay predicted by Anderson-Kim have been observed [158-160]. These observations have been interpreted in terms of the flux-creep model and labelled 'giant flux creep'. Thermally activated phenomena are often referred to as thermally activated flux flow (TAFF).

For low temperature type II superconductors, the Anderson-Kim model predicts J_c as

$$J_c = J_c(0)\left[1 - \frac{\mathrm{k_B}T}{U_0}\ln\left(\frac{Bd\Omega}{E_c}\right)\right] \qquad \textbf{(3.19)}$$

where $J_c(0)$ is critical current density at 0 K, d is the hopping distance, Ω is the attempt frequency of a hopping event and E_c is the voltage criterion[138]. Therefore any field or temperature will produce a measurable voltage across the superconductor. Tinkham calculated that the giant flux creep model puts serious constraints on operation at high temperatures and fields. For example, the resistance could never be zero in a field of 30 T regardless of B_{c2} and T_c values and a material with a T_c of 400 K would only exhibit zero resistance at room temperature in fields below 10 T [161].

Collective pinning – flux creep theories[162-165] were proposed by incorporating the effects of thermal fluctuations into the collective pinning theory. They argue that thermal fluctuations of the flux lines, $\langle u^2 \rangle$, increases the effective range of the pinning force, resulting in a smoothed pinning potential. Activation energy was predicted of the form

$$U(J) = (U_0 / \mu)\left[(J_{c0} / J)^{\mu} - 1\right] \tag{3.20}$$

including the characteristic exponent μ in a similar way to the vortex glass model.

3.5.2 Vortex Glass model

The vortex-glass model includes disorder in the system and predicts a truly zero resistance superconducting state. The addition of random pinning sites disturbs the long-range order of the vortex lattice. A number of vortices are pinned at these sites while in a stiff lattice groups of vortices between pinning sites are held in place by vortex-vortex repulsion forces in local hexagonal arrangements. This describes the vortex glass phase [166,167] with the lattice exhibiting short range order. The pinning sites provide a barrier against vortex motion of strength $U_0(B,T)$ and are able to overcome the Lorentz force density on the fluxons $\boldsymbol{J}$ x $\boldsymbol{B}$, where $\boldsymbol{J}$ is the current density, up to the critical current density, J_c. For $J < J_c$ the flux lines are pinned and so the vortex glass phase exhibits zero resistance in this condition.

As the vortices gain thermal energy the elastic forces within the lattice result in displacement of the vortices a distance u from the ideal configuration reaching an average displacement $\langle u^2 \rangle \propto T$, the constant depending on the rigidity of the lattice, C_{66}. As defined by the Lindemann criterion[168], when the average displacement $\langle u^2 \rangle^{1/2} = c_L a_0$, where c_L is between 0.1 to 0.3 and a_0 is the average flux line separation, the flux line lattice melts [169-171] into the vortex liquid phase enabling the flux lines to move independently of one another. The melting line separates the vortex glass and the vortex liquid phases and along which the shear modulus is equal to zero. Within the melted phase, if the pinning barriers are greater than the thermal energy, $U > k_BT$, vortices remain pinned although the lattice is not rigid. This is the pinned vortex liquid phase and occurs immediately above the melting line in the H-T diagram. Close to B_{c2} the pinning barriers are small compared with the thermal energy of the vortices, $U << k_BT$, the vortices can thus move within the lattice unaffected by the pinning sites in this unpinned liquid phase.

The first experimental evidence for the existence of the VG phase was seen in YBCO epitaxial films[172] in the scaling of non-linear *E-J* curves around the vortex-glass transition temperature T_g. These data are presented in Figure 3.5. Isothermal E-J curves at different temperatures were found to collapse onto two master curves above and below T_g when plotted as $(E / J) / \left|T - T_g\right|^{\upsilon(z+2-D)}$ verses $J / \left|T - T_g\right|^{\upsilon(D-1)}$ where z and υ are the dynamic and static critical indices and D represents the dimension of the fluxons, in accordance with the VG model. Later work on YBCO [173-176] and Bi-2223 [177,178] has been analysed in a similar way and has further supported the VG model. It has been suggested that the data by Koch could also be described using the flux-creep model [179].

More recent work has investigated the statistical properties of volume pinning force densities, their thermodynamic properties and the phase transition properties in HTS [180-183]. This work has been compared with the vortex-glass model in which there is no distribution in pinning strength. The isothermal scaling of *E-J* characteristics has been related to the thermodynamic properties of the pinning force density and its statistical distribution. By scaling using the proposed theory excellent agreement has been found with experimental data from YBCO and TlSCCO(2223). It has been shown that the GL transition line is identical to the depinning line for the minimum value of the pinning strength and the scaling of the indices is strongly influenced by the pinning properties.

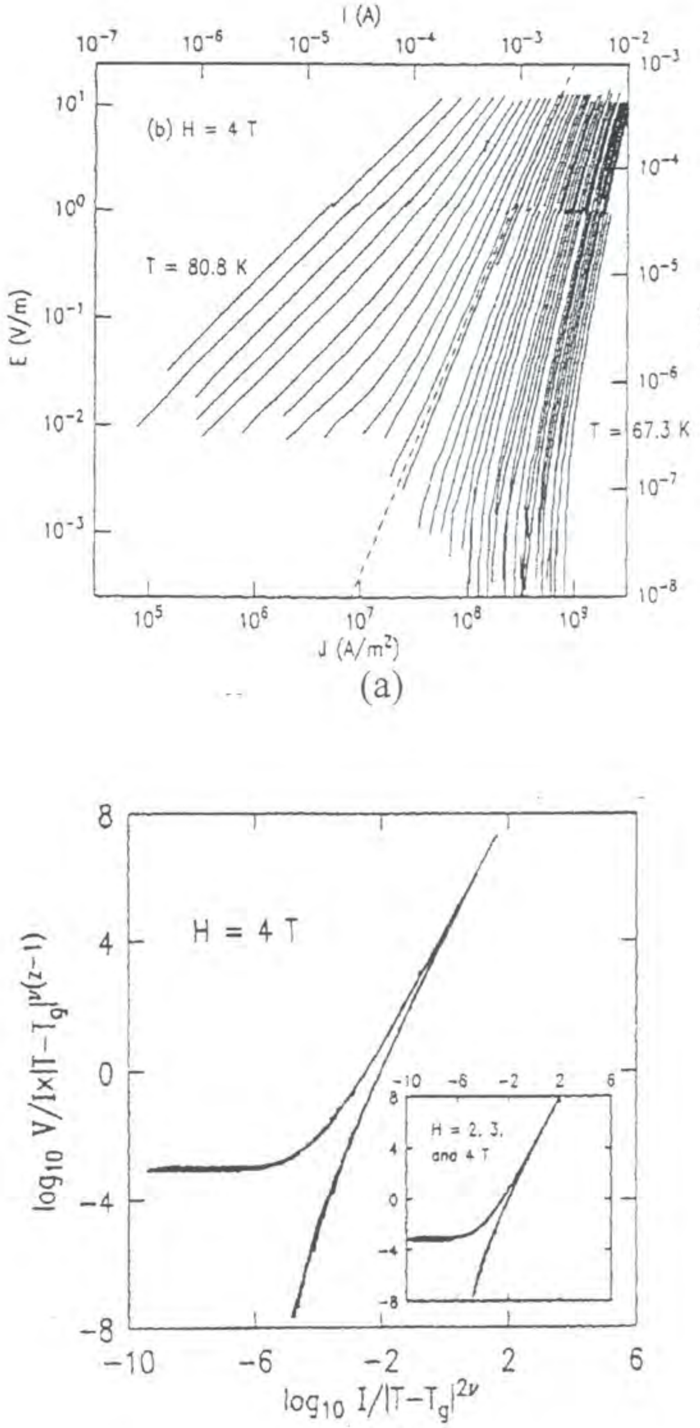

(a)

(b)

Figure 3.5. (a) Isothermal E-J curves taken at 4 T at temperatures intervals of 0.3 K between 67.3 – 80.8 K. The dashed line represents T_g at 77.4 K[172]; (b) Collapsed data curves from (a) lying on two master curves at 4 T[184].

3.5.3 Irreversibility Field

The irreversibility field (B_{irr}) is defined as the field at which J_c drops to zero. From a technological point of view B_{irr} provides the useful limit for the conductor and has been the subject of much theoretical and experimental research[139,140,185]. B_{irr} was first observed in HTS well below B_{c2}[4,158] and has since been observed in LTS closer to B_{c2}[186]. Behaviour of LTS[186] and HTS[187,188] materials have also been studied above B_{irr}. The connection between B_{irr} and the superconducting parameters is still not fully understood. Daniel et al have shown that in VSM measurements, J_c is measured to be zero when the effective ac field caused by the sample movement penetrates the entire sample and not, as is widely assumed, when the critical current becomes zero[189]. Therefore the apparent B_{irr} transition is solely an artefact of the field gradient of the system and cannot correctly be compared to theoretical calculations of the irreversibility field.

3.6 Magnetic phase diagrams

3.6.1 Mean field phase diagram

The mean field phase diagram proposed by Abrisokov[190] is shown in Figure 3.6 and contains three regions; i) the Meissner phase for $B < B_{c1}$ in which flux is completely excluded from the bulk of the superconductor; ii) a mixed phase for $B_{c1} < B < B_{c2}$ in which magnetic field penetrates the sample in the form of quantised vortices; iii) the normal conducting state for $B > B_{c2}$ where the magnetic field completely penetrates the material.

3.6.2 HTS phase diagram

The disorder and varying rigidity of the flux line lattice in HTS materials lead to a revised H-T diagram, explained in terms of the vortex-glass model. The

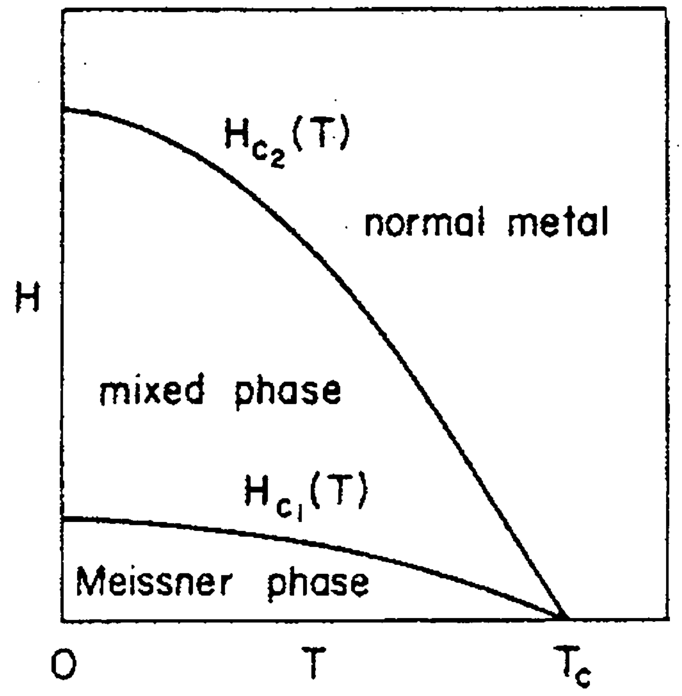

Figure 3.6. Mean-field phase diagram[185].

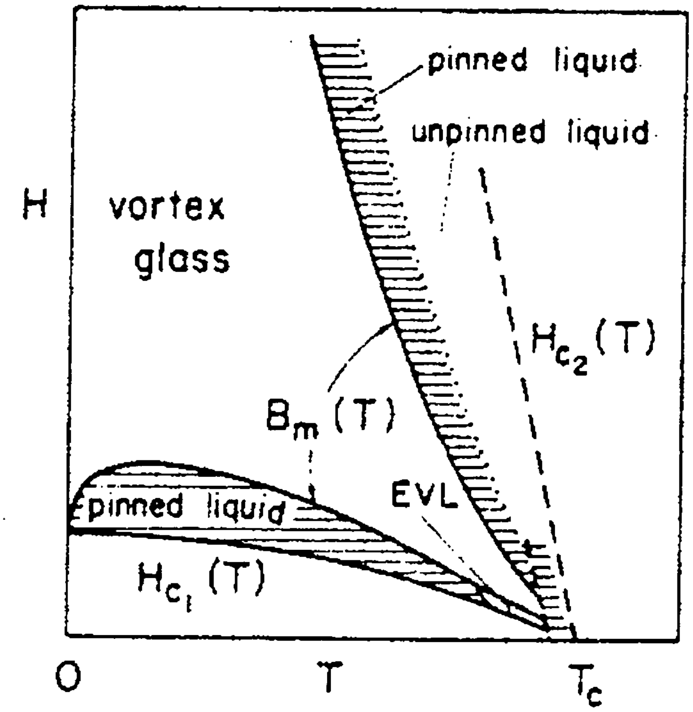

Figure 3.7. Phenomenological phase diagram for HTS[185]. The EVL region is the entangled vortex liquid. The vortex liquid-glass transition line is given by $B_m(T)$.

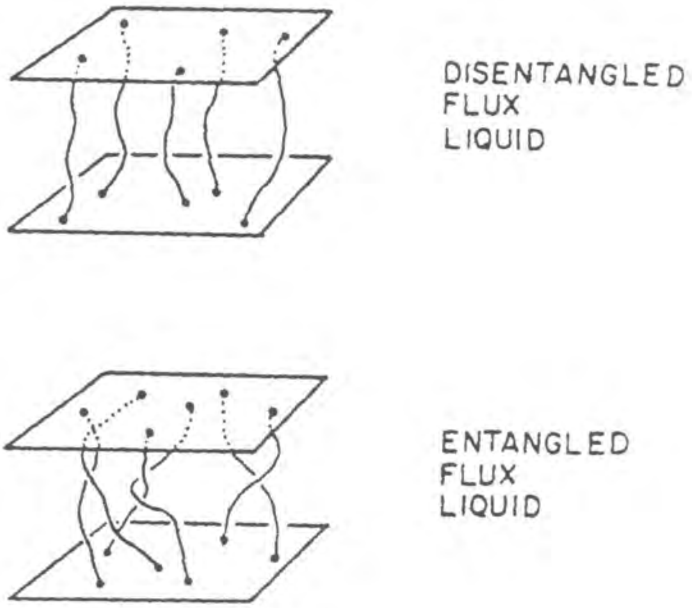

Figure 3.8. A schematic representation of the disentangled and entangled flux liquid phases[169].

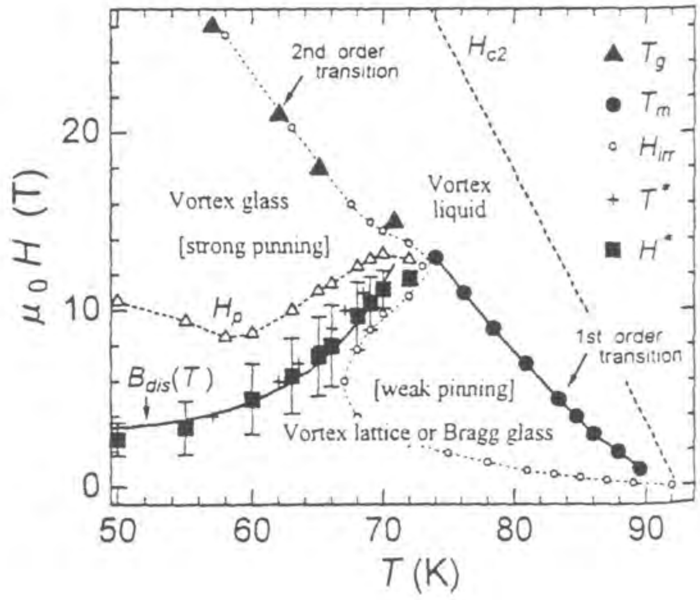

Figure 3.9. Magnetic field verses temperature phase diagram[191]. The vortex liquid, the vortex glass and the Bragg glass terminate at the multicritical point. The disordering transition line is given by $B_{dis}(T)$.

phenomenological phase diagram for an anisotropic layered HTS is given in Figure 3.7.

Below B_{c1} the superconductor exists in the Meissner state. On increasing B slightly above B_{c1} only a small number of vortices penetrate the superconductor, the distance between these few vortices is greater than the penetration depth λ resulting in very weak vortex-vortex interactions. The lattice is very soft in this region and since the energy of the pinning force > k_BT the flux line lattice is a pinned liquid. This re-entrant behaviour has been observed in LTS[192], the region being extremely narrow of width around 1 G. On increasing the field the shear modulus increases as the vortex fields overlap and the rigid lattice enters the vortex glass phase with the vortices pinned by pinning centres. At the melting line the lattice enters the liquid phase as the thermal energy of the fluxons increases. The sample first enters the pinned liquid phase but on approaching B_{c2} the pinning becomes weak compared with the thermal energy of the vortices and the unpinned liquid state is entered. Close to B_{c2} the vortices are strongly overlapping and above B_{c2} the sample exists in the normal state. In addition, at temperatures close to T_c, an elastic fluxon pinned at several points along its length will undergo transverse motion between pinning sites. The vortices repeatedly exchange places as they 'wander' around the lattice leading to an entangled flux lattice[169] close to T_c, represented in Figure 3.8. In summary, for $E_{vp} > E_{vv} > E_{th}$ the pinned vortex glass phase exists, $E_{vp} > E_{th} > E_{vv}$ the pinned liquid phase exists and for $E_{th} > E_{vp} > E_{vv}$ the unpinned liquid phase exists, where E_{vp} is the energy due to the votex-pin interaction, E_{vv} is the energy due to the vortex-vortex interaction and E_{th} is the thermal energy of a fluxon.

More recent experimental studies have identified the existence of at least three vortex phases[191,193,194]. Two vortex-solid phases have been identified, a weakly pinned well ordered Bragg glass phase and a strongly pinned vortex glass phase. The weakly pinned Bragg glass exists in the high temperature, low field region of the phase diagram undergoing a first-order phase transition into the vortex liquid phase when the temperature is increased. On increasing the field and reducing the temperature, the Bragg glass phase undergoes a second-order phase transition into a highly disordered, strongly pinned vortex glass. The three vortex phases meet on the phase diagram at a multicritical point as described by Nishizaki et al[191] and shown in Figure 3.9. Evidence for a two stage melting transition of vortex matter as a function of temperature has also been reported identifying melting and then decoupling of the vortex solid[195].

The phase diagram of the HTS materials continues to be the subject of extensive research. More comprehensive reviews of the H-T phase diagram are presented by Blatter[185], Cohen[140] and Brandt[139].

References for Chapter 3

[1] Gavaler J 1973 *Applied Physics Letters* **23** 480-482

[2] Bardeen J, Cooper L, and Schrieffer J 1957 *Physical Review* **108** 1175-1204

[3] Bednorz J and Muller K 1986 *Z. Phys. B - Condensed Matter* **64** 189-193

[4] Wu M, Ashburn J, Torng C, Hor P, Meng R, Gao L, Huang Z, Wang Y, and Chu C 1987 *Phys. Rev. Lett.* **58** 908-910

[5] Maeda H, Tanaka Y, Fukutomi M, and Asano T 1988 *Japanese Journal of Applied Superconductivity* **27** L209-L210

[6] Sheng Z and Hermann A 1988 *Nature* **332** 55-58

[7] Schilling A, Cantoni M, Guo J, and Ott H 1993 *Nature* **363** 56-58

[8] Hazen R, Prewitt C, Angel R, Ross N, Finger L, Hadidiacos C, Veblen D, Heaney P, Hor P, Meng R, Sun Y, Wang Y, Xue Y, Huang Z, Gao L, Bechtold J, and Chu C 1988 *Phys. Rev. Lett.* **60** 1174-1177

[9] Taracoscon J, McKinnon W, Barboux P, Hwang D, Bagley B, Greene L, Hull G, LePage Y, Stoffel N, and Giroud M 1988 *Physical Review B* **38** 8885-8892

[10] Tallon J, Buckley R, Gilberd P, Presland M, Brown I, Bowden M, Christian L, and Goguel R 1988 *Nature* **333** 153-156

[11] Harshman D and Mills Jr A 1992 *Physical Review B* **45** 10684-10712

[12] Rao C, Nagarajan R, and Vijayaraghavan R 1993 *Superconductor Science and Technology* **6** 1-22

[13] Cava R, Hewat A, Hewat E, Batlogg B, Marezio M, Rabe K, Krajewski J, Peck W, and Rupp L 1990 *Physica C* **165** 419-433

[14] Nguyen P, Wang Z, Rao A, Dresselhaus M, Moodera J, Dresselhaus G, Radousky H, Glass R, and Liu J 1993 *Physical Review B* **48** 1148-1155

[15] Iye Y, Tamegai T, Sakakibara T, Goto T, Miura N, Takeya H, and Takei H 1988 *Physica C* **153-155** 26-31

[16] Worthington T, Gallagher W, Kaiser D, Holtzberg F, and Dinger T 1988 *Physica C* **153-155** 32-37

[17] Zhao B, Kuroumaru S, Horie Y, Yanada E, Aomine T, Qui X, Zhang Y, Zhao Y, Xu P, and Li L 1991 *Physica C* **176** 409-419

[18] Welp U, Kwok W, Crabtree G, Vandervoort K, and Lui J 1989 *Phys. Rev. Lett.* **62** 1908-1911

[19] Naughton M, Yu R, Davies P, Fischer J, Chamberlin R, Wang Z, Jing T, Ong N, and Chaikin P 1988 *Physical Review B* **38** 9280-9283

[20] Gallagher W, Worthington T, Dinger T, Holtzberg F, Kaiser D, and Sandstrom R 1987 *Physica B* **148** 228-232

[21] Hidaka Y, Oda M, Susuki M, Katsui A, Murakami T, Kobayashi N, and Muto Y 1987 *Physica B* **148** 329-331

[22] Oda M, Hidaka Y, Suzuki M, and Murakami T 1988 *Physical Review B* **38** 252-256

[23] Hidaka Y, Enomoto Y, Suzuki M, Oda M, and Murakami T 1987 *Japanese Journal of Applied Physics* **26** L337-L339

[24] Iye Y, Tamegai T, Takeya H, and Takei H 1987 *Physica B* **148** 224-227

[25] Worthington T, Gallagher W, and Dinger T 1987 *Phys. Rev. Lett.* **59** 1160-1163

[26] Oh B, Char K, Kent A, Naito M, Beasley M, Geballe T, Hammond R, Kapitulnik A, and Graybeal J 1988 *Physical Review B* **37** 7861-7864

[27] Vandervoot K, Welp U, Kessler J, Claus H, Crabtree G, Kwok W, Umezawa A, Veal B, Downey J, and Paulikas A 1991 *Physical Review B* **43** 13042-13048

[28] Chaudhari P, Collins R, Freitas P, Gambino R, Kirtley J, Koch R, Laibowitz R, LeGoues F, McGuire T, Penney T, Schlesinger Z, and Segmuller A 1987 *Physical Review B* **36** 8903-8906

[29] Wordenweber R, Abd-El-Hamed M, Schneider J, and Laborde O 1991 *Journal of Applied Physics* **70** 2230-2233

[30] Gallito A and Vigni M 1996 *Physica C* **259** 365-372

[31] Iye Y, Tamegai T, Takeya H, and Takei H 1987 *Japanese Journal of Applied Superconductivity* **26** L1057-L1059

[32] Ukrainczyk I and Dulcic A 1994 *Europhysics Letters* **28** 199-204

[33] Ando Y, Boebinger G, Passner A, Schneemeyer L, Kimura T, Okuya M, Watauchi S, Shimoyama J, Kishio K, Tamasaku K, Ichikawa N, and Uchida S 1999 *Physical Review B* **60** 12475-12479

[34] Zheng D, Campbell A, Johnson J, Cooper J, Blunt F, Porch A, and Freeman P 1994 *Physical Review B* **49** 1417-1426

[35] Dinger T, Worthington T, Gallagher W, and Sandstrom R 1987 *Phys. Rev. Lett.* **58** 2687-2690

[36] Umezawa A, Crabtree G, Lui J, Moran T, Malik S, Nunez L, Kwok W, and Sowers C 1988 *Physical Review B* **38** 2843-2846

[37] Krusin-Elbaum L, Malozemoff A, Yeshurun Y, Cronemeyer D, and Holtzberg F 1989 *Physical Review B* **39** 2936-2939

[38] Umezawa A, Crabtree G, Welp U, Kwok W, Vandervoort K, and Lui J 1990 *Physical Review B* **42** 8744-8747

[39] Wu D and Sridhar S 1990 *Phys. Rev. Lett.* **65** 2074-2077

[40] Sridhar S, Wu D, and Kennedy W 1989 *Phys. Rev. Lett.* **63** 1873-1876

[41] Gallagher W 1988 *Journal of Applied Physics* **63** 4216-4219

[42] Bohmer, Brandstatter G, and Weber H 1997 *Superconductor Science and Technology* **10** A1-A10

[43] Konczykowski M, Burlachkov L, Yeshurun Y, and Holtzberg F 1991 *Physical Review B* **43**

[44] Burlachkov L, Yeshurun Y, Konczykowski M, and Holtzberg F 1992 *Physical Review B* **45** 8193-8196

[45] Tochihara S, Yasuoka H, Mazaki H, Osada M, and Kakihana M 1999 *Journal of Applied Physics* **85** 8299-8306

[46] Chaudhari P, Koch R, Laibowitz R, McGuire T, and Gambino R 1987 *Phys. Rev. Lett.* **58** 2684-2686

[47] Roas B, Schultz L, and Saemann-Ischenko G 1990 *Phys. Rev. Lett.* **64** 479-482

[48] Tachiki M and Takahashi S 1989 *Solid State Communications* **72** 1083-1086

[49] Hampshire D and Chan S 1992 *Journal of Applied Physics* **72** 4220-4226

[50] Watanabe K, Awaji S, Kobayashi N, Yamane H, Hirai T, and Muto Y 1991 *Journal of Applied Physics* **69** 1543-1546

[51] Kuwasawa Y, Yamaguchi T, Toska T, Aoki S, and Nakano S 1990 *Physica C* **169** 39-42

[52] Hettinger J, Swanson A, Skocpol W, Brooks J, Graybeal J, Mankiewich P, Howard R, Straughn B, and Burkhardt E 1989 *Phys. Rev. Lett.* **62** 2044-2047

[53] Satchell J, Humphreys R, Chew N, Edwards J, and Kane M 1988 *Nature* **334** 331-333

[54] Nishizaki T, Aomine T, Fujii I, Yamamoto K, Yoshii S, Terashima T, and Bando Y 1991 *Physica C* **181** 223-232

[55] Tozer S, Kleinsasser A, Penney T, Kaiser D, and Holtzberg F 1987 *Phys. Rev. Lett.* **59** 1768-1771

[56] Semba K, Ishii T, and Matsuda A 1991 *Phys. Rev. Lett.* **67** 769-772

[57] Hidaka Y, Enomoto Y, Suzuki M, Oda M, Katsui A, and Murakami T 1987 *Japanese Journal of Applied Superconductivity* **26** L726-L728

[58] Inderhees S, Salamon M, Rice J, and Ginsberg D 1991 *Phys. Rev. Lett.* **66** 232-235

[59] Junod A, Bonjour E, Calemczuk R, Henry J, Muller J, Triscone G, and Vallier J 1993 *Physics* **211** 304-318

[60] Ota S, Sastry V, Gmelin E, Murugaraj P, and Maier J 1991 *Physical Review B* **43** 6147-6150

[61] Salamon M, Inderhees S, Rice J, Pazol B, Ginsberg D, and Goldenfeld N 1988 *Physical Review B* **38** 885-887

[62] Harshman D, Schneemeyer L, Waszczak J, Aeppli G, Cava R, Batlogg B, Rupp L, Ansaldo E, and Williams D 1989 *Physical Review B* **39** 851-853

[63] Panagopoulos C, Cooper J, Xiang T, Peacock G, Gameson I, Edwards P, Schmidbauer W, and Hodby J 1997 *Physica C* **282-287** 145-148

[64] Athanassopoulou N and Cooper J 1996 *Physica C* **259** 326-336

[65] Fuchs A, Prusseit W, Berberich P, and Kinder H 1996 *Physical Review B* **53** R14745-14748

[66] Palstra T, Batlogg B, Schneemeyer L, Dover R, and Waszczak J 1988 *Physical Review B* **38** 5102-5105

[67] Koike Y, Nakanomoyo T, and Fukase T 1988 *Japanese Journal of Applied Superconductivity* **27** L841-843

[68] Matsubara I, Tanigawa H, Ogura T, Yamishita H, Kinoshita M, and Kawai T 1992 *Physical Review B* **45** 7414-7417

[69] Han S, Hegedus Z, Andersson M, Nygren M, Rapp O, Yan Y, Chen Q, Wei Y, and He Y 1990 *Physica C* **169** 250-256

[70] Kang J, Kampwirth R, and Gray K 1988 *Applied Physics Letters* **52** 2080-2082

[71] Laborde O, Monceau P, Potel M, Gougeon P, Padiou J, Levet J, and Noel H 1988 *Solid State Communications* **67** 609-611

[72] Li J, Kadowaki K, Menken M, Huang Y, Bakker K, Menovsky A, and Franse J 1988 *Applied Physics A* **47** 209-211

[73] Batlogg B, Palstra T, Schneemeyer L, Dover R, and Cava R 1988 *Physica C* **153-155** 1062-1066

[74] Tagaya K, Senda K, Yosida T, Fukuoka N, and Sasakura H 1992 *Japanese Journal of Applied Superconductivity* **31** L1170-L1171

[75] Job R and Rosenberg M 1991 *Physica C* **172** 391-399

[76] Li Q, Suenaga M, Gohng J, Finnemore D, Hikata T, and Sato K 1992 *Physical Review B* **46** 3195-3198

[77] Niderost M, Frassanito R, Saalfrank M, Mota A, Blatter G, Zavaritsky V, Li T, and Kes P 1998 *Phys. Rev. Lett.* **81** 3231-3233

[78] Yamasaki H, Endo K, Kosaka S, Umeda M, Misawa S, Yoshida S, and Kajimura K 1993 *IEEE Transactions on Applied Superconductivity* **3** 1536-1539

[79] Yamasaki H, Endo K, Kosaka S, Umeda M, Yoshida S, and Kajimura K 1993 *Phys. Rev. Lett.* **70** 3331-3334

[80] Hensel B, Grivel J, Jeremie A, Lerin A, Pollini A, and Flukiger R 1993 *Physica C* **205** 329-337

[81] Schmitt P, Kummeth P, and Schultz S-I, G. 1991 *Phys. Rev. Lett.* **67** 267-270

[82] Fastampa R, Sarti S, Silva E, and Milani E 1994 *Physical review B* **49** 15959-15964

[83] Schmitt P, Schultz L, and Saemann-Ischenko G 1990 *Physica C* **168** 475-478

[84] Raffy H, Labdi S, Laborde O, and Monceau P 1991 *Superconductor Science and Technology* **4** S100-S102

[85] Yamasaki H, Endo K, Nakagawa Y, Umeda M, Kosaka S, Misawa S, Yoshida S, and Kajimura K 1992 *Journal of Applied Physics* **72** 2951-2957

[86] Labdi S, Raffy H, Laborde O, and Monceau P 1992 *Physica C* **197** 274-282

[87] Martin S, Fiory A, Flemming R, Schneemeyer L, and Waszczak J 1988 *Phys. Rev. Lett.* **60** 2194-2197

[88] Iye Y, Oguro I, Tamegai T, and Datars W 1992 *Physica C* **199** 154-160

[89] Takagi H, Eisaki H, Uchida S, Maeda A, Tajima S, Uchinokura K, and Tanaka S 1988 *Nature* **332** 236-238

[90] Raffy H, Labdi S, Laborde O, and Monceau P 1991 *Phys. Rev. Lett.* **66** 2515-2518

[91] Wagner P, Hillmer F, Frey U, and Adrian H 1994 *Physical Review B* **49** 13184-13192

[92] Han G, Ong C, Li C, and Xi Z 1998 *Applied Physics Letters* **72** 2751-2753

[93] Juang J, Cutro J, Rudman D, Dover R, Schneemeyer L, and Waszczak J 1988 *Physical Review B* **38** 7045-7048

[94] Marcon R, Fastampa R, Giura M, and Silva E 1991 *Europhysics Letters* **16** 757-762

[95] Wise P, Dawson A, Datars W, and Garrett J 1989 *Solid State Communications* **70** 341-345

[96] Farrell D, Bonham S, Foster J, Chang Y, Jiang P, Vandervoort K, Lam D, and Kogan V 1989 *Phys. Rev. Lett.* **63** 782-785

[97] Maeda A, Shibauchi T, Kondo N, Uchinokura K, and Kobayashi M 1992 *Physical Review B* **46** 14234-14237

[98] Harshman D, Kleiman R, Inui M, Espinosa G, Mitsi D, Kapitulnik A, Pfiz T, and Williams D 1991 *Phys. Rev. Lett.* **67** 3152-3155

[99] Mitra S, Cho J, Lee W, Johnston D, and Kogan V 1989 *Physical Review B* **40** 2674-2677

[100] Kritscha W, Sauerzopf F, Weber H, Crabtree G, Chang Y, and Jiang P 1991 *Physica C* **179** 59-68

[101] Aegerter C, Lee S, Keller H, Forgan E, and Lloyd S 1996 *Physical Review B* **54** R15661-R15663

[102] Jacobs T, Sridhar S, Li Q, Gu G, and Koshizuka N 1995 *Phys. Rev. Lett.* **75** 5416-4519

[103] Werthamer N, Helfand E, and Hohenberg P 1966 *Physical Review* **147** 295-302

[104] Burns G, *High temperature superconductivity* (Scientific Press, 1992).

[105] Moodera J, Meservey R, Tkaczyk J, Hao C, Gibson G, and Tedrow P 1988 *Physical Review B* **37** 619-622

[106] Poole C, Farach H, and Creswick R, *Superconductivity* (1995).

[107] Matsubara I, Funahashi R, Ueno K, Yamashita H, and Kawai T 1996 *Physica C* **256** 33-38

[108] Cyrot M and Pavuna D, *Introduction to superconductivity and high-Tc materials* (World Scientific, 1992).

[109] Tilley D 1965 *Proc. Phys. Soc.* **86** 289-295

[110] Lawrence W and Doniach S 1970 *Proceedings of the 12th International Conference on Low Temperature Physics, Kyoto, Japan* 361-362

[111] Klemm R, Luther A, and Beasley M 1975 *Physical Review B* **12** 877-891

[112] Bulaevskii L 1973 *Sov. Phys. JETP.* **37** 1133-1136

[113] Schneider T, Gedik Z, and Ciraci S 1991 *Z. Phys. B* **83** 313-321

[114] Schneider T and Schmidt A 1993 *Physical Review B* **47** 5915-5921

[115] Clem J 1991 *Physical Review B* **43** 7837-7846

[116] Bulaevskii L and Vagner I 1991 *Physical Review B* **43** 8694-8697

[117] Tinkham M 1963 *Physical Review* **129** 2413-2422

[118] Woollam J and Somoano R 1976 *Physical Review B* **13** 3843-3853

[119] Prober D, Schwall R, and Beasley M 1980 *Physical Review B* **21** 2717-2733

[120] Coleman R, Eiserman G, Hillenius S, Mitchell A, and Vicent J 1983 *Physical Review B* **27** 125-139

[121] Ruggiero S, Barbee T, and Beasley M 1980 *Phys. Rev. Lett.* **45** 1299-1302

[122] Ruggiero S, Barbee T, and Beasley M 1982 *Physical Review B* **26** 4894-4908

[123] Banerjee I, Yang Q, Falco C, and Schuller I 1983 *Physical Review B* **28** 5037-5040

[124] Kanoda K, Mazaki H, Yamada T, Hosoito N, and Shinjo T 1986 *Physical Review B* **33** 2052-2055

[125] Farrell D, Rice J, Ginsberg D, and Liu J 1990 *Phys. Rev. Lett.* **64** 1573-1576

[126] Li Q, Xi X, Wu X, Inam A, Vadlamannati S, McLean W, Venkatesan T, Ramesh R, Hwang D, Martinez J, and Nazar L 1990 *Phys. Rev. Lett.* **64** 3086-3089

[127] Triscone J, Fischer O, Brunner O, Antagnazza L, Kent A, and Karkut M 1990 *Phys. Rev. Lett.* **64** 804-807

[128] Lowndes D, Norton D, and Budai J 1990 *Phys. Rev. Lett.* **65** 1160-1163

[129] Deak J, Hou L, Metcalf P, and McElfresh M 1995 *Physical Review B* **51** 705-708

[130] Silva E, Marcon R, Fastampa R, Giura M, and Sarti S 1993 *Physica C* **214** 175-178

[131] Fastampa R, Giura M, Marcon R, and Silva E 1991 *Phys. Rev. Lett.* **67** 1795-1798

[132] Marcon R, Silva E, Fastampa R, and Giura M 1992 *Physical Review B* **46** 3612-3618

[133] Martinez J, Brongersma S, Koshelev A, Ivlev B, Kes P, Griessen R, Groot D, Tarnavski Z, and Menovsky A 1992 *Phys. Rev. Lett.* **69** 2276-2279

[134] Schilling A, Jin R, Guo J, and Ott H 1993 *Phys. Rev. Lett.* **71** 1899-1902

[135] White W, Kapitulnik A, and Beasley M 1991 *Phys. Rev. Lett.* **66** 2826-2829

[136] Bean C 1962 *Phys. Rev. Lett.* **8** 250-253

[137] Bean C 1964 *Reviews of Modern Physics* 31-39

[138] Campbell A and Evetts J 1972 *Advances in Physics* **21** 199-430

[139] Brandt E 1995 *Rep. Prog. Phys.* **58** 1465-1594

[140] Cohen L and Jenson H 1997 *Rep. Prog. Phys.* **60** 1581-1672

[141] Fietz W and Webb W 1969 *Physical Review* **178** 657-667

[142] Kramer E 1973 *Journal of Applied Physics* **44** 1360-1370

[143] Dew-Hughes D 1974 *Philosophical Magazine* **30** 293-305

[144] Larkin A and Ovchinnikov Y 1979 *Journal of Low Temperature Physics* **34** 409-428

[145] Bulaevskii L, Clem J, Glazman L, and Malozemoff A 1992 *Physical Review B* **45** 2545-2548

[146] Jin S, van Dover R, Tiefel T, Graebner J, and Spencer N 1991 *Applied Physics Letters* **58** 868-870

[147] Sato K, Hikata T, Mukai H, Ueyama M, Shibuta N, Kato T, Masuda T, Nagata M, Iwata K, and Mitsui T 1991 *IEEE Transactions on Magnetics* **27** 1231-1238

[148] Specht E, Goyal A, and Kroeger D 1996 *Physical Review B* **53** 3585-3589

[149] Hampshire D 1997 *Physica C* **296** 153-166

[150] Kobayashi S, Kaneko T, Kato T, Fujikami J, and Sato K 1996 *Physica C* **258** 336-340

[151] Yin D, Li C, and Bai W 1998 *Applied Superconductivity* **5** 147-150

[152] Bai W, Li G, Chen H, Yin D, Lu G, Chen K, and Li C 1999 *IEEE Transactions on Applied Superconductivity* **9** 2647-2650

[153] Griessen R, Hai-hu W, van Dalen A, Dam B, Rector J, Schnack H, Libbrecht S, Osquiguil E, and Bruynseraede Y 1994 *Phys. Rev. Lett.* **72** 1910-1913

[154] Giller D, Shaulov A, and Yeshurun Y 2000 *Physica B* **284-288** 687-688

[155] Koblischka M 1997 *Physica C* **282-287** 2193-2194

[156] Anderson P 1962 *Phys. Rev. Lett.* **9** 309-311

[157] Anderson P and Kim Y 1964 *Reviews of Modern Physics* **36** 39-43

[158] Yeshurun Y and Malozemoff A 1988 *Phys. Rev. Lett.* **60** 2202-2205

[159] Malozemoff A 1991 *Physica C* **185-189** 264-269

[160] Thompson J, Sun Y, and Holtzberg F 1991 *Physical Review B* **44** 458-461

[161] Tinkham M 1988 *Phys. Rev. Lett.* **61** 1658-1661

[162] Feigel'man M, Geshkenbein V, Larkin A, and Vinokur V 1989 *Phys. Rev. Lett.* **63** 2303-2306

[163] Feigel'man M and Vinokur V 1990 *Physical Review B* **41** 8986-8990

[164] Feigel'man M, Geshkenbein V, and Vinokur V 1991 *Physical Review B* **43** 6263-6265

[165] Thompson J and Sun Y 1993 *Phys. Rev. Lett.* **47** 14440-14447

[166] Fisher M 1989 *Phys. Rev. Lett.* **62** 1415-1418

[167] Fisher D, Fisher M, and Huse D 1991 *Physical Review B* **43** 130-159

[168] Lindemann F 1910 *Phys. Z.* **11** 609

[169] Nelson D and Seung H 1989 *Physical Review B* **39** 9153-9174

[170] Houghton A, Pelcovits R, and Sudbo A 1989 *Physical Review B* **40** 6763-6770

[171] Franz M and Teitel S 1995 *Physical Review B* **51** 6551-6574

[172] Koch R, Foglietti V, Gallagher W, Koren G, Gupta A, and Fisher M 1989 *Phys. Rev. Lett.* **63** 1511-1514

[173] Worthington T, Olsson E, Nichols C, Shaw T, and Clarke D 1991 *Physical Review B* **43** 10538-10543

[174] Gammel P, Schneemeyer L, and Bishop D 1991 *Phys. Rev. Lett.* **66** 953-956

[175] Dekker C, Woltgens P, Koch R, Hussey B, and Gupta A 1992 *Phys. Rev. Lett.* **69** 2717-2720

[176] Wang Z, Zhang H, and Cao X 2000 *Physica C* **337** 62-66

[177] Yamasaki H, Endo K, Kosaka S, Umeda M, Yoshida S, and Kajimura K 1994 *Physical Review B* **50** 12959-12965

[178] Yamasaki H, Endo K, Mawatari Y, Kosaka S, Umeda M, Yoshida S, and Kajimura K 1995 *IEEE Transactions on Applied Superconductivity* **5** 1888-1891

[179] Coppersmith S, Inui M, and Littlewood P 1990 *Phys. Rev. Lett.* **64** 2585

[180] Kiss T, Matsushita T, and Irie F 1999 *Superconductor Science and Technology* **12** 1079-1082

[181] Matsushita T and Kiss T 1999 *Physica C* **315** 12-22

[182] Yamafugi K and Kiss T 1996 *Physica C* **258** 197-212

[183] Yamafuji K and Kiss T 1997 *Physica C* **290** 9-22

[184] Koch R, Foglietti V, and Fisher M 1990 *Phys. Rev. Lett.* **64** 2586

[185] Blatter G, Feigel'man M, Geshkenbein V, Larkin A, and Vinokur V 1994 *Rev. Mod. Phys.* **66** 1125-1387

[186] Suenga M, Ghosh A, Xu Y, and Welch D 1991 *Phys. Rev. Lett.* **66** 1777-1780

[187] Genoud J, Triscone G, Junod A, Tsukamoto T, and Muller J 1995 *Physica C* **242** 143-154

[188] Zheng D, Campbell A, and Liu R 1993 *Physical Review B* **48** 6519-6524

[189] Daniel I and Hampshire D 2000 *Physical Review B* **61** 6982-6993

[190] Abrikosov A 1957 *Soviet Physics JETP* **5** 1174-1182

[191] Nishizaki T, Naito T, and Kobayashi N 1998 *Physical Review B* **58** 11169-11172

[192] Ravikumar G, Chandrasekhar Rao T, Mishra P, Sahni V, Saha S, Banerjee S, Patil N, Grover A, Ramakrishnan S, Bhattacharya S, Yamamoto E, Haga Y, Inada Y, and Onuki Y 1997 *Physica C* **276** 9-17

[193] Khaykovich B, Zeldov E, Majer D, Li T, Kes P, and Konczykowski M 1996 *Phys. Rev. Lett.* **76** 2555-2558

[194] Giller D, Shaulov A, Yeshurun Y, and Giapintzakis J 1999 *Physical Review B* **60** 106-109

[195] Blasius T, Niedermayer C, Tallon J, Pooke D, Golnik A, and Bernhard C 1999 *Phys. Rev. Lett.* **82** 4926-4929

Chapter 4

Critical Current Density of Bi-2223/Ag Multifilamentary Tapes from 4.2 K up to 90 K in Magnetic Fields up to 23 T

4.1 Introduction

The Bi-based high temperature superconductors are among the most promising materials for high current density (J_c), high field applications. The highly layered structure of Bi-2223 and strongly anisotropic superconducting and mechanical properties have made it difficult to find a clear explanation for the mechanisms that determine the critical current density in these materials. In recent years fabrication techniques have improved sufficiently that tapes are now produced in kilometre lengths creating the realistic possibility of large scale applications. Probably most promising for applications requiring long lengths of conductor is the powder-in-tube route. It has been found empirically that good grain alignment and clean grain boundaries are important to achieve high J_c values in these tapes. However a better understanding of the factors limiting J_c would doubtless lead to even further improvements. In this chapter a comprehensive J_c data for a Bi-2223/Ag multifilamentary powder-in-tube tape from 4.2 K up to 90 K in fields up to 23 T is presented. These data can be used to test the predictions of the many models in the literature that have been suggested to explain the high field J_c properties of these tapes [1-3]. The J_c dependence of short samples of the Bi-2223 tape as a function of field and temperature for 3 orientations of the tape with respect to the field are presented.

The following two sections outline the experimental details and results. The analysis of this work has been performed using the simple exponential form, $J_c = \alpha(T)\exp[-B/\beta(T)]$, such that these results can be compared with data in the literature. A more comprehensive analysis of these J_c data is presented in Chapter 6 with the inclusion of B_{c2} and quality of grain alignment to give a more complex functional form of J_c. A preliminary discussion of the data and theoretical models in the literature are then presented at the end of this chapter.

4.2 Experimental

The 37 filament Bi-2223/Ag tape used in the measurements was fabricated using the powder in tube method. The tapes have a cross-sectional area of 0.854 mm^2 and fill factor of 36.2%. The critical current density transport measurements at 4.2 K were made in fields up to 23 T at the Grenoble High Field Facility. Measurements made at temperatures above 4.2 K were made in fields up to 15 T in Durham. Short samples of length 20 mm were cut and mounted on tufnol. A standard dc four terminal measurement was used to determine the critical current density. The voltage taps were spaced 6 mm apart and connected to the tape using silver paint to avoid any mechanical damage. The current taps were soldered to the tape using lead-tin solder. For measurements at 4.2 K, the samples were directly immersed in liquid helium. Measurements at temperatures above 4.2 K were made using a $J(B,T)$ probe developed in Durham [4]. When operating this probe, the sample is held in a variable-temperature vacuum enclosure. The accuracy of the data quoted in this paper is expected to be equivalent to an uncertainty in temperature of ± 3 K. J_c was found to be very sensitive to the orientation of the tape with respect to the applied field. Hence the sample and the current leads attached to the sample were firmly held down to avoid any movement. Measurements were taken with the tape in three orientations with respect to field; 1) Field parallel to the a-b planes and perpendicular to current; 2) Field parallel to both a-b planes and current; 3) Field parallel to c-axis of the tape and perpendicular to current. J_c was determined for the superconductor alone from the E-J characteristics using a criterion of 1.5 $\mu V.cm^{-1}$. After obtaining the data for any orientation the sample was allowed to warm up to expel any trapped flux, and the critical current density was remeasured in zero field in liquid nitrogen. No change was found from the J_c values obtained before the measurement for any of the samples presented in this chapter. This demonstrates that no damage occurred during the experiments.

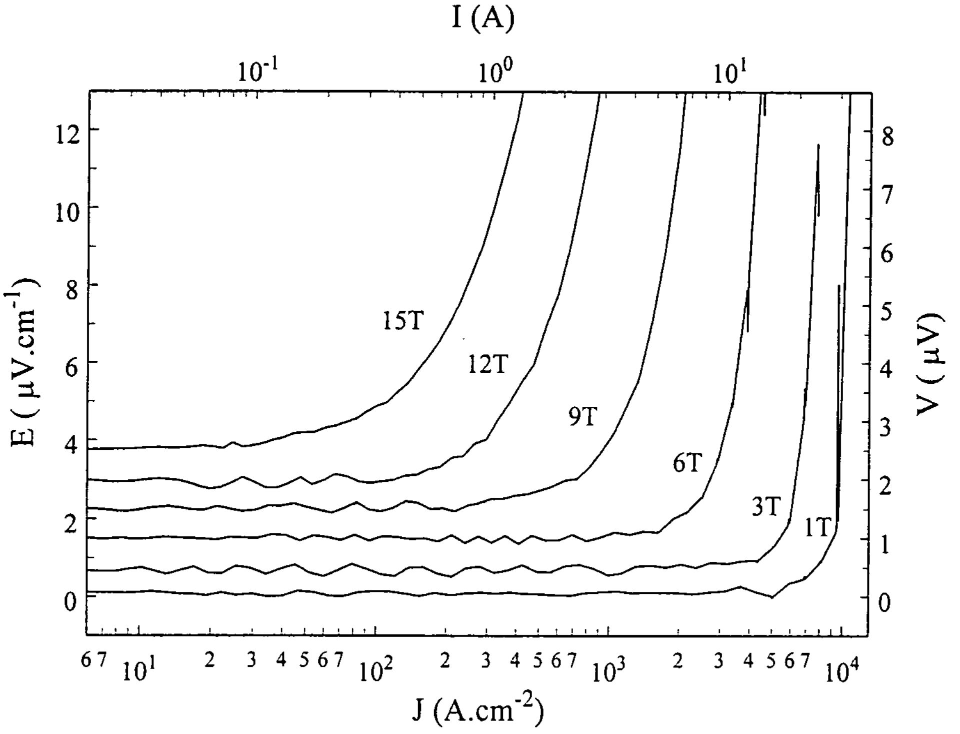

Figure 4.1. The electric field-current density characteristics of a short sample taken at 68 K with field applied (*B*) parallel to a-b planes and perpendicular to current. The individual traces have been offset for clarity.

4.3 Results

Figure 4.1 shows typical *E-J* data taken at 68 K at fields up to 15 T. The figure shows that the base-lines are flat below J_c to within the limits of the experiment and the large range over which current measurements can accurately be made. In Figure 4.2 the field dependence of J_c between 5 and 23 T for both increasing and decreasing fields at 4.2 K is shown for the two orientations in which the Lorentz force operates. In fields up to 20 T, J_c is weakly field dependent and shows the usual hysteretic effect, i.e. in decreasing field J_c is slightly higher than in increasing field. However, above 20 T an inverse hysteresis is observed. This inverse hysteresis has been previously reported and is consistent with the temperature of the sample and the surrounding gas increasing above 4.2 K [5].

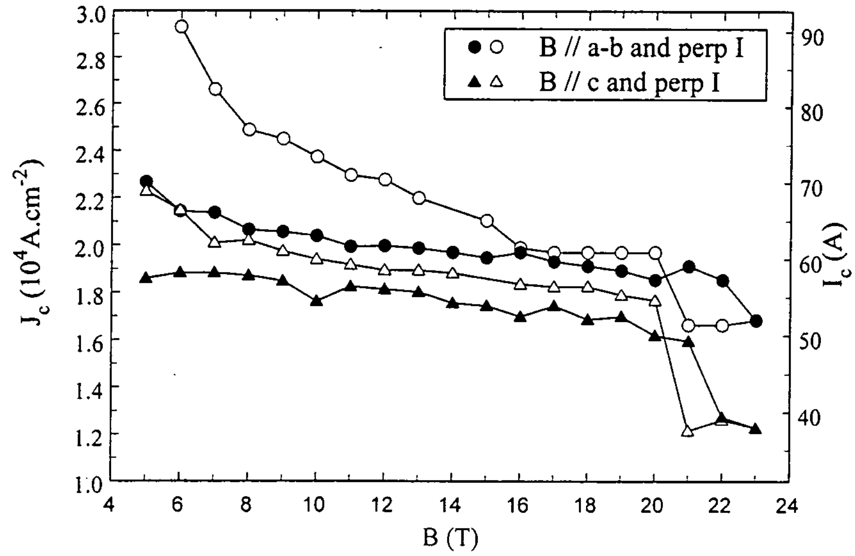

Figure 4.2. The critical current density (J_c) as a function of applied field (B) for 2 orientations of the tape with respect to field from 5 – 23 T at 4.2 K. Open shapes taken in increasing field and closed shapes taken in decreasing field.

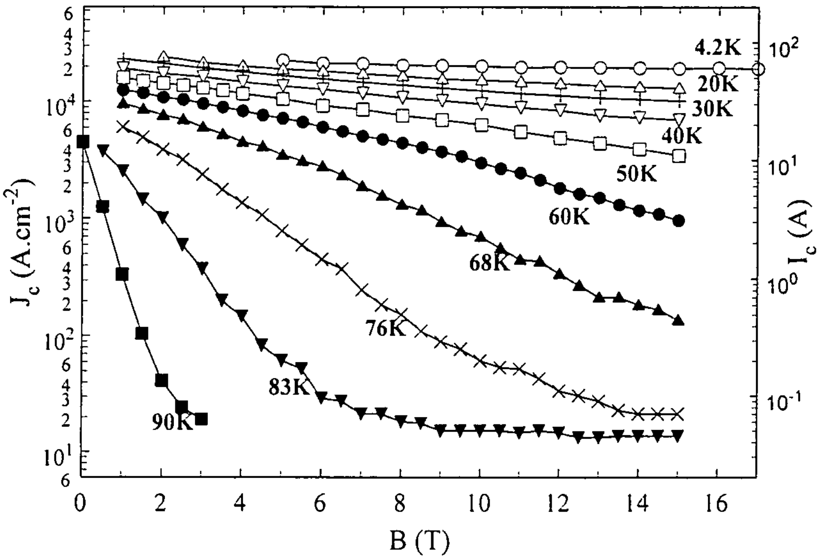

Figure 4.3. The critical current density (J_c) as a function of applied field (B) of a short sample at temperatures from 4.2 K up to 90 K with the field applied parallel to a-b planes and perpendicular to current.

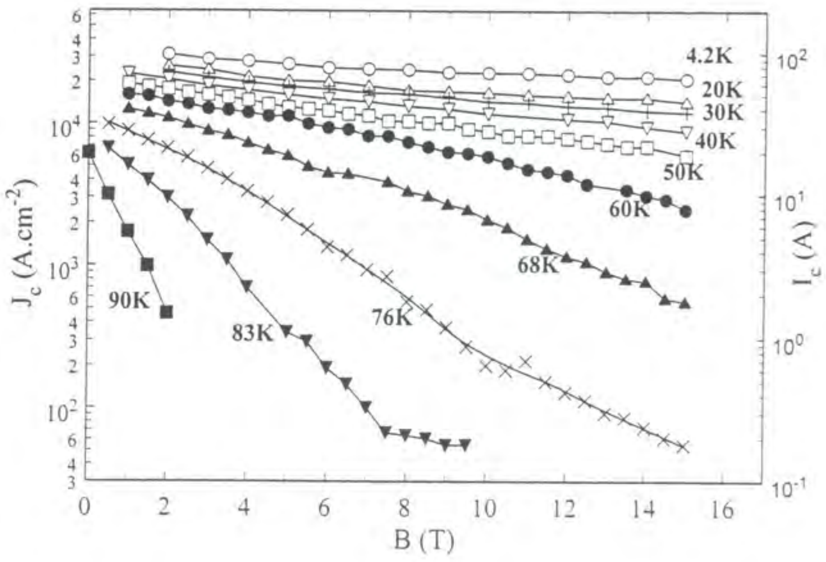

Figure 4.4. The critical current density (J_c) as a function of applied field (B) at temperatures from 4.2 K up to 90 K with field parallel to both a-b planes and current.

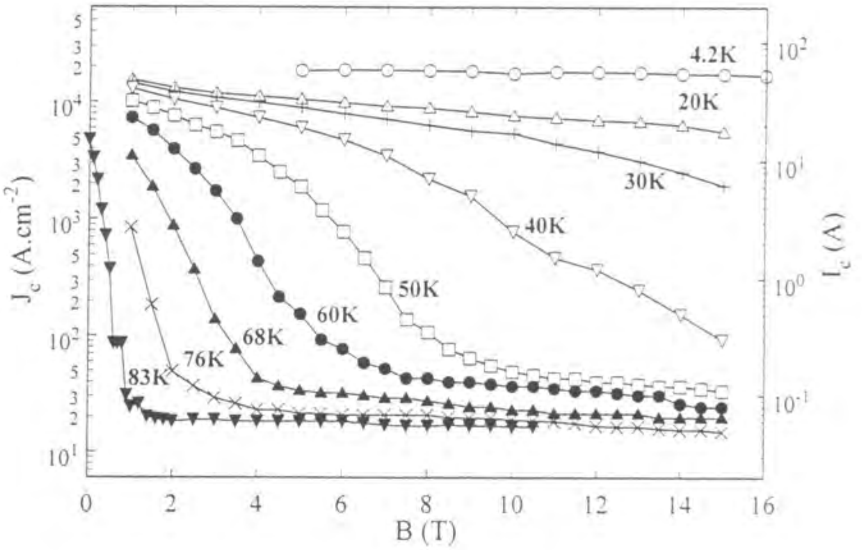

Figure 4.5. The critical current density (J_c) as a function of applied field (B) at temperatures from 4.2 K up to 83 K with field parallel to c-axis and perpendicular to current.

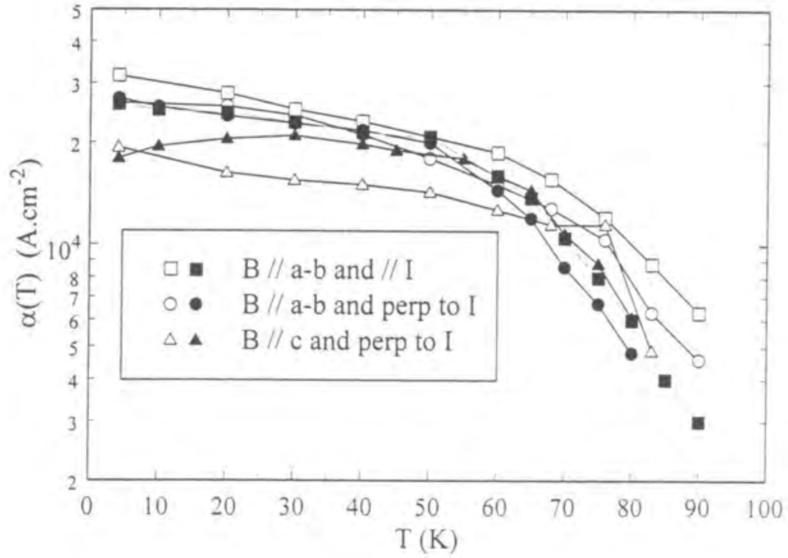

Figure 4.6. The parameter $\alpha(T)$ as a function of temperature for the short sample for 3 orientations of the tape with respect to field, where $J_c(B,T) = \alpha(T)\exp[-B/\beta(T)]$. Closed shapes are taken from Friend [6].

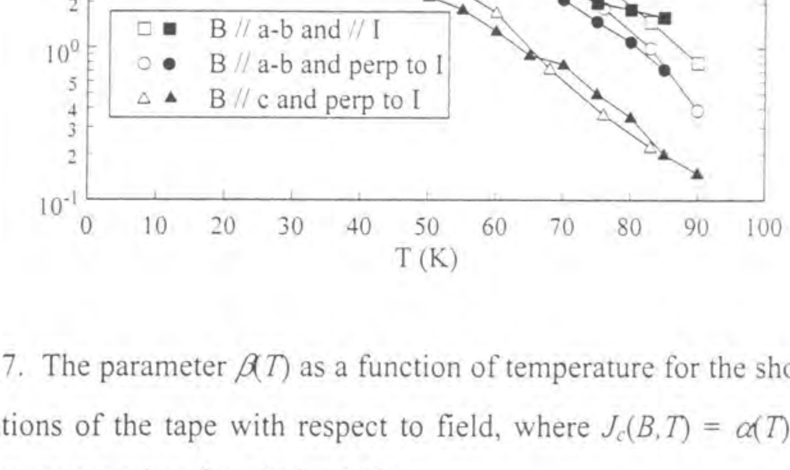

Figure 4.7. The parameter $\beta(T)$ as a function of temperature for the short sample for 3 orientations of the tape with respect to field, where $J_c(B,T) = \alpha(T)\exp[-B/\beta(T)]$. Closed shapes are taken from Friend [6].

In Figures 4.3, 4.4 and 4.5 the J_c field dependence of the tape is shown for fields between 0 and 15 T at temperatures from 4.2 K up to 90 K for 3 orientations of the tape with respect to field. The J_c data at high temperatures that are almost field independent occur when most of the current (at the 1μV.cm^{-1}) is carried in the silver sheath.

4.4 Analysis

The data from Figures 4.3, 4.4 and 4.5 has been fitted at intermediate fields to an exponential function of the form [7]:

$$J_c(B,T) = \alpha(T)\exp[-B/\beta(T)] \qquad \textbf{(4.1)}$$

The parameters $\alpha(T)$ and $\beta(T)$ are plotted in Figures 4.6 and 4.7 for all three orientations of the tape. Also plotted are data taken from Friend et al for the purpose of comparison [6].

4.5 Discussion

By describing the data shown in Figures 4.3-4.5 in terms of an exponential functional form, it facilitates a relatively simple comparison between the high field data presented here and other Bi-2223 tape conductors reported in the literature. Figures 6 and 7 show that the temperature dependence of $\alpha(T)$ and $\beta(T)$ for the data presented in this work and those of Friend et al [6] are similar. However a draw-back of the exponential functional form is that it cannot hold when the applied field is close to the upper critical field. A more complex form for J_c has been proposed which includes three free parameters to describe data measured at the highest fields [3], this model is discussed and applied in detail in Chapter 6. However this is only really useful when the range of measurements of J_c is sufficiently large that there is significant deviation from the simple exponential dependence. Such a deviation is only clearly observed in the B // c-axis data of Figure 4.5.

One of the first questions that must be answered by a complete explanation for the functional form of $J_c(B,T)$ is why the magnitude of J_c is so much lower in tapes than that found in epitaxial thin films [8] or the depairing current [9]. Clearly the grain boundaries play an important role as has been emphasised in the brick-wall [1] and railway switch models [2]. However, even if one only incorporates the most basic properties of these tapes such as the strongly anisotropic nature of these materials and the structure of the grain boundaries, the complexity of these models increases very rapidly. To address this complexity properly, one often needs to know how the properties of the material change on the scale of the coherence length, which for Bi-2223 is approximately the unit cell size. Furthermore, in practice there is inevitably a hierarchy of microstructural factors [10] such that a single mechanism need not necessarily operate throughout the superconducting phase [11]. Recently a simple weak-link diffraction model has been suggested that includes the effective thickness of the grain boundaries as the important free parameter [3]. Whether this model can describe the complexity of these materials is addressed in Chapter 6.

It is clear that extensive measurements over the widest range of current temperature and field are required before we can expect to identify which mechanism determines J_c in these materials. The results presented in this chapter are focused in this direction.

4.6 Conclusions

$J_c(B,T)$ measurements have been completed on a Bi-2223 tape over a very wide range of current, temperature and magnetic field. Measurements have been made with the tape in three orientations with respect to field. The J_c values have been fitted to the exponential form $J_c(B,T) = \alpha(T)\exp[-B/\beta(T)]$ and compared to data in the literature. Chapter 6 includes a more comprehensive analysis of the data reported here to test in more detail the predictions of the models proposed in the literature.

References for Chapter 4

[1] Bulaevskii L, Clem J, Glazman L, and Malozemoff A 1992 *Physical Review B* **45** 2545-2548

[2] Hensel B, Grivel J, Jeremie A, Lerin A, Pollini A, and Flukiger R 1993 *Physica C* **205** 329-337

[3] Hampshire D 1997 *Physica C* **296** 153-166

[4] Friend C and Hampshire D 1995 *Measurement Science and Technology* **6** 98-106

[5] Kitaguchi H, Kumakura H, and Togano K 1995 *Applied Superconductivity* **3** 535-541

[6] Friend C and Hampshire D 1995 *Physica C* **252** 107-116

[7] Le Lay L, Friend C, Maruyama T, Osamura K, and Hampshire D 1994 *Journal of Physics Condensed Matter* **6** 10053-10066

[8] Yamasaki H, Endo K, Kosaka S, Umeda M, Misawa S, Yoshida S, and Kajimura K 1993 *IEEE Transactions on Applied Superconductivity* **3** 1536-1539

[9] Tinkham M, *Introduction to superconductivity* (1996).

[10] Osamura K, Nonaka S, Matsui M, Oku T, Ochiai S, and Hampshire D 1996 *Journal of Applied Physics* **79** 7877-7882

[11] Sun Y, Zhang F, Lu Z, Jiang J, Du J, and Zhang Y 1995 *Physical Review B* **51** 519-522

Chapter 5

Transport measurements taken on Bi-2223 single filaments extracted from an alloy sheathed multifilamentary tape

5.1 Introduction

It is well known that the dependence of critical current density (J_c) on field and temperature can provide information about flux pinning mechanisms within superconductors. Detailed studies of the $J_c(B,T,\theta)$ dependencies of Bi-2223 thin films have been presented [1,2] but despite successful attempts to increase tape J_c, thin film performance remains at least a factor of 3 above the highest tape values [3,4] at 77 K in zero field and far higher in high magnetic fields. Critical current density studies on multifilamentary Bi-2223/Ag tapes [5-7] provide information about the fundamental physics of the materials and their commercial viability. However, the effect of the silver sheath acting as a low resistance shunt tends to conceal the shape of the superconducting transition, as demonstrated in Chapter 4 of this thesis. By removing the silver shunt from the tape the properties of the superconductor can be measured in isolation. There is currently little work in the literature on transport measurements of extracted filaments. Cai et al [8] have presented high field *E-J* data at 50 K and low field data at 77 K on extracted filaments although a comprehensive study of $J_c(B,T)$ is not presented.

The statistics and dynamics of vortices within the high temperature superconductors have also been widely studied. Much of this work has been analysed in terms of the flux creep model [9,10], predicting existence of a finite linear resistivity for all $T > 0$ due to the thermal activation of flux lines out of the pinning wells, or the vortex-glass (VG) model [11,12], which includes disorder in the system and postulates a true superconducting state exhibiting zero linear resistivity ($\rho_{lin}=(E/J)_{J\to 0}=0$).

The first experimental evidence for the existence of the VG phase was observed in YBCO epitaxial films [13] through the scaling of non-linear *E-J* curves around the vortex-glass transition temperature (T_g). Isothermal E-J curves were found to collapse onto two master curves when plotted as $(E/J)/\left|T-T_g\right|^{\upsilon(z+2-D)}$ against $J/\left|T-T_g\right|^{\upsilon(D-1)}$, where z and υ are the dynamic and static critical indices and D represents the dimension of the fluxoids in accordance with the VG model. Later work on YBCO[14-17] and Bi-2223 [18-22] has been analysed in a similar way and further supports the VG model. Studies of E-J characteristics in variable fields at a constant background temperature have also been published [23-27]. In this case a vortex-glass transition field (B_g) is observed defining the transition from glass-liquid behaviour of the flux line lattice. It has been demonstrated that the data by Koch [13] can also be scaled in terms of the flux-creep model [28]. Isothermal scaling of E-J characteristics has more recently been related to the thermodynamic properties of the pinning force density and its statistical distribution in keeping with the flux-creep model [29-31].

In this chapter transport measurements taken on Bi-2223 single filaments extracted from a 37 filament alloy sheathed multifilamentary tape are presented. The tape was fabricated via the powder in tube method with a 28 % fill factor. The average J_c across the Bi-2223 cross-section was 11.8 kA.cm^{-1} at 77 K and zero field. In Section 5.2 the sample fabrication technique is discussed and particular attention drawn to the electrical contacts. A series of E-J data taken at 77 K in fields up to 300 mT with field applied parallel and perpendicular to the filament surface is presented in Section 5.3. A change in curvature in the log$E$-log$J$ characteristics is observed in the c-axis orientated data at 280 mT. An interesting feature of the data taken at 280 mT is that the log$E$-log$J$ characteristics exhibit both positive and negative curvature in different current regions. Current density measurements as a function of field and temperature are also presented for a limited data set between 60 and 90 K in high fields up to 15 T in the field parallel to a-b orientation. A discussion of the results from this work is presented in Section 5.4. It was our intention to obtain a comprehensive data set for all orientations of field. Despite attempting to make good contacts on approximately 100 filaments, it was not possible to obtain a sample with 4 low resistance contacts at cryogenic temperatures. The improvement in sample preparation techniques are outlined below with some suggestions for future work.

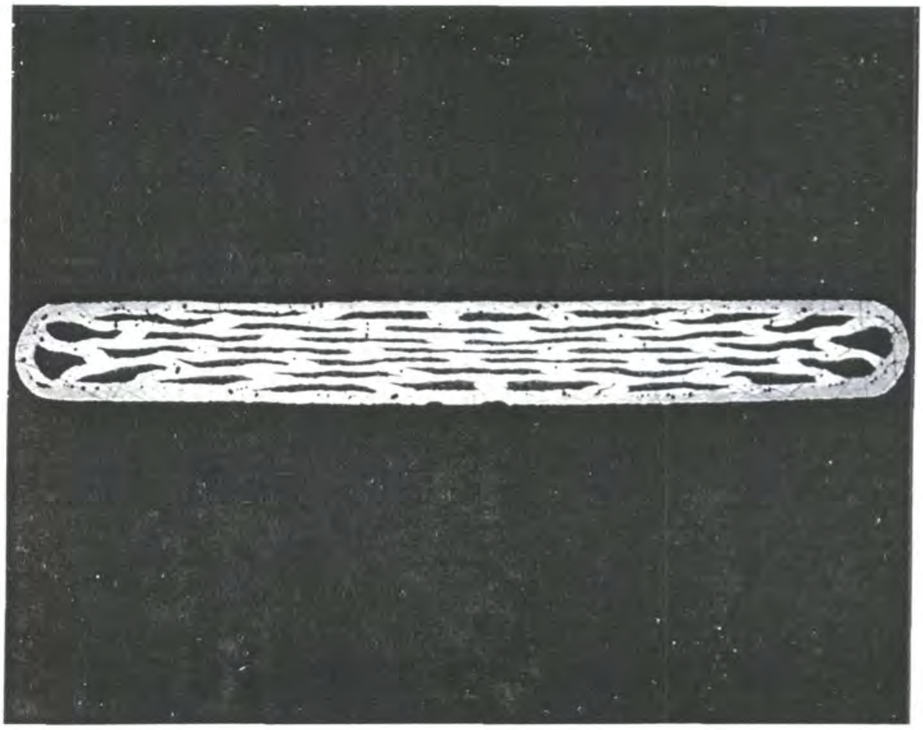

Figure 5.1. A micrograph of a cross-section through the Bi-2223 tape from which the filaments were extracted.

5.2 Experimental

5.2.1 Sample preparation

The cross-sectional geometry of the filaments is strongly dependent on position within the tape as seen in Fig. 5.1. This is probably due to a variation in rolling pressure during fabrication. The samples reported in this chapter are believed to have been extracted from the outer regions of the tape since filaments in the centre regions were not extractable using this etching technique. Since no microscopy study has been carried out on the individual filaments reported in this work, it is assumed that all filaments in the tape have an equal cross-sectional area of 8.24×10^{-3} mm^2. Figure 5.1 suggests that there may be an error of up to ± 10 % due to this assumption. Samples were typically cut to 8 mm in length. In measuring critical current density using a four-terminal technique, low electrical resistance contacts are essential for voltage taps, to minimise electrical noise, and current leads, to minimise thermal gradients across the sample. Contact resistances below 50 Ω are required (and preferably below 5 Ω) for all contacts for these experiments.

A solution of ammonium hydroxide and hydrogen peroxide [32] was used to dissolve the alloy sheath from the tape, extracting the filaments. Complete removal of the etching solution was essential in order that silver paint contacts were not dissolved by any remaining silver etch solution. After the filaments were removed from the etching solution, three different approaches were tried to dilute any solution remaining on filament surface and pores and to make electrical contacts:

i) The filaments were soaked in water for 24 hours and all electrical contacts were made using silver paint to contact the surface of the filament. However the silver paint current contacts were only able to support currents below 80 mA in liquid nitrogen with higher currents leading to contact 'burn out', target currents were around 300 mA.

ii) A better electrical contact to the surface could be produced using gold sputtering. Gold was not required for the voltage taps since they carried no current and the silver paint provided a sufficiently low resistance. During sputtering the centre region of the sample was masked exposing only the regions to which the current leads would be contacted. A gold layer of thickness around 20 nm was applied to the unmasked regions. The sputtered sample was laid across 4 copper pads mounted on tufnol. Electrical wires were connected to each of the copper pads using silver paint. Connections were subsequently made between the filament and the pads using silver paint ensuring that the paint ran completely around the sample. Efforts were made to contact to the cross-section of the filament with the current leads in an attempt to access directly the a-b planes. The paint dried for 3 hours at room temperature. A distance of 2 mm was exposed between the voltage taps. The sample was finally encapsulated with stycast to strengthen against Lorentz forces and to increase the thermal mass for cooling purposes. This is the procedure used to obtain all data presented in this Chapter.

iii) In this preparation technique, the filaments were soaked in the solvent used to dilute the silver paint (4-methyl-2-pentanone). This solvent evaporated from the filament (and pores) after removal and eliminated the possibility of water residue.

A regularly observed phenomenon for filaments prepared using procedure (i) and (ii) was a decrease in the resistance of the current contacts during the first current cycle up to 100 mA. Once the joint resistance had decreased it remained below the experimental limit through further current and thermal cycles. This phenomenon is believed to be due to a high resistance oxide layer between the sample and the contact being burnt off at high currents. The silver paint voltage contacts tended to burn out at a few mA thus this technique could not be used to reduce voltage tap contact resistance. On the basis of this evidence several samples were heated to temperatures above 100°C immediately before the silver paint contacts were applied. This technique increased the probability of an initial low resistance contact from 50 % to 75 % although no measurements were taken on samples fabricated in this way.

The probability of successfully fabricating and cooling a sample with 4 low resistance contacts was very low for all preparation techniques. For example for technique (ii), the probability of obtaining an initial low resistance contact between the silver paint and the filament was 50 %. Application and drying of the stycast presented a further 50 % risk of damaging atleast one contact per sample. Finally cooling from room temperature to 77 K over 30 minutes resulted in 30 % of the samples increasing contact resistances above the 50 Ω experimental limit. Therefore the overall probability of obtaining a sample suitable with all four contacts suitable for high precision data was about 2 %.

5.2.2 Experimental procedure

Transport critical currents were measured using a conventional four-probe dc method. A Keithley 182 nanovoltmeter was used to read the voltage across the sample and a 30 V variable voltage source across a variable resistor controlled the current. 77 K data was taken in liquid-nitrogen using a 300 mT copper magnet. All variable temperature data was taken in Durham using a variable temperature insert (VTI) within a 15 / 17 T superconducting magnet.

5.3 Results

In Figure 5.2 the log*E*-log*J* characteristics for a c-axis orientated single filament are presented at 77 K in background fields between 20 to 280 mT at intervals of 20 mT. Current densities have been calculated assuming all filaments from the tape have an equal cross-section of 8.24 x 10^{-3} mm^2. Thermal voltages due to the contact resistances have been fitted to a fourth order polynomial equation and subtracted from the data. The noise level on the data is ± 70 nV. All log*E*-log*J* curves taken in fields below 260 mT exhibit systematic negative curvature. The 280 mT trace exhibits positive curvature above 10 mA however below 10 mA negative curvature is observed. The curvature in the traces is confirmed in Figure 5.3 by plotting $d(\log(E))/d(\log(J))$ against $\log(J)$. In this plot a negative gradient corresponds to negative curvature in the log*E*-log*J* characteristics, zero gradient corresponds to zero curvature and a negative gradient corresponds to negative curvature. The 280 mT exhibits positive curvature for $-2.0 < \log(I)$ and negative curvature exhibited for $\log(I) < -2.0$. No positive curvature is observed in any of the traces taken in fields below 270 mT. Linear *E*-*J* plots of data taken above 220 mT on the c-axis orientated sample are presented in Figure 5.4. These data confirm that the change in curvature observed in the log*E*-log*J* characteristics at 280 mT at low currents is not due to experimental noise. By extrapolating the positive curvature region of the 280 mT in Fig. 5.2 trace to low currents an electric field of around 1 $\mu\text{V.cm}^{-1}$ may be expected at 5 mA. This value is clearly above the baseline in the linear plot and confirms that the observed change in curvature cannot be attributed to noise in the measurement.

In Figure 5.5 the log*E*-log*J* curves are presented for the a-b orientated sample at 77 K in background fields up to 300 mT. Data is presented at intervals of 10 mT below 60 mT and in 20 mT intervals above 60 mT. The critical current density (J_c) values for both orientations at 77 K are presented in Figure 5.6 using a criterion of 1.5 $\mu\text{V.cm}^{-1}$. After an initial decrease in J_c at low field, both orientations exhibit an exponential decrease in J_c. At a field close to 280 mT the J_c dependence in the c-axis

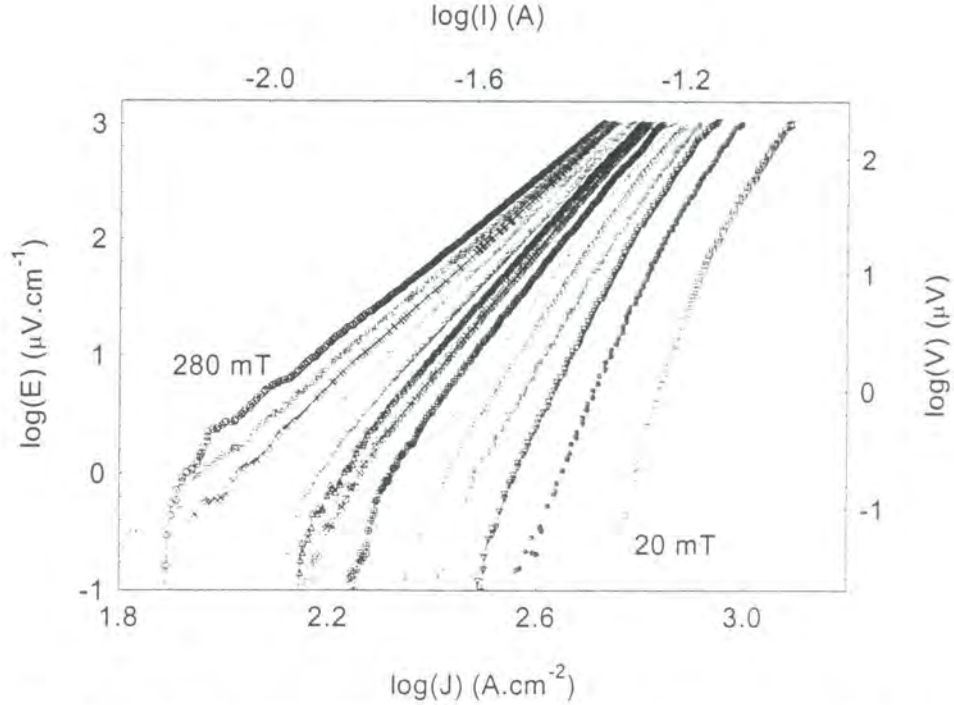

Figure 5.2 log*E*-log*J* characteristics of a single filament with field applied perpendicular to the filament surface. Data taken at 77 K in fields between 20 – 280 mT, traces taken in 20 mT intervals.

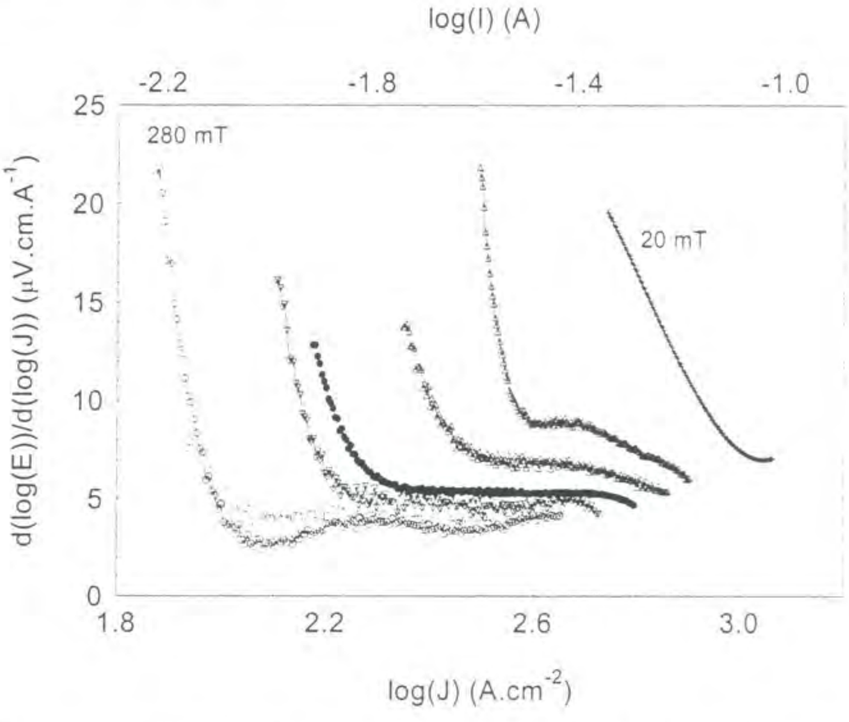

Figure 5.3. d(log(*E*))/d(log(*J*)) against log(*J*) of the single filament data taken at 77 K with field applied parallel to the c-axis. Data shown at 20, 60, 100, 160, 200, 240 and 280 mT.

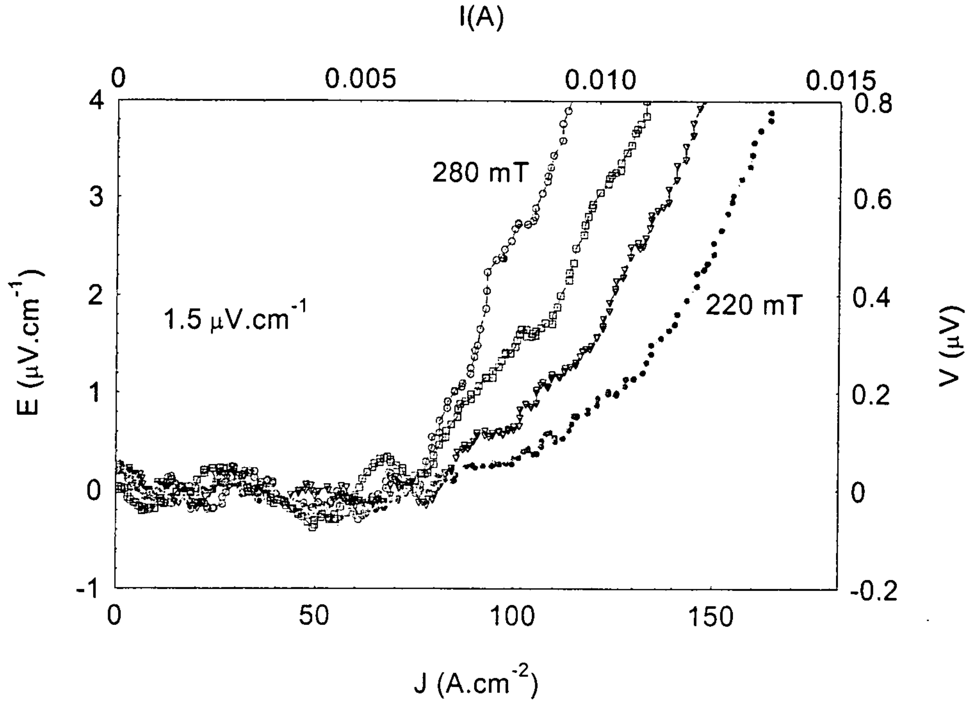

Figure 5.4. Linear E-J characteristics for the c-axis orientated sample in fields between 220 – 280 mT in 20 mT intervals at 77 K.

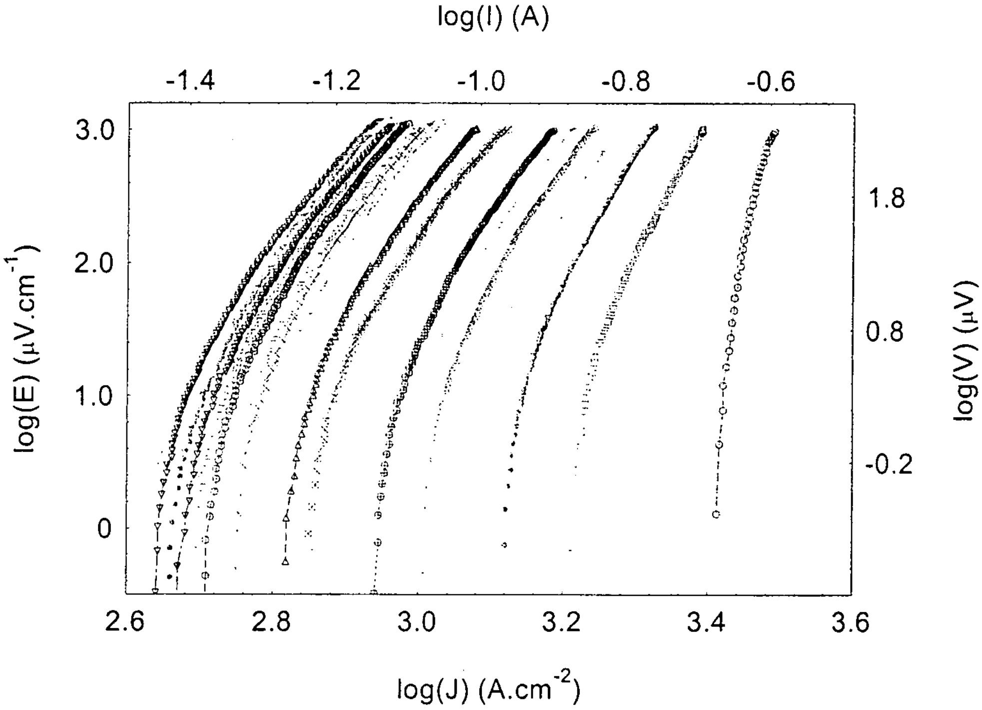

Figure 5.5. log$E$-log$J$ characteristics of a single filament with field applied parallel to the filament surface. Data taken at 77 K in background fields from 0 – 300 mT. Traces are presented every 10 mT up to 60 mT and then in 20 mT intervals up to 300 mT.

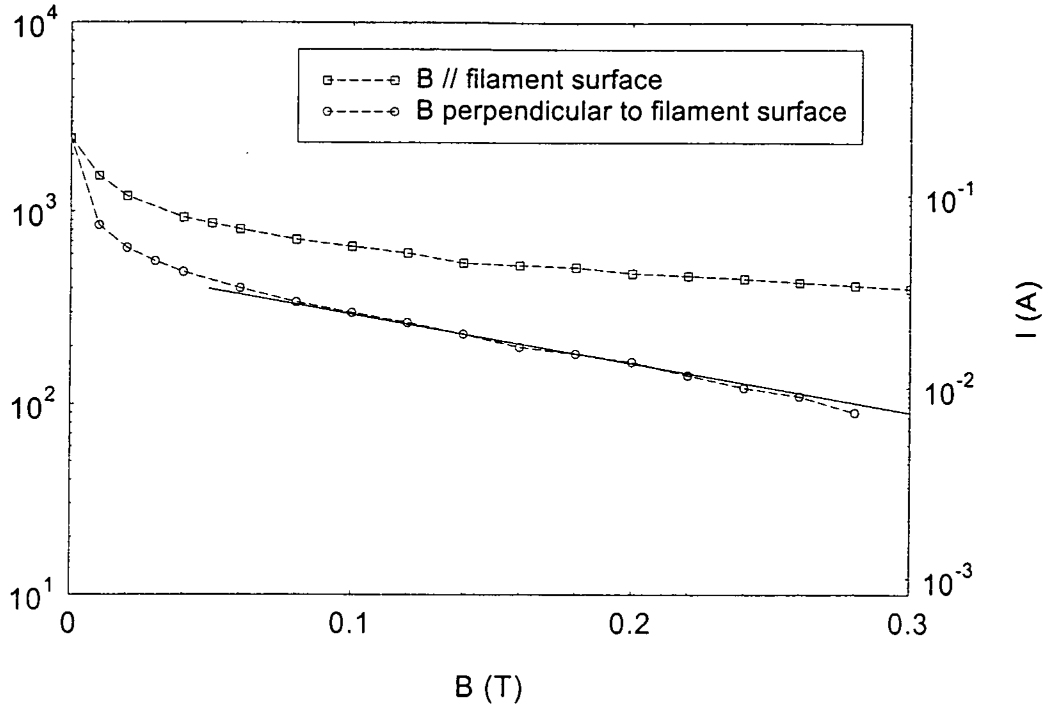

Figure 5.6. Critical current density (J_c) as a function of field for the single filament at 77 K with the field applied parallel and perpendicular to the filament surface. J_c is determined using a criterion of 1.5 μV.cm^{-1}.

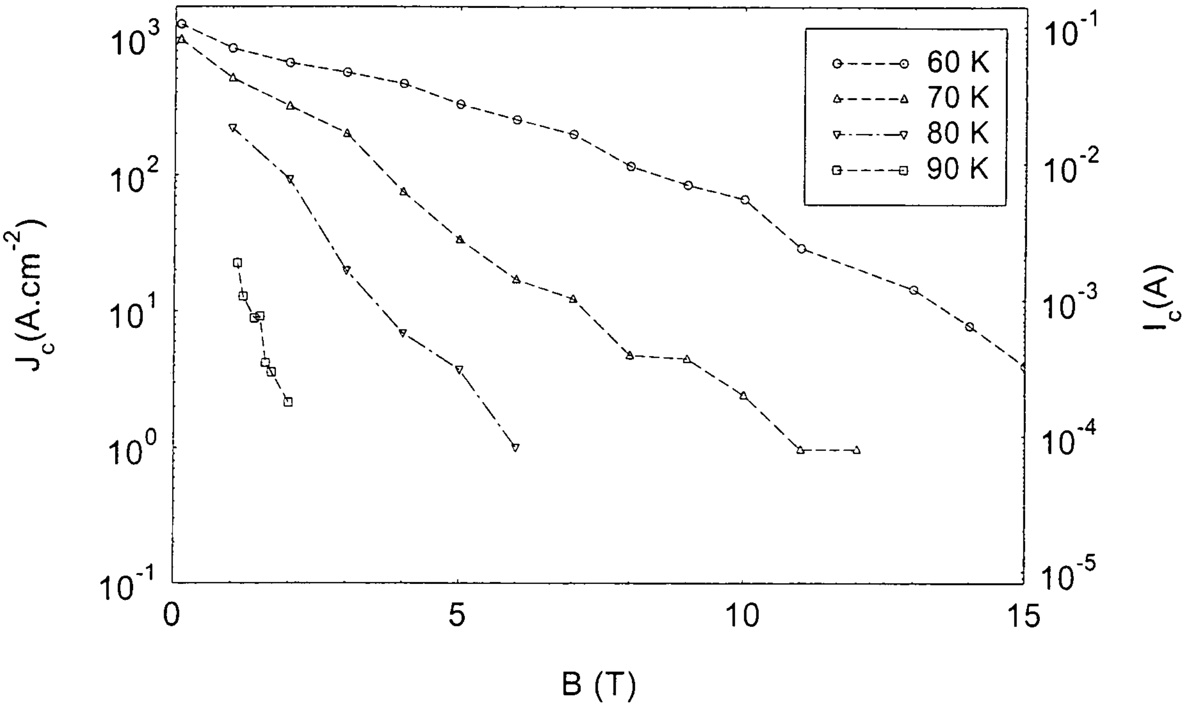

Figure 5.7. Critical current density (J_c) as a function of field and temperature for a single filament with field applied parallel to the filament surface. J_c was determined using a criterion of 10 μV.cm^{-1}.

orientated data deviates from the exponential form and begins to drop more sharply. The initial drop in J_c which has previously been observed [24,25] can be attributed to weakly coupled grain boundaries with diminishing current carrying capabilities as the field is increased.

J_c characteristics of a different a-b orientated filament are presented in Figure 5.7 in fields up to 15 T and at temperatures between 60 to 90 K. The contact resistance of the voltage taps was increased during cooling thus increasing the noise on the measurement and reducing the accuracy of data in the low current region below 0.1 mA. A J_c criterion of 10 μV.cm^{-1} was used for these data due to increased noise levels on the data. Agreement of critical current density between the data at 80 K and the 77 K data obtain in liquid nitrogen, show that there is reliable temperature control within the VTI.

5.4 Discussion

The single filament J_c at 77 K and zero field is calculated as 2.45 kA.cm^{-2}, a factor of about 5 less than the average Bi-2223 J_c within the tape. Several groups have investigated the distribution of critical current density within the cross-section of multifilamentary tapes using sliced tapes [33-35] and magneto optical imaging [36,37] and also within individual filaments [38]. The most compelling data has shown a variation in cross-section of filament depending on the position within the tape[39] and found that the most deformed filaments, appearing in the centre of the tape, have the highest J_c [33,35,39] up to a factor of 10 higher than those found in the outer regions. These reasons are believed to explain the factor of 5 difference between the average J_c across the superconductor in the sheathed tape and the measured filament at 77 K in self-field.

E-J characteristics of HTS materials over wide field and temperature ranges have previously been used to investigate the vortex glass-liquid phase transition [14-22]. Fisher's vortex-glass theory predicts that in the vortex-glass regime ($T < T_g$ or $B < B_g$) the log$E$-log$J$ curves exhibit negative curvature, corresponding to a vanishing linear resistivity as J approaches zero [11,12]. In the vortex-liquid regime ($T > T_g$ or

$B > B_g$) the theory predicts a finite linear resistivity for small J exhibited as positive curvature in the log$E$-log$J$ characteristics. A similar change in curvature is observed at high currents between 260 and 280 mT in the c-axis orientated data presented in Figure 5.2. However at low currents, the 280 mT trace also exhibits negative curvature in contradiction with Fisher's vortex glass theory. A close inspection of the data presented by Shibutani et al [24] and Li et al [27] shows a similar change in curvature to that observed at 280 mT although the feature was not discussed.

The arguments presented above and the published data [24,27] produce evidence for a zero resistance phase at fields above B_g. More data is required in fields above B_g extending to lower currents and voltages in order to make firmer conclusions. The variable temperature and field data presented in Figure 5.7 show the scope to obtain data in the Durham system. We suggest that in future measurements, the silver paint solvent is used to soak the filaments after they have been etched. The filaments should then be heated to 100 C and a thick layer of gold should be deposited for the current leads. It is intended that that in future the fabrication procedure and experimental system developed in this work may be used to achieve a comprehensive study of the $J_c(B,T)$ dependence for Bi-2223 filaments over a large range of temperatures and fields.

5.5 Conclusions

High quality transport measurements have been taken on Bi-2223 single filaments extracted from an alloy sheathed multifilamentary tape. Data has been taken in liquid nitrogen at 77 K in fields up to 300 mT with the field aligned parallel to the c-axis and a-b planes. Further data has been taken in a variable temperature insert at temperatures between 60 to 90 K in fields up to 15 T with the field aligned with the a-b planes. c-axis orientated log$E$-log$J$ characteristics at 77 K shows a change in curvature at 280 mT similar data has previously been attributed to the vortex glass-liquid transition. An interesting feature of the data taken at 280 mT is that the log$E$-log$J$ characteristics exhibit both positive and negative curvature in different current regions. The $I_c(B)$ dependence of the c-axis orientated data provides further evidence for the vortex glass-liquid transition at 280 mT. Transport measurements taken between 60 to 90 K in fields up to 15 T show the range of measurements obtainable in future studies and good agreement in J_c has been observed between data taken in liquid-nitrogen and in the variable temperature insert. The single filament J_c is a factor of 5 lower than the Bi-2223 average within the tape.

References for Chapter 5

[1] Yamasaki H, Endo K, Kosaka S, Umeda M, Misawa S, Yoshida S, and Kajimura K 1993 *IEEE Transactions on Applied Superconductivity* **3** 1536-1539

[2] Yamasaki H, Endo K, Nakagawa Y, Umeda M, Kosaka S, Misawa S, Yoshida S, and Kajimura K 1992 *Journal of Applied Physics* **72** 2951-2957

[3] Malozemoff A, Carter W, Fleshler S, Fritzemeier L, Li Q, Masur L, Miles P, Parker D, Parrella R, Podtburg E, Riley G, Rupich M, Scudiere J, and Zhang W 1999 *IEEE Transactions on Applied Superconductivity* **9** 2469-2474

[4] Li Q, Brodersen K, Hjuler H, and Freltoft T 1993 *Physica C* **217** 360-366

[5] Sneary A, Friend C, Vallier J, and Hampshire D 1999 *IEEE Transactions on Applied Superconductivity* **9** 2585-2588

[6] Sato K, Hikata T, and Iwasa Y 1990 *Applied Physics Letters* **57** 1928-1929

[7] Ohkura K, Sato K, Ueyama M, Fujikami J, and Iwasa Y 1995 *Applied Physics Letters* **67** 1923-1925

[8] Cai X, Polyanskii A, Li Q, Riley G, and Larbalestier D 1998 *Nature* **392** 906-909

[9] Anderson P 1962 *Phys. Rev. Lett.* **9** 309-311

[10] Anderson P and Kim Y 1964 *Reviews of Modern Physics* **36** 39-43

[11] Fisher M 1989 *Phys. Rev. Lett.* **62** 1415-1418

[12] Fisher D, Fisher M, and Huse D 1991 *Physical Review B* **43** 130-159

[13] Koch R, Foglietti V, Gallagher W, Koren G, Gupta A, and Fisher M 1989 *Phys. Rev. Lett.* **63** 1511-1514

[14] Worthington T, Olsson E, Nichols C, Shaw T, and Clarke D 1991 *Physical Review B* **43** 10538-10543

[15] Gammel P, Schneemeyer L, and Bishop D 1991 *Phys. Rev. Lett.* **66** 953-956

[16] Dekker C, Woltgens P, Koch R, Hussey B, and Gupta A 1992 *Phys. Rev. Lett.* **69** 2717-2720

[17] Wang Z, Zhang H, and Cao X 2000 *Physica C* **337** 62-66

[18] Li Q, Weismann H, Suenga M, Motowidlow L, and Haldar P 1994 *Physical Review B* **50** 4256-4259

[19] Yamasaki H, Endo K, Kosaka S, Umeda M, Yoshida S, and Kajimura K 1994 *Physical Review B* **50** 12959-12965

[20] Yamasaki H, Endo K, Kosaka S, Umeda M, Yoshida S, and Kajimura K 1995 *Cryogenics* **35** 263-269

[21] Mawatari Y, Yamasaki H, Kosaka S, and Umeda M 1995 *Cryogenics* **35** 161-167

[22] Yamasaki H, Endo K, Mawatari Y, Kosaka S, Umeda M, Yoshida S, and Kajimura K 1995 *IEEE Transactions on Applied Superconductivity* **5** 1888-1891

[23] Shibutani K, Wiesmann H, Sabatini R, Suenga M, Hayashi S, Ogawa R, Kawate Y, Motowidlo L, and Haldar P 1994 *Applied Physics Letters* **64** 924-926

[24] Shibutani K, Li Q, Sabatini R, Suenga M, Motowidlo L, and Haldar P 1993 *Applied Physics Letters* **63** 3515-3517

[25] Li Q, Wiesmann H, Suenga M, Motowidlo L, and Haldar P 1995 *IEEE Transactions on Applied Superconductivity* **5** 1713-1716

[26] Li Q, Wiesmann H, Suenga M, Motowidlo L, and Haldar P 1995 *Applied Physics Letters* **66** 637-639

[27] Li Q, Wiesmann H, Suenga M, Motowiglo L, and Haldar P 1995 *Physical Review B* **51** 701-704

[28] Coppersmith S, Inui M, and Littlewood P 1990 *Phys. Rev. Lett.* **64** 2585

[29] Yamafugi K and Kiss T 1996 *Physica C* **258** 197-212

[30] Yamafuji K and Kiss T 1997 *Physica C* **290** 9-22

[31] Kiss T, Matsushita T, and Irie F 1999 *Superconductor Science and Technology* **12** 1079-1082

[32] Strano G, Siri A, and Grasso G 2000 *Superconductor Science and Technology* **13** 1470-1475

[33] Polak M, Majoros M, Kasztler A, and Kirchmayr H 1999 *IEEE Transactions on Applied Superconductivity* **9** 2151-2154

[34] Grasso G, Hensel B, Jeremie A, and Flukiger R 1995 *Physica C* **241** 45-52

[35] Larbalestier D, Cai X, Feng Y, Edelman H, Umezawa A, Riley Jr G, and Carter W 1994 *Physica C* **221** 299-303

[36] Welp U, Gunter D, Crabtree G, Zhong W, Balachandran U, Haldar P, Sokolowski R, Vlasko-Vlasov V, and Nikitenko V 1995 *Nature* **376** 44-46

[37] Pashitski A, Polyanskii A, Gurevich A, Parrell J, and Larbalestier D 1995 *Physica C* **246** 133-144

[38] Sivakov A, Lukashenko A, Turutanov O, Dmitrenko I, Abraimov D, Muller P, and Ustinov A 2000 *Physica B* **284-288** 2071-2072

[39] Schuster T, Kuhn H, Weibhardt A, Kronmuller H, Roas B, Eibl O, Leghissa M, and Neumuller H 1996 *Applied Physics Letters* **69** 1924-1956

Chapter 6

The Useful Limit for the Critical Current Density in Bi-2223 tapes

6.1 Introduction

It is generally believed that the critical current density (J_c) in high magnetic fields achieved in state-of-the-art Bi-2223 tapes is substantially below its optimum, perhaps two or three orders of magnitude [1]. In zero applied field at 77 K, there is only about a factor of 4 difference between J_c(0 T, 77K) in the best short samples of Bi-2223 tapes ($J_c \sim 7.3 \times 10^4$ Acm^{-2}) [2,3] and the best Bi-2223 thin films ($J_c \sim 3 \times 10^5$ Acm^{-2}) [4]. Given the larger self-field in the tapes, it is probable that J_c(0 T, 77K) in the best filaments (were they measured in isolation) is already similar to the best films. The question arises why the high magnetic field J_c values are so different. The relatively high porosity and cracks in tapes [5] certainly contributes to reducing J_c but the high zero-field J_c values suggest that in the best tapes that this is not the primary consideration. The excellent work pioneered by Dimos on bicrystals grain-boundaries showed that J_c can be reduced by a few orders of magnitude if the grain boundaries are misaligned even by a few degrees [6,7]. This has led to the concept of weak links and strong links [8,9]. It is considered that the weak link connections only carry current in low fields. In high magnetic fields, most of the grain boundary provides a barrier to current flow so that only a small strong-link cross-sectional area is active. This chapter provides a comparison between the high field J_c in Bi-2223 tapes and Bi-2223 films. Calculations for J_c are provided that would be expected in a fully dense tape with no grain boundaries using a curved film model. This allows a quantitative estimate of the degree to which the grain boundaries in tapes act as barriers in high magnetic fields. The calculations are compared to comprehensive variable temperature variable field J_c data obtained for a Bi-2223 tape. The implications of this comparison for magnet technology are discussed.

In Section 6.2, comprehensive variable-temperature high magnetic field J_c data for Bi-2223 tapes are presented and compared to a strong pinning flux creep model [10] and a weak-link model [11]. Such comparison addresses the mechanism that determines J_c in tapes. In Section 6.3, the basic assumptions of the curved film model are outlined and the field and temperature dependence of J_c calculated. In Section 6.4, the experimental tape and calculated curved film J_c values are compared and the implications for fabricating tapes for high field magnet technology discussed. The conclusions from this work are presented in Section 6.5.

6.2 The Critical Current Density of Bi-2223 Tapes

In high fields and temperatures where the index of the E-J transition is low (where $E \propto J^n$, n: index), if J_c is defined using an electric field criterion, a low resistance metal in principle carries a supercurrent since there is a finite current density at finite E-field. In Bi-2223, such an E-field definition for J_c does not distinguish the contribution from the superconductor and low normal state resistivity silver alloy matrix [12]. Despite this drawback, for engineering applications the properties of the entire composite conductor is required so the electric field criterion is the most commonly used. However in basic studies of critical current density, the properties of the superconductor alone are required. The comprehensive critical current density data on Bi-2223 presented in Chapter 4, that were analysed at 1.5 μV.cm^{-1}, have been reanalysed using the offset criterion for J_c [13]. A line is drawn between the E-field criteria 1.5 and 0.75 μV.cm^{-1} and extrapolated to zero which defines J_c as shown in Fig. 6.1. The $J_c(B,T)$ dependence for the Bi-2223 tape in 3 orientations with respect to field are presented in Figs. 6.2 – 6.4 defined using the offset criterion. The data are compared with the predictions from a strong pinning - flux creep model [1,10] and a weak link model [11]. The accuracy of the temperature is expected to be ± 3 K and the error in the J_c values is ± 3 %.

Collective pinning – flux creep (FC) theories which include the effects of thermal fluctuations have been used to predict the functional form of $J_c(B)$[10] where [1]:

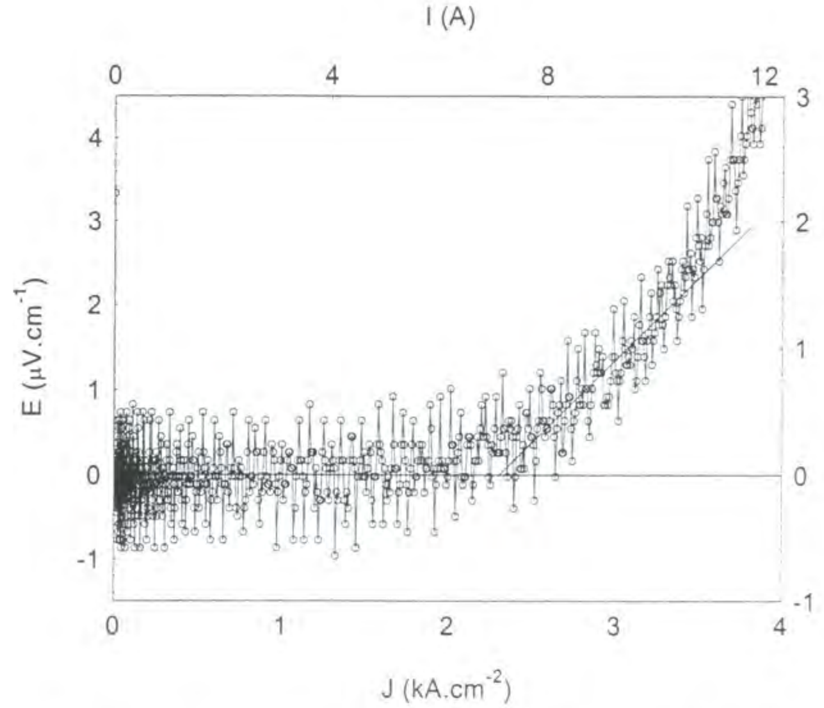

Figure 6.1. The electric field (E) - current density (J) characteristics for the Bi-2223 tape at 76 K and 2.5 T for B parallel to the a-b planes and orthogonal to current. The straight line shown is determined using the offset criterion procedure for finding a critical current density at a nominal zero electric field.

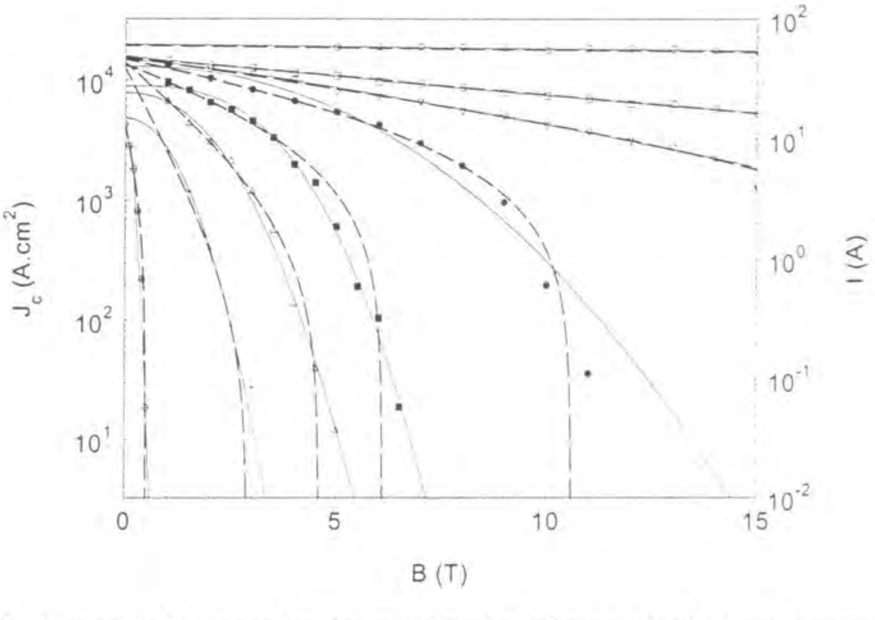

Figure 6.2. The critical current density as a function of magnetic field and temperature for the Bi-2223 tape with the field applied orthogonal to the surface of the tape and perpendicular to the direction of current flow. The solid line is fitted using the flux creep model and the dashed line the weak-link diffraction model. Data at 4.2 K (o), 20 K (□), 30 K (∇), 40 K (●), 50 K (■), 60 K(Δ), 68 K (+) and 83 K (⊕).

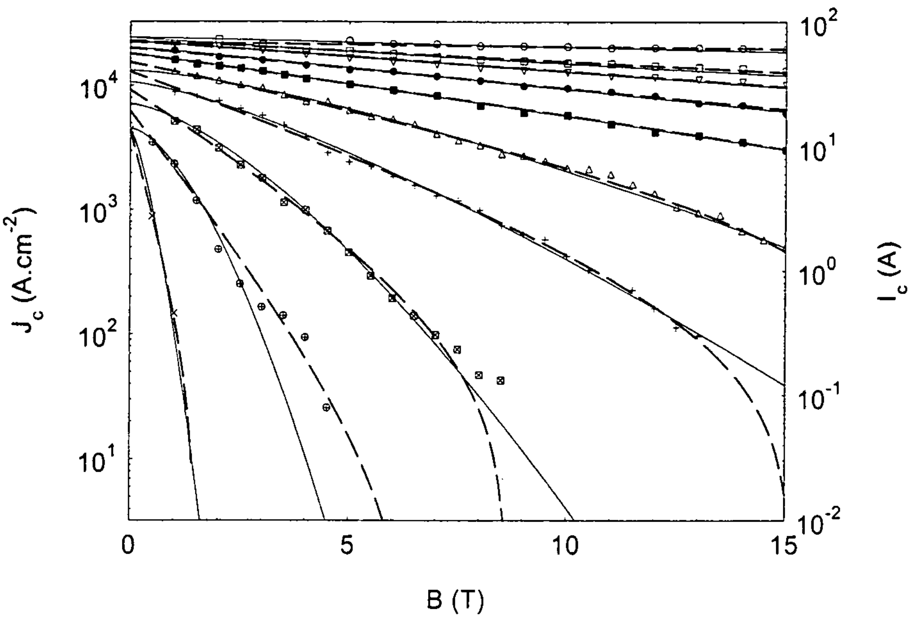

Figure 6.3. The critical current density as a function of magnetic field and temperature for the Bi-2223 tape with the field applied parallel to the surface of the tape and perpendicular to the direction of current flow. The solid line is fitted using the flux creep model and the dashed line the weak-link diffraction model. Data at 4.2 K (o), 20 K (□), 30 K (∇), 40 K (●), 50 K (■), 60 K (Δ), 68 K (+), 76 K (⊠), 83 K (⊕) and 90 K (×).

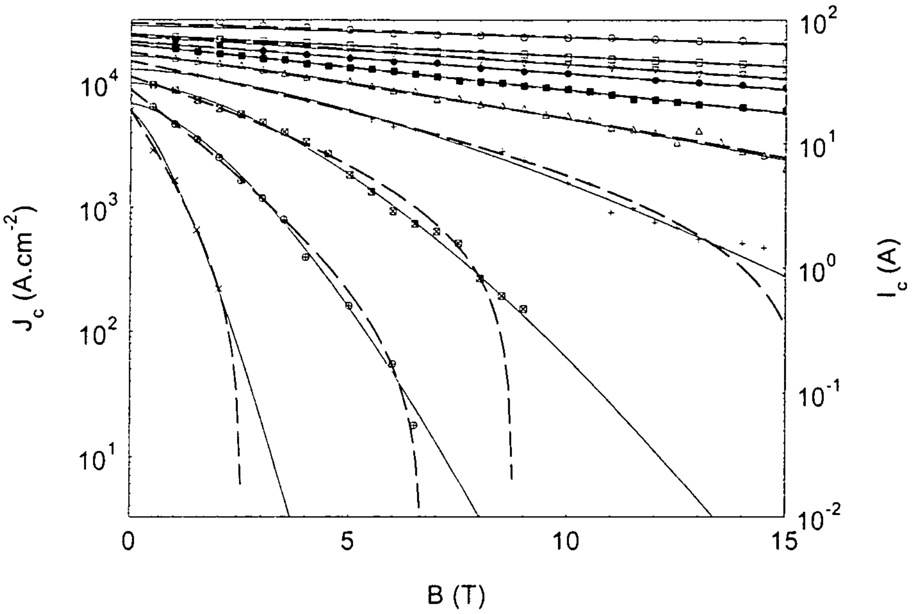

Figure 6.4. The critical current density as a function of magnetic field and temperature for the Bi-2223 tape with the field applied parallel to the surface of the tape and parallel to the direction of current flow. The solid line is fitted using the flux creep model and the dashed line the weak-link diffraction model. Data at 4.2 K (o), 20 K (□), 30 K (∇), 40 K (●), 50 K (■), 60 K (Δ), 68 K (+), 76 K (⊠), 83 K (⊕) and 90 K (×).

$$J_c(B,T) = J_0 \exp\left[-(B/B_0)^{\upsilon}\right] \tag{6.1}$$

where J_0 is the critical current through strong links at zero field and B_0 and υ are related to pinning characteristics of the tape. The parameter υ affects the curvature of the $J_c(B)$ dependence. For $\upsilon = 1$ the exponential form is observed, for $\upsilon < 1$ positive curvature and for $\upsilon > 1$ negative curvature. The contribution from weak linked grains is completely ignored in this model [14]. The functional form (solid lines in Figs. 6.2-6.4) provides a reasonable fit to the data for the 3 orientations of the sample with respect to field. In Figs. 6.5, 6.6 and 6.7, the free parameters J_0, B_0 and υ in the collective pinning – flux creep model are presented as a function of temperature. In the captions, B // a-b and B // c correspond to field applied parallel and perpendicular to the tape surface respectively.

The J_c data have also been compared to the predictions of the weak-link diffraction (WL) model [11]. This model assumes strong intragranular pinning with no pinning operating along the grain boundaries. The functional form of $J_c(B,T)$ is given by

$$J_c(B,T) = \alpha(T)\left(1 - \frac{B}{B_{c2}(T)}\right)\exp\left(\frac{-B}{\beta(T)}\right) \tag{6.2}$$

where $\alpha(T)$, β(T) and $B_{C2}(T)$ are taken as free parameters. In the original work a diffraction argument was used to specify $\alpha(T)$. However in this work it is left as a free parameter to account for cracks and grain-boundaries acting as barriers. The factor $(1-B/B_{C2})$ accounts for the reduction of the order parameter in the grains where $B_{C2}(T)$ is the upper critical field. The parameter $\beta(T)$ accounts for the effective width of the grain boundaries following the phenomenological pair-breaking S-N-S model of Hsiang and Finnemore [15]. In Figs. 6.2, 6.3 and 6.4 the short sample data have also been fitted to the WL model. There is good agreement between the data and the model. Figs. 6.8 and 6.9 show the temperature dependence of the free parameters from the WL model.

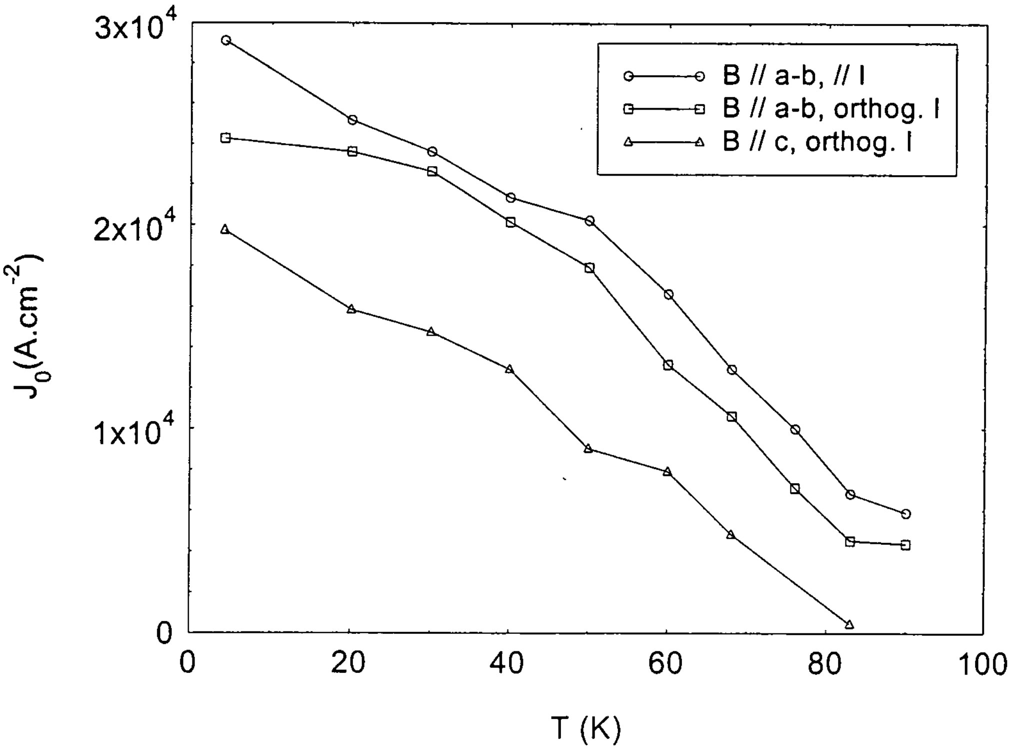

Figure 6.5. The parameter J_0 versus temperature from the flux creep model for the three orientations of the tape with respect to the magnetic field.

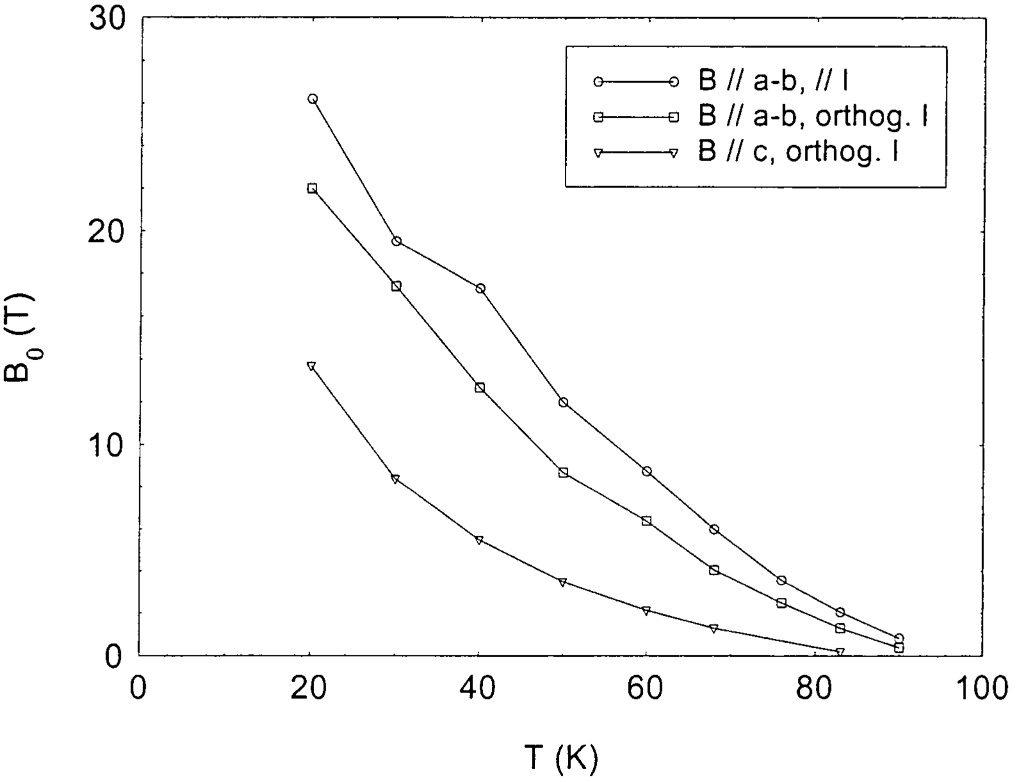

Figure 6.6. The parameter B_0 versus temperature from the flux creep model for the three orientations of the tape with respect to the magnetic field.

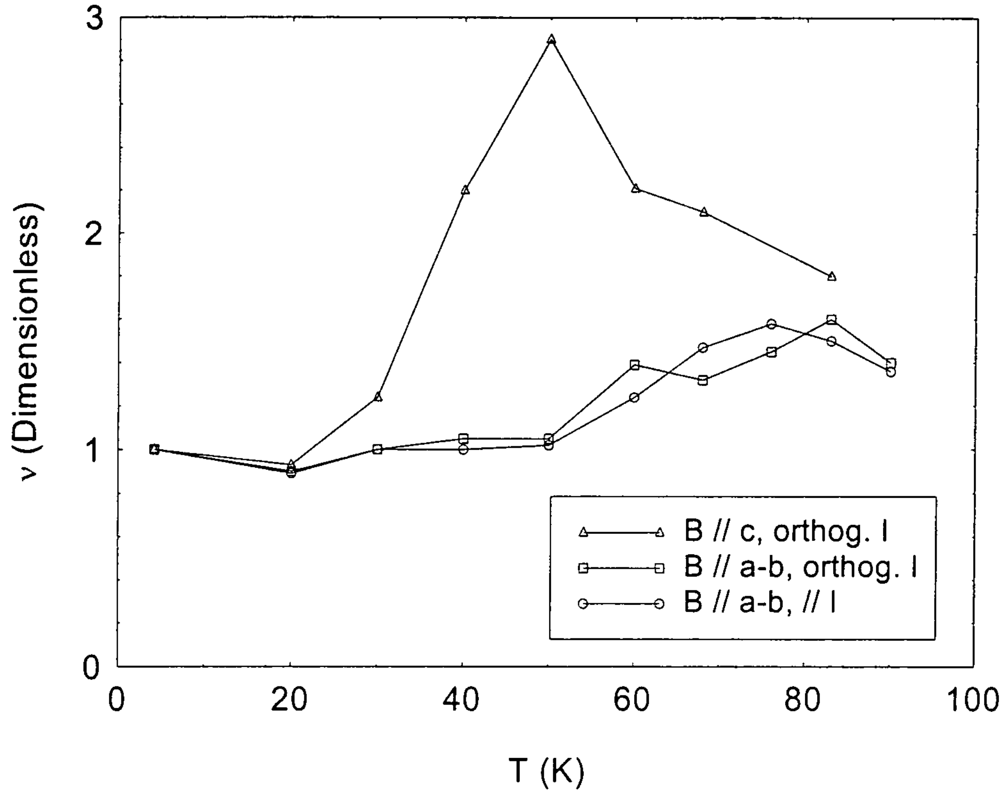

Figure 6.7. The dimensionless parameter υ versus temperature from the flux creep model for the three orientations of the tape with respect to the magnetic field.

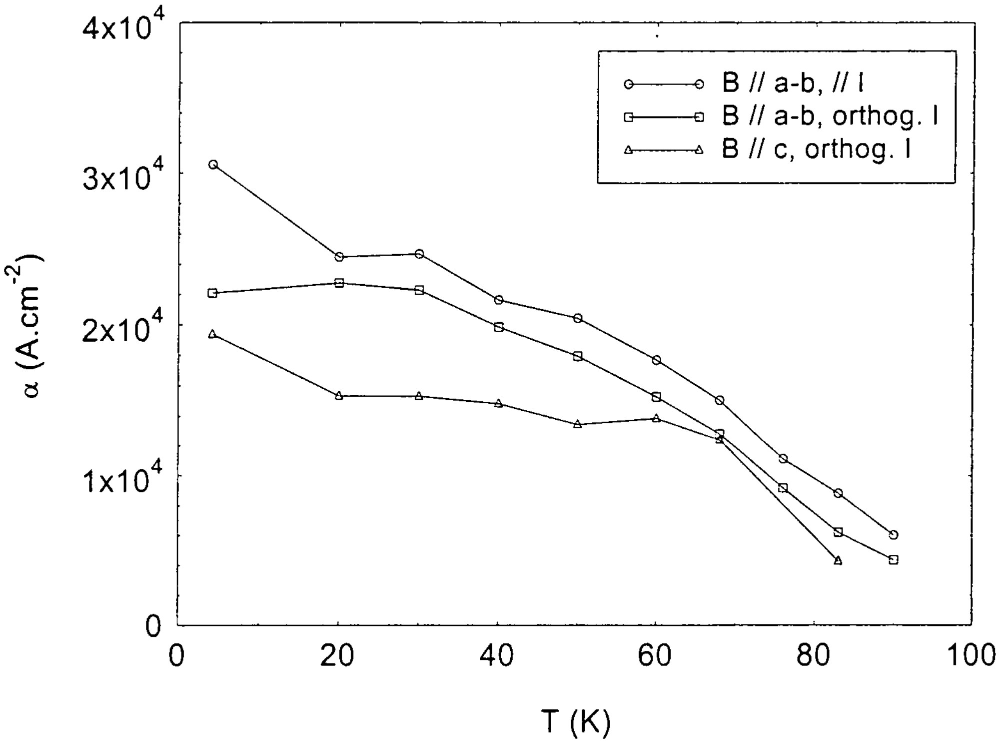

Figure 6.8. The parameter α versus temperature from the weak-link diffraction model for the three orientations of the tape with respect to the magnetic field.

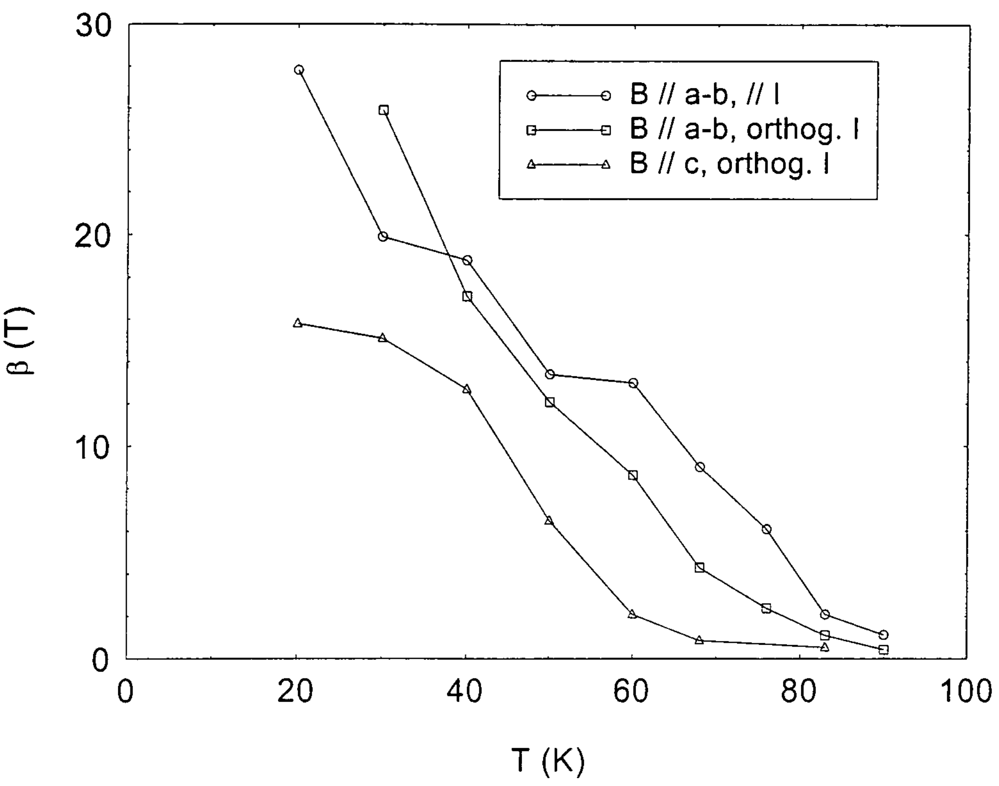

Figure 6.9. The parameter β versus temperature from the weak-link diffraction model for the three orientations of the tape with respect to the magnetic field.

The data have also been fitted using the Fietz-Webb flux pinning scaling law [16] which has been successful in many studies of low temperature superconductors [17]. No universal scaling was observed for these data and the quality of the fits was rather poor. This law has been disregarded in the rest of this work.

It is clear that although the fundamental mechanism for the FC and WL models are completely different, if υ is set to 1 and B_{C2} to infinity, the functional forms are both exponential in magnetic field with two identical free parameters. Since the magnetic field data at low fields for all three orientations is almost exponential one can expect the absolute values, orientation and temperature dependence of the parameters to be similar. Comparing J_0 and α, which represent the extrapolated value of J_c in zero field, these similarities are observed. Equally the values of B_0 and β have similar absolute values, orientation and temperature dependence. $\beta(T)$ decreases with increasing temperature for all orientations and shows positive curvature as previously observed in HTS[18] and Chevrel phase materials[19]. At low temperatures B_{c2} of the Bi-2223 tapes is much greater than the maximum measured field and there is no curvature in the exponential field dependence of $J_c(B)$ data up to 15 T. For this reason possible errors in B_{c2} are expected at 4.2 K for all orientations and at 20 K for the orientations with field applied parallel to the tape surface. In the FC model this feature fixes υ to the value 1. For these reasons the 4.2 K values of B_0 and $\beta(T)$ have been omitted from the relevant figures.

The most striking feature of the data presented is that despite the underlying mechanisms in the FC and WL models being completely different, they both agree equally well with the experimental data. Additional experimental and theoretical work is required to distinguish which of these models is correct.

6.3 The Curved Film Model

In this section, the assumptions and predictions of the "curved film" model are described. The curved film calculations represent the maximum obtainable J_c values in Bi-2223 tapes assuming that J_c properties equivalent to those achieved in the superb Bi-2223 film produced by Yamasaki et al are reproduced. The zero field J_c values have been extrapolated from published B // c orientated films [4]. Although J_c is higher in the a-b oriented thin film data the pinning mechanism in that particular orientation is unique since the fluxons are parallel to the a-b planes and consequently locked between the planes. The high pinning force associated with this orientation is not representative of any other angle of applied field. Since angles of applied field other than zero are included in the curved film model J_c values from the c-axis orientated thin film data are used. The Bi-2223 film has the highest values of J_c reported, is fully dense and "no apparent grain boundaries" [4]. The reported properties of the thin film are used to calculate the predicted properties of a curved film in which there is no degradation due to strain and there are no deleterious effects of percolation. The curved film represents an idealised tape where the amount of curvature represents the degree of grain alignment in the tape and in which there are no grain boundaries to act as barriers in high magnetic fields.

Thin film $J_c(B,T,\theta)$ data has shown that the angular dependence of J_c is dominated by the field component in the c-direction where [4]:

$$J_c(B,T,\theta) = \alpha^*(T)\exp\left(\frac{-B|\sin\theta|}{\beta^*(T)}\right) \tag{6.3}$$

where the temperature dependence of $\alpha^*(T)$ and $\beta^*(T)$ are known from the thin film data. In the calculations, we have added in a factor $(1-B/B_{C2})$ as in Eqn. 6.2 which ensures that J_c becomes zero at $B_{c2}(T)$. This additional factor is only important at the very highest fields. The $B_{c2}(0)$ values assumed are 1210 and 38 T for parallel and perpendicular to the a-b planes respectively and are taken from resistivity measurements on high quality Bi-2223 whiskers [20]. T_c is taken as 110 K. The angular dependence of B_{c2} in highly anisotropic superconductors can be described using the layered [21] or coupled models [22]. For highly anisotropic materials, both models predict a similar functional form. The coupled model was used in these calculations

$$B_{c2}(T,\theta) = \frac{B_{c2}(T)}{\left(\cos^2(\theta) + \gamma^2\sin^2(\theta)\right)} \tag{6.4}$$

where θ is the angle between the applied field and the a-b plane and $\gamma = B_{c2//ab}/B_{c2//c}$. The temperature dependence of B_{c2} was assumed to follow that of BCS theory [23] given by:

$$B_{c2}(T) = B_{c2}(0)\left(1 - \left(\frac{T}{T_c}\right)^2\right) \tag{6.5}$$

The temperature and angular dependence of $B_{c2}(T,\theta)$ for a high quality thin films is calculated by combining Eqns. 6.4 and 6.5 and the net $J_c(B,\theta,T)$ dependence for a flat film is given by

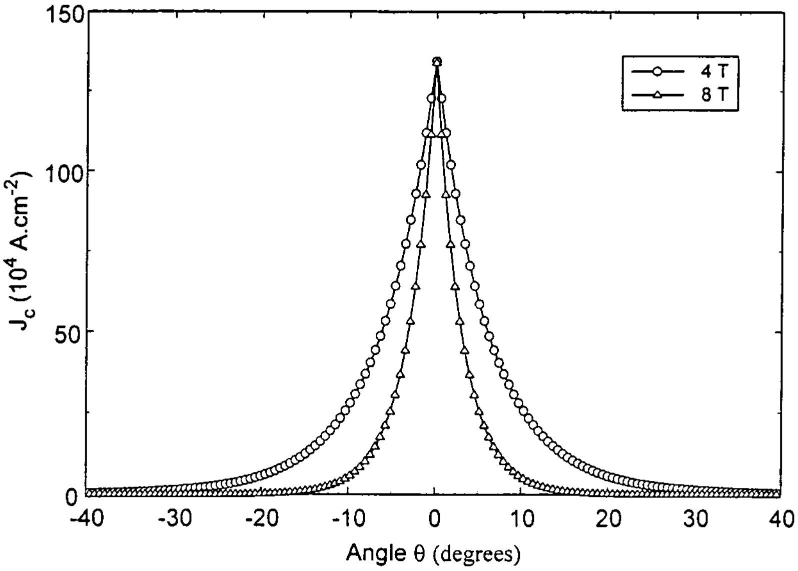

Figure 6.10. The calculated angular dependence of the critical current density of a Bi-2223 flat film at 40 K at 4 T and 8 T.

$$J_c(B,T,\theta)=\alpha(T)\left(1-\frac{B}{B_{c2}(T,\theta)}\right)\exp\left(-\frac{B|\sin(\theta)|}{\beta(T)}\right) \tag{6.6}$$

where θ is the angle between the applied field and the a-b plane of the flat film. In Fig. 6.10 the angular dependence of J_c is presented at 40 K at 4 and 8 T. The strong effect of the anisotropy is evident from the sharp decrease in J_c as θ increases from 0°. A sharper decrease is observed at higher fields due to the increased magnitude of the B // c component. These calculations are consistent with the experimental data from the film [4]. Predictions of the $J_c(B,T)$ dependence for a curved thin film can be generated by incorporating a curvature term into Eqn. 6.6 where:

$$Jc(B,\theta,T,\phi)=\frac{\int_{\delta-0.5\phi}^{\delta+0.5\phi}\alpha(T)\left(1-\frac{B}{B_{c2}(T,\theta)}\right)\exp\left(-\frac{B|\sin\theta|}{\beta(T)}\right)d\theta}{\phi} \tag{6.7}$$

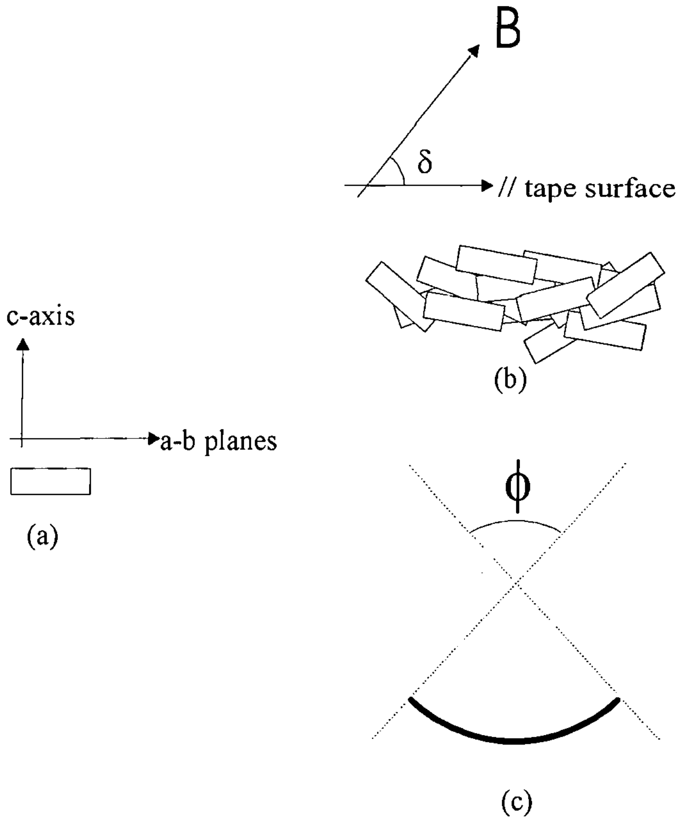

Figure 6.11. (a) The orientation of a Bi-2223 grain; (b) A schematic representation of grains within a superconducting tape aligned within the angle ϕ; (c) A curved film representing the tape in (b).

where δ is the angle between the applied field and the middle of the curved film, ϕ describes the degree of curvature so that the angle subtended by the curved film is ϕ and θ is the angle between any component in the curved film and the applied field. These parameters are shown in Fig. 6.11. The calculated J_c(B,T) dependencies at 20 and 60 K for varying degrees of grain alignment (various levels of ϕ) are presented in Figs. 6.12, 6.13 and 6.14. Calculations are shown for field applied parallel and perpendicular to the tape surface. Short sample data at the relevant temperature is included for comparison. As the degree of curvature increases, the anisotropy of J_c for the applied field in the two orthogonal directions decreases. For a completed curved thin film (i.e. a half-tube), $\phi = 180^{\circ}$ and the curved film exhibits an isotropic $J_c(B)$ dependence. Also note that at 20 T, the half-tube film has a J_c value more than an order of magnitude lower than a flat film when B is parallel to the a-b planes at 20 K and more than 2 orders of magnitude lower at 60 K.

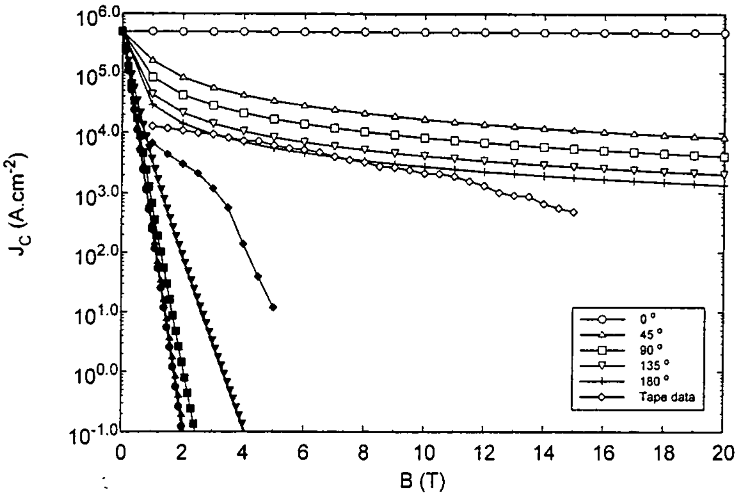

Figure 6.12: The field dependence of the critical current density calculated using the curved film model at 60 K. The angles denote the arc described by the thin film. Open and closed symbols indicate the field applied parallel and orthogonal to the tape surface respectively. Experimental critical current density values for the Bi-2223 tape at 60 K are shown for comparison.

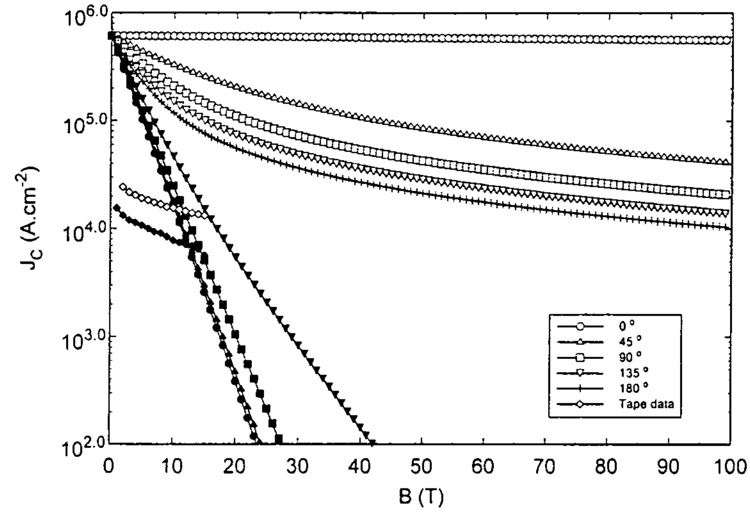

Figure 6.13. The field dependence of the critical current density calculated using the curved film model at 20 K in fields up to 100 T showing the effect of the upper critical field. The angles denote the arc described by the thin film. Open and closed symbols indicate the field applied parallel and orthogonal to the tape surface respectively. Experimental critical current density values for the Bi-2223 tape at 20 K are shown for comparison.

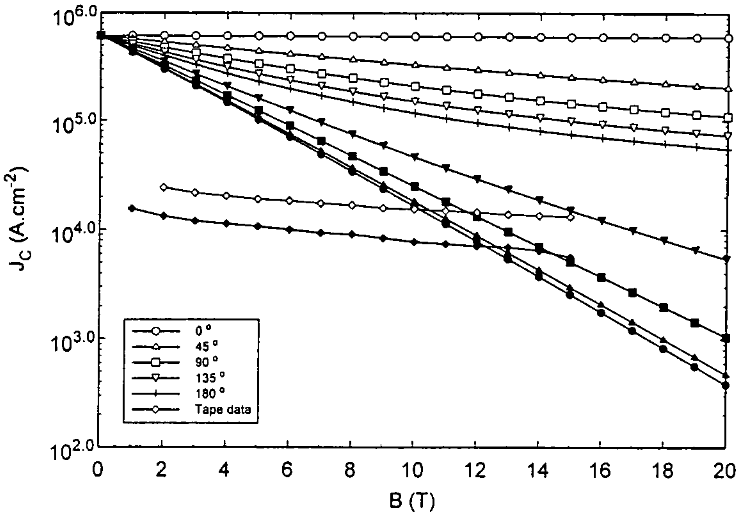

Figure 6.14. The field dependence of the critical current density calculated using the curved film model at 20 K in fields up to 20 T. The angles denote the arc described by the thin film. Open and closed symbols indicate the field applied parallel and orthogonal to the tape surface respectively. Experimental critical current density values for the Bi-2223 tape at 20 K are shown for comparison.

6.4 Discussion

The measurements presented in this chapter are among the most comprehensive presented in the literature however they are still unable to distinguish between some of the theoretical models which predict the factors limiting J_c. The errors associated with this measurement include temperature uncertainty of up to 3 K and errors in J_c due to the effects of the shunt. It is suggested that measurements on single filaments etched from the tape may be the most efficient way to distinguish the models. Higher accuracy in temperature control would clearly reduce the uncertainty on the measurement and accurate values of J_c could be attained without the contribution from the shunt. $B_{c2}(T)$ in these materials remains ill-defined however experiments controlling the current on the μA level close to B_{c2} could measure the parameter as a function of temperature therefore removing the free parameter from many of the fitting models. However, there are many difficulties associated with the single filament measurement including electrical contacts and sample preparation as discussed in Chapter 5.

The calculated J_c values provide an upper bound for J_c achievable in Bi-2223 assuming that the world's best Bi-2223 thin films are optimised samples. A comparison of the anisotropy in the $J_c(B,T)$ functional form of the measurements with the calculations at 20 and 60 K suggests that the angle of grain alignment within the tape measured is between 135 – 180°. The magnitude of Jc in the tapes at 20 K and 15 T with the field applied parallel to the a-b axis is 1.3 x 10^4 A.cm^{-2}. This value can be compared with predictions of 9.9 x 10^4 A.cm^{-2} in a curved film with ϕ = 135° in the same conditions and 6.05 x 10^5 A.cm^{-2} for a flat film. Therefore the tapes perform within a factor 8 of curved film (ideal tape) performance at 20 K assuming 135° grain alignment. At 60 K and 15 T the tape performance is 4.9 x 10^2 A.cm^{-2} compared with 2.7 x 10^3 curved film with ϕ = 135° and 4.9 x 10^5 A.cm^{-2} for a flat film. These data at 60 K suggest that at 5 T the tapes are already close to the optimum predicted from the film calculations.

The implications of these calculations are quite far-reaching. Although the J_c of these particular tapes are about a factor 3 below state of the art long length tapes at 77 K and zero field, at high field they operate to within a factor 8 of the curved film at 15 T assuming grain alignment of 135° and perfect grain boundaries. These numbers should be used to influence the direction of the effort put into increasing tape J_c. The calculations suggest that increasing the quality of the grain boundaries and grains can only possibly produce an increase in J_c of a factor 8 at 20 K at 15 T for a similarly aligned conductor.

Although improvements in grain alignment in the tapes (equivalent to a flatter thin film) would increase the value of J_c with field applied parallel to the surface of the tape, the associated increase in anisotropy of the $J_c(B)$ dependence would affect the suitability of the tape for use in applications. Magnet systems generate field components parallel and perpendicular to the central field. In a magnet, the operating current density is required to be below J_c for all turns. When using an anisotropic superconducting tape, the maximum axial field (B_{Amax}) and the maximum radial field component (B_{Rmax}) must both be considered in the choice of conductor. For a magnet designed to produce the maximum field with the minimum volume of turns the ratio of B_{Amax} to B_{Rmax} is around 4. The performance limiting point within the magnet is then determined by the anisotropy condition $J_{cB//ab}(B_{Amax})$ / $J_{cB//c}(B_{rmax})$ where typically B_{Amax} = 4 x B_{Amax}. If this ratio is equal to 1 then the performance of the magnet is determined by both orthogonal field components (this is the optimal operational condition), however for ratios other than 1 the performance of the magnet is limited by either the radial or axial field component. As the degree of alignment within the tape is increased the associated anisotropy in the $J_c(B)$ dependencies will also increase, as shown in Figs 6.12-6.14, resulting in the J_c ratio at the maximum axial and radial field components increasing above the value 1 (which is not optimum). Therefore increasing J_c for fields applied parallel to the surface of the tape through increased alignment beyond the anisotropy condition cited above, is not a route to increasing the field available from typical magnet systems.

6.5 Conclusions

The J_c(B,T) dependence of ideal Bi-2223 tapes has been calculated assuming that the polycrystalline tape can be described by a curved film model. These calculations account for the degree of grain alignment in the tapes and assume that the properties of the best reported thin film are at an optimum. A comparison between the calculations and measurements suggest that the maximum obtainable J_c in high magnetic fields at 20 K, useful for applications, is only a factor 8 above that presently available from industrially manufactured tapes. Although perfectly aligned tapes produce the highest J_c with field aligned to the a-b planes the large anisotropy associated with the alignment means that these tapes are not the most useful for typical applications.

References for Chapter 6

[1] Horvat J, Dou S, Lui H, and Bhasale R 1996 *Physica C* **271** 51-58

[2] Li Q, Brodersen K, Hjuler H, and Freltoft T 1993 *Physica C* **217** 360-366

[3] Malozemoff A, Carter W, Fleshler S, Fritzemeier L, Li Q, Masur L, Miles P, Parker D, Parrella R, Podtburg E, Riley G, Rupich M, Scudiere J, and Zhang W 1999 *IEEE Transactions on Applied Superconductivity* **9** 2469-2474

[4] Yamasaki H, Endo K, Kosaka S, Umeda M, Misawa S, Yoshida S, and Kajimura K 1993 *IEEE Transactions on Applied Superconductivity* **3** 1536-1539

[5] Larbalestier D and Lee P 1999 *Proceedings of the 1999 Particle Accelerator Conference* 177-181

[6] Dimos D, Chaudhari P, Mannhart J, and LeGoues F 1988 *Phys. Rev. Lett.* **61** 219-222

[7] Dimos D, Chaudhari P, and Mannhart J 1990 *Physical Review B* **41** 4038-4049

[8] Shibutani K, Li Q, Sabatini R, Suenga M, Motowidlo L, and Haldar P 1993 *Applied Physics Letters* **63** 3515-3517

[9] Kawasaki M, Sarnelli E, Chaudhari P, Gupta A, Kussmaul A, Lacey J, and Lee W 1993 *Applied Physics Letters* **62** 417-419

[10] Feigel'man M and Vinokur V 1990 *Physical Review B* **41** 8986-8990

[11] Hampshire D 1997 *Physica C* **296** 153-166

[12] Keys S and Hampshire D, in *Handbook of Applied Superconductivity* (IOP Publishing Ltd., London, to be published).

[13] Ekin J 1989 *Applied Physics Letters* **55** 905-906

[14] Huang Y, ten Haken B, and ten Kate H 1999 *IEEE Transactions on Applied Superconductivity* **9** 2702-2705

[15] Hsiang T and Finnemore D 1980 *Physical Review B* **22** 154-163

[16] Fietz W and Webb W 1969 *Physical Review* **178** 657-667

[17] Dew-Hughes D 1974 *Philosophical Magazine* **30** 293-305

[18] Le Lay L, Friend C, Maruyama T, Osamura K, and Hampshire D 1994 *Journal of Physics Condensed Matter* **6** 10053-10066

[19] Zheng D, Ali S, Hamid H, Eastell C, Goringe M, and Hampshire D 1997 *Physica C* **291** 49-58

[20] Matsubara I, Tanigawa H, Ogura T, Yamishita H, Kinoshita M, and Kawai T 1992 *Physical Review B* **45** 7414-7417

[21] Tinkham M 1963 *Physical Review* **129** 2413-2422

[22] Lawrence W and Doniach S 1970 *Proceedings of the 12th International Conference on Low Temperature Physics, Kyoto, Japan* 361-362

[23] Bardeen J, Cooper L, and Schrieffer J 1957 *Physical Review* **108** 1175-1204

Chapter 7

Introduction to Superconducting Magnet Design

7.1 Introduction

After the discovery of the superconducting alloys in the 1950s and 60s it became clear that superconducting magnets would offer superior performance to their conventional counterparts. The potential for compact high field systems with low power consumption could be realised through the high current densities of the materials and zero resistance operating mode. Persistent current operation would also produce stable fields over long time periods. The design of superconducting magnets is a specialist science with systems being designed to the specific requirements of the user. Types of system range from small solenoids to large volume 3-D magnets used in fusion projects. Specific design parameters include magnitude and direction of field, bore size, operating temperature, field homogeneity and field stability.

The most important part of any magnet is the wire or tape used for winding. Most superconducting magnets are presently produced using NbTi and Nb_3Sn wires although HTS magnet technology is rapidly emerging. Other A15 and Chevrel phase materials offer realistic alternatives for the future. Magnetic fields just above 20 T at 4.2 K can be produced using combinations of NbTi and Nb_3Sn where higher fields are unobtainable due to the B_{c2} values of the materials. A cryocooled NbTi/Nb_3Sn laboratory system with a 52 mm room temperature bore has recently been reported producing a bore field of 15 T[1]. The high B_{c2} and T_c values of the HTS give the potential for high field cryocooled magnet systems operating at 20 or 30 K or for use as magnet inserts within low temperature high field systems. Cryocooled Bi-2223 systems with room temperature bores have produced fields in excess of 7 T[2,3] and a HTS insert has produced 1.46 T within a 22.54 T background field at 4.2 K[4]. Hybrid systems containing high powered water cooled magnets within superconducting outer coils have been designed to produce DC magnetic fields in excess of 40 T [5,6]. Non-destructive pulsed field systems currently produce fields above 60 T [7] for time periods up to 100 ms [8] and a project is underway to produce the first non-destructive 100 T pulse field magnet [9]. Explosive pulsed field systems are capable of producing fields as high as 1000 T.

In this chapter the main considerations of superconducting magnet design are discussed focusing around the basic solenoid. Firstly the equations used to calculate the field generated within the coil are presented. Limitations of the field magnitude for a magnet system are presented in a discussion of the critical current dependence of field, temperature and strain of the conductor. The transition from superconducting to normal state (quenching) in a superconducting magnet is potentially destructive to the system. The causes of quenching are discussed in Section 7.4 and the main protection mechanisms against damage are presented. Large field homogeneity is essential for many superconducting magnet applications and the methods used to increase field homogeneity are identified in Section 7.5. After a discussion of magnet impregnation and 'training' the main applications of superconducting magnets away from the physics research laboratory are briefly described.

7.2 Magnetic field calculations

7.2.1 Field calculation at a point (*r*,*z*) due to a magnet

The axial and radial field components at any position (*r*,*z*) with respect to the centre of an elemental current loop of radius *a* carrying current *I* can be calculated using the expressions[10]

$$B_z(z,r) = \frac{2I}{10a}\left[\frac{1}{\left[(1+r/a)^2+(z/a)^2\right]^{1/2}}\right]\left\{K(\phi)+\frac{1-(r/a)^2-(z/a)^2}{\left[1-(r/a)\right]^2+(z/a)^2}E(\phi)\right\} \quad \textbf{(7.1)}$$

$$B_r(z,r) = \frac{2I}{10a}\left(\frac{z}{r}\right)\left[\frac{1}{\left[1-(r/a)^2+(z/a)^2\right]^{1/2}}\right]\left\{-K(\phi)+\frac{1+(r/a)^2+(z/a)^2}{\left[1-(r/a)\right]^2+(z/a)^2}E(\phi)\right\} \quad \textbf{(7.2)}$$

where

$$\phi = \sin^{-1} k \tag{7.3}$$

and

$$k = \left[\frac{4(r/a)}{(1-r/a)^2 + (z/a)^2}\right]^{1/2} = \sin\phi . \tag{7.4}$$

$K(\phi)$ and $E(\phi)$ are complete elliptic integrals of the first and second kind respectively. The field produced at any point due a magnet can be calculated by integration of Equations 7.1 and 7.2 within the particular system.

7.2.2 Field produced at the central point of a solenoid

The simplest of magnet types is the solenoid. In the following descriptions the solenoid length is given by $2l$, bore radius a, outer winding radius b, number of turns N and the field at the central point B_0 as shown in Figure 7.1. The magnet is assumed to be completely homogenous and the average current density of the magnet, J_{coil}, is given by

$$J_{coil} = \frac{NI}{2l(b-a)} \tag{7.5}$$

where I is the current through the magnet.

The field at the centre point of the solenoid is given by

$$B_0 = J_{coil} a F(\alpha\beta) \tag{7.6}$$

where $F(\alpha\beta)$ is the shape factor described by[11]

$$F(\alpha\beta) = \mu_0 \beta \ln\left(\frac{\alpha + (\alpha^2 + \beta^2)^{1/2}}{1 + (1 + \beta^2)^{1/2}}\right), \tag{7.7}$$

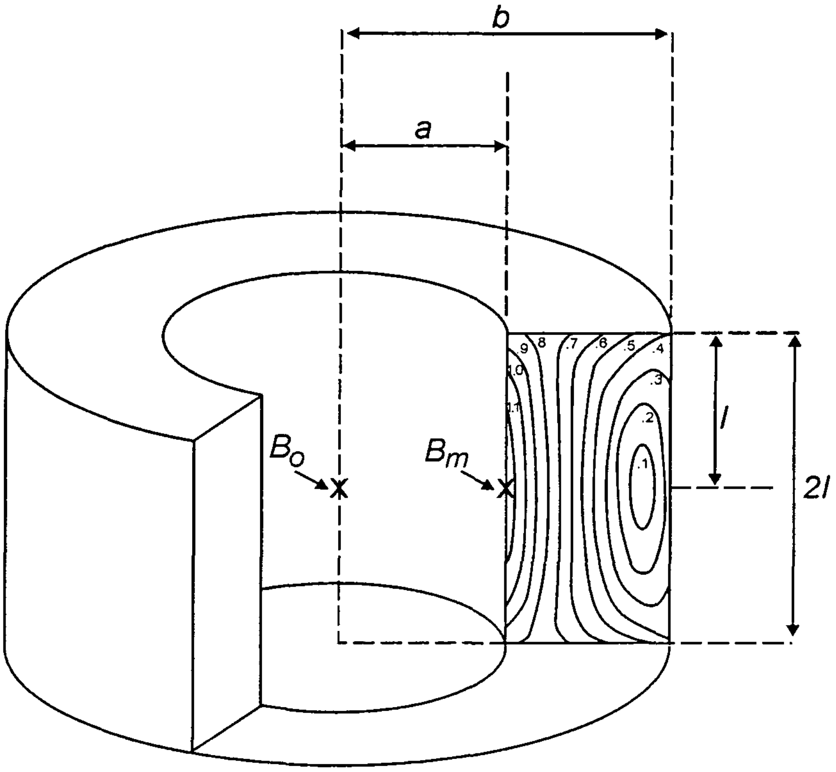

Figure 7.1. A schematic of a simple solenoid showing field line contours within the cross-section. The magnitude of field on each contour is given relative to the central field.

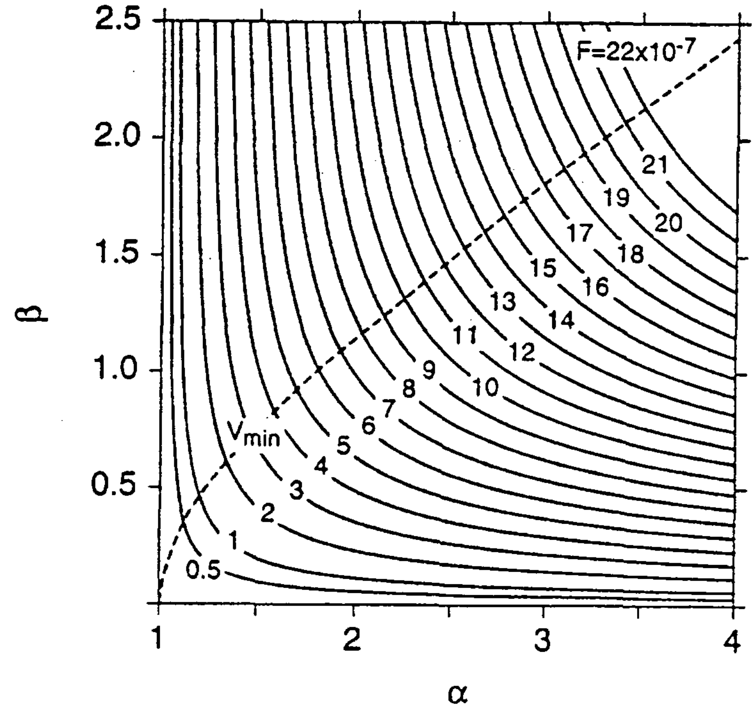

Figure 7.2 Function F, relating the central field in a simple solenoid to its radius, current density and shape factors α and β[12].

$\alpha = b/a$ and $\beta = l/a$. In Figure 7.2 the shape function is presented as a function of α and β. Clearly different values of α and β can be used to produce to the same central field. The minimum volume required to produce a given central field is described by the function

$$V_{\min} = 2\pi a^3(\alpha^2 - 1)\beta. \tag{7.8}$$

The minimum volume dimensions produce a short fat magnet with low field homogeneity and a high ratio between the maximum field within the magnet and the central field. The maximum field within a solenoid occurs on the inner winding at the midpoint along the length, represented by point B_m in Figure 7.1. For a superconductor the current carrying capacity is dependent on field and hence it is more efficient to subject the conductor to a field similar to the central field of the magnet. For these reasons the minimum volume dimensions may not always be the most efficient in magnet design.

7.3. Limiting factors in the performance of superconducting magnets

The dominating factor in the design of a magnet system is the performance of the electrical conductor. Superconducting materials are only useful below the critical current density in specific background conditions. The critical current density of superconductors has been observed to be dependent on the magnitude and direction of applied field, temperature [4,13,14] and strain [15-17]. As shown in Figure 7.1 different turns within a magnet experience fields varying in both magnitude and direction. The bending strain experienced by different turns also varies due to the variation in radii of current loops. Therefore the dependence of J_c on field, temperature and strain should be known explicitly for the conductor within the ranges experienced within the magnet in order to make reliable predictions of expected performance.

The performance of the conductor at a particular point within the magnet can be predicted using load lines. A load line defines the magnitude and direction of field at a specific point within the magnet as a function of current through the magnet. The intercept of the load line with the field dependence of the critical current for the conductor in identical conditions defines I_c for a turn at the corresponding position. If all sections of the magnet are connected in series the performance will be limited by the turn with the lowest I_c.

The performance of a magnet can be optimised using a technique known as grading. The magnet cross-section should be divided into regions experiencing similar field magnitudes, field directions or bending strains. A conductor with optimum current carrying properties within the conditions of a section can then be selected and used to wind that particular section of the magnet. For example, Bi-2223 has been shown to have a strong J_c dependence on angle of applied field and bending strain above about 0.3 %. Therefore regions of a Bi-2223 magnet experiencing field perpendicular to the tape surface or a bending strain above 0.3 % may be replaced by a conductor with higher J_c values in the same conditions. However, if the magnet is designed to operate in liquid nitrogen clearly only HTS materials are suitable. It is clear that there are many considerations when designing a magnet system and the conductor should always be carefully chosen in order that the performance is optimised.

7.4 Quench production and protection

7.4.1 Introduction to quenches and quench protection

Quenching is the term used to describe the process that occurs when any part of a superconducting magnet changes from the superconducting to normal phase. A transition will occur when any of the critical parameters of the superconducting material are exceeded. At low temperatures the specific heat of all materials is relatively low and therefore a very small increase in energy will produce a large increase in temperature. The low operating temperature of superconducting magnets means that the release of only a small amount of energy within the magnet may initiate a quench in the system.

The energy stored in a magnet is given by

$$E = \frac{1}{2} L I^2 \tag{7.9}$$

where L is the inductance of the magnet and I is the current. Typical superconducting magnets may store up to megajoules of energy which can be released in a few tenths of a second during a quench. As a comparison, 1 MJ is the energy required to boil off 333 l of liquid helium. If the energy was released uniformly within the magnet there would seldom be a problem however a quench is normally initiated at a single point. The energy is released in the form of heat and spreads from the initiating point by ohmic heating and thermal conduction. The initiating point experiences the highest temperatures simply because it is subjected to heating for the longest time. The increase in temperature during a quench may be sufficient to burn through the insulation or even melt the wire.

All magnet systems have a 'minimum propagating zone'. If the heat produced at the initiation point is below the minimum propagating value then the cooling properties of the magnet are sufficient to disperse the heat and prevent the propagation of the quench. However, the quench will spread throughout the magnet if the heat exceeds the minimum propagating value. Even in the best designed magnet systems there is always the possibility of liquid helium being lost or the current being ramped too high and so magnets must be designed to quench safely at all times. Ideally the magnet would be able to absorb the energy released during a quench without any damage to the system. However the high levels of energy stored during operation in most systems demand that protection devices are an integral part of any superconducting magnet. In this section the main causes of quenching are identified and the most frequently employed magnet protection mechanisms are discussed.

7.4.2 Typical causes of quenches

7.4.2.1 Eddy current heating

Within a magnet, ramping the current results in eddy currents being produced in the matrix of the superconducting wire and in the support structure. At higher ramp rates larger currents are produced. If the heat produced in these non-superconducting materials cannot be conducted away from the superconductor at a fast enough rate, the superconductor will increase in temperature and initiate a quench.

7.4.2.2 Movement within a magnet

Cooling and operating magnet systems results in large stresses being exerted on the system which may result in movement of the turns. Forces on the wire are induced by Lorentz forces and differential thermal contraction between different materials. Movement of wire of only few microns during operation may release enough frictional energy to produce a normal region in the magnet and initiate a quench. Therefore superconducting magnets must be designed to prevent any movement of wire during operation.

The conductor can experience very large Lorentz forces during operation due to the high currents and fields experienced by the turns. In some magnet systems the local forces can approach the yielding strength of copper. In designing a magnet the forces acting within the system should be accurately modelled and the magnet sufficiently strengthened to prevent any movement of wires. Within a standard solenoid the forces act to compress the coil axially and burst the coil radially. Coils are impregnated using wax or resin to prevent movement of the turns during operation. A discussion of coil impregnation is presented in Section 7.6.

The second cause of stresses within the magnet is the differential thermal contraction of the constituent materials. On cooling from room temperature to cryogenic temperatures all materials experience some degree of thermal contraction.

Forces induced between sections of the magnet may be considerable due to differential thermal contraction between materials.

7.4.2.3 Flux jumping

Using the critical state model, on applying a magnetic field to a slab of superconductor a screening current is induced around the surface. The current density of the screening current is J_c. Therefore the current density within the slab has only two possible values, J_c or zero. If the external field is kept constant, on increasing the temperature of the slab the current density of the material is reduced and the magnetic field will penetrate deeper into the slab. The resulting movement of flux will generate heat and increase the temperature further. If the original disturbance is strong enough it will cause an avalanche of heat generation and flux motion – a flux jump. By dividing the wire into fine subsections the energy dissipation is reduced and the surface of the superconductor is increased thereby reducing the effects of flux jumping. Flux jumping may be observed during the ramping of a magnet system. Typically a random, backward step in field of a few mT would be observed, generally at fields below 2 T.

7.4.3 Methods of protection against quenching

7.4.3.1 Protection by an external resistor

The simplest protection for a superconducting magnet is an external 'dump' resistor. The electrical circuit is shown in Figure 7.3(a) containing a switch (S) and external resistor (R_e). The switch is opened on detection of a quench and the current decays through the external resistor. The external resistor dominates the decay time if it is chosen to have a large resistance compared with the internal quench resistance (R_q). The current decay time is given by

$$\tau = L\left(R_e + R_q\right)^{-1} \qquad \textbf{(7.10)}$$

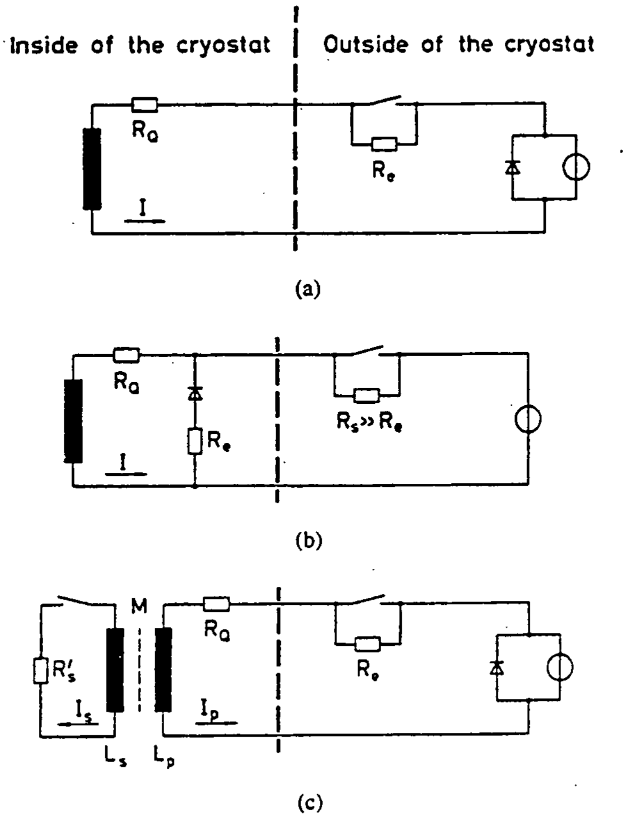

Figure 7.3. Magnet protection circuits using; (a) an external resistor; (b) an internal diode plus external resistor; (c) magnetically coupled resistor [18].

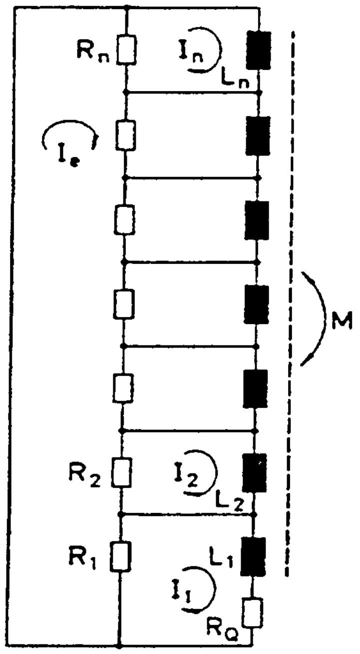

Figure 7.4. Quench protection of a subdivided coil with *n* subdivisions [18].

where L is the induction of the magnet. An advantage of the external resistor is that most of the energy is removed from the cryogenic environment minimising cryogen boil off. The external resistor circuit is an 'active' protection mechanism relying on a detection circuit to operate the switch.

An extra diode may also be added to the circuit as shown in Figure 7.3(b). In the figure the diode is contained within the cryostat and referred to as a 'cold diode'. In the case of a quench and after the current source has been switched to zero the current will pass through the diode.

7.4.3.2 Protection by a coupled secondary coil

By magnetically coupling the magnet to a short-circuited secondary coil any change in current in the magnet will couple to the secondary. This circuit is shown in Figure 7.3(c). The secondary is often the support cylinder of the magnet or another part of the support structure. During a quench part of the energy will be transferred from the magnet into the secondary reducing the temperature and voltage across the normal region. If the secondary is in good thermal contact with the magnet the heat produced in the secondary will heat up the magnet thus increasing the rate of propagation of the normal conducting region. This technique is called 'quench-back'. A disadvantage of the coupled protection technique is that during current ramping energy will be released from the secondary within the cryostat possibly warming the magnet. For this reason a low ramp rate is always used in magnets protected in this way.

7.4.3.3 Protection by subdivision

A final method of protection for the magnet is the use of subdivisions as shown in Figure 7.4. In this protection technique shunt resistors are placed in parallel with sections of the superconducting coil. During superconducting operation the current passes through the magnet but when the resistance of a superconducting section increases the current is shared between the coil and the shunt resistor. The disadvantage of the subdivision protection mechanism is that heat is released across the resistors during ramping causing cryogen boil off and therefore a slow ramp rate is required.

7.4.3.4 Summary of quench protection

It is clear that in an ideal case a magnet would be self protecting such that the heat released during a quench would disperse within the magnet and cause no damage. However this is only the case with small, low field magnet systems and in general protection mechanisms must be installed to control the quench safely. The two choices for protection are 'active' and 'passive' mechanisms. The active external resistor removes most of the energy from the cryostat and therefore avoids boiling off expensive cryogenic liquid. However the success of the system relies upon the quench detection system to open the switch. Passive systems are generally cheaper, simpler and more reliable. However energy is released through the protection circuits during current ramping and heavy restrictions are put on the magnet ramp rate. Also the stored energy is contained within the cryostat during the quench. Protection by subdivision is generally favoured among the passive protection techniques since it does not affect the coil construction and is usually more efficient if a sufficiently large number of sections are employed.

7.5 Homogeneity within a magnet system

The homogeneity of a magnet system is generally classified by defining a volume over which the uniformity of the magnetic field is specified. Homogeneity requirements vary between applications. For example, laboratory magnets are typically uniform to between 1 part in 1000 (10^{-3}) and 10^{-5} over 10 mm diameter spherical volume (10 mm DSV). MRI magnets are around 10^{-6} over 500 mm DSV and magnetic resonance spectroscopy requires approximately 2 x 10^{-10} over 7.2 mm DSV.

The field around the centre point of a uniform current density coil can be expressed as a series expansion. Along the *z*-axis the field has the form

$$B = B_0\left[1 + E_2(\alpha,\beta)\left(\frac{z}{a}\right)^2 + E_4(\alpha,\beta)\left(\frac{z}{a}\right)^4 + \ldots..\right] \qquad \textbf{(7.11)}$$

where a is the inner radius of the solenoid. For a simple solenoid the coefficient $E_2(\alpha,\beta)$ is negative and therefore the field decreases in moving away from the centre along the z-axis. Since the solenoid is symmetrical about the z-axis the odd terms in the expansion are equal to zero. The field homogeneity about the centre of the magnet can be increased by eliminating the power terms in the expansion. The order of a coil is defined by the lowest power of the (z/a) term.

The simplest way to improve field homogeneity is to increase the length of the solenoid and therefore increase the value of β. For further improvements, 'notches' are incorporated into the winding. A notch is a region of the magnet with low current density. Typical notches have current density equal to half or zero times the bulk of the windings. A zero current density notch would usually be occupied either by the magnet bobbin or air. Half current density notches are often wound from the superconducting tape with a 'dummy' tape in parallel carrying zero current thus halving the current density in the region of the notch. A notch increases field homogeneity about the centre of the magnet but decreases the magnitude of the field produced. Notches can be used to increase the order of the magnet up to sixth order in which the axial field distribution is given by

$$B = B_0\left[1 + E_6(\alpha,\beta)\left(\frac{z}{a}\right)^6 + E_8(\alpha,\beta)\left(\frac{z}{a}\right)^8 + \ldots..\right]. \qquad \textbf{(7.12)}$$

A higher level of field uniformity is gained through the use of series correction coils. Once the magnet has been fabricated there may be small variations in field homogeneity due to manufacturing tolerances. The homogeneity along the z-axis may typically diverge between 10 and 100 parts per million from the sixth order field function. It is possible that odd-order gradients ($(z/a)^3$ etc) may also appear in the expression for axial field distribution. To compensate these variations in field homogeneity series correction coils are wound around the outside of the main coil and connected in series with the main coil. The improved homogeneity is usually independent of field and therefore the coils will not need to be adjusted at different fields.

Shim coils are used to produce homogeneity greater than 1 part in 10^4 over 10 mm DSV. Superconducting shims can operate in series up to 1 part in 10^5 over 10 mm DSV or independently to above 1 part in 10^6 over 10 mm DSV. Shimming coils are situated outside the main coil and may be wound in any configuration to reduce field gradients on and off the *z*-axis. Magnet shimming is extremely complex and unique configurations are required for every magnet. High-resolution NMR magnets are usually fitted with atleast ten shimming coils each with its own superconducting switch.

7.6 Impregnation

Magnets are impregnated to prevent any movement of the windings during operation. The impregnant should fill all voids within the magnet volume thus supporting all regions of the magnet. An impregnant should be selected with similar thermal contracting properties to the other constituent materials in the magnet and good adhesive properties to the wire and insulation. Typical choices for the impregnant are paraffin wax or resin, depending on the application. All voids and gas bubbles must be removed before curing and so magnets are generally degassed before impregnation and impregnated under vacuum. Large volumes of impregnant are always susceptible to cracking. To avoid impregnant-rich areas the coil should be tightly wound and the volume of impregnant should not exceed the required minimum. The precise details of impregnating coils using wax and resin are presented in Chapters 8 and 9.

Wax is used to impregnate coils that exert low stresses on the conductor. The wax has no significant strength and is basically used to fill out the turns and prevent movement. Wax is regularly used to impregnate NMR magnets that experience low levels of stress and do not undergo many thermal cycles before being held at a constant field for a significant time. Wax impregnation is rather cheap and simple with the wax being heated above the melting point (around 60^0C) and penetrating between the turns.

Resin has a much greater strength than wax and is used to impregnate coils experiencing high levels of stress. Resin systems contain epoxy, hardener and accelerator mixed in precise ratios. Accurate temperature control during curing is also required to optimise the properties. Although resin is much stronger than wax it is more liable to crack during cooling or magnet operation. This cracking of the resin results in 'training' of the magnet.

7.7 Training

Newly built magnets are often found to quench prematurely (train) when they are initially energised. The resin is brittle at low temperatures and weak links will often crack when experiencing the stresses exerted within the magnet for the first time. The resin at a particular point can only crack once and on re-energising the magnet again another region of the coil may reach a critical stress limit and crack. Once the cracking process is completed, the magnet is 'trained' and able to reach higher currents before quenching. A well designed magnet should reach the design value without extensive training. Some modern resins can resist cracking and are used to impregnate magnets exhibiting little or no training.

7.8 Applications of superconducting magnets

7.8.1 Nuclear magnetic resonance (NMR)

7.8.1.1 Principles of NMR

The magnetic moment of a nucleus is given by

$$\mu = \gamma \hbar I \qquad \textbf{(7.13)}$$

where γ is the gyromagnetic ratio, $\hbar = h/2\pi$ (h is Plank's constant) and $\boldsymbol{I}$ is the spin. In an external field the magnetic moments attempt to align with the field but at a finite temperature thermal fluctuations result in misalignment the moments with the field direction. The moments precess around the field ($\boldsymbol{B_0}$) due to their angular momentum at a frequency given by

$$\omega = \gamma \boldsymbol{B}_0 . \tag{7.14}$$

The electrons of a molecule screen the magnetic field at the location of the nucleus. Therefore the local field is dependent on the chemical environment and the local precessing frequency changes accordingly. By exciting molecules at different radio frequencies in a background field and detecting the signals from the sample the nuclear magnetic resonance spectrum can be determined. NMR is a technique currently used in biochemical and medical applications.

7.8.1.2 Nuclear magnetic resonance spectroscopy

The first large scale application for superconducting magnets outside of physics came in the early 1970s in nuclear magnetic resonance (NMR) spectroscopy. High resolution NMR magnets are used in biochemistry for the structural analysis of molecules. Very large magnetic fields are required with long term stability better than 10^{-8} h^{-1} and a field homogeneity around 2 x 10^{-10} over 7.5 mm DSV. Large fields are required for added sensitivity and large field homogeneity produces a sharp resonance of extremely narrow linewidths. NMR magnets operate at a single field and remain at that field for a number of years. The field is usually expressed in terms of the proton frequency where 42 MHz corresponds to 1 T. Field strengths in NMR magnets currently range from 4.7 T (200 MHz) to 21.1 T (900 MHz) although 1 GHz NMR systems are presently being developed[19-22].

7.8.1.3 Magnetic resonance imaging (MRI)

Imaging using magnetic resonance techniques (MRI) has become a widely used medical procedure over the last decade. For clinical MRI only the proton is imaged.

The most important factors for MRI purposes are strong fields within large diameter bores exhibiting high homogeneity and excellent stability. Limiting stray fields is also an important design consideration and fields are shielded using a second coil around the outside of the main coil. Typical MRI magnets have a bore diameter of 1 m and produce a field of around 1.5 T of homogeneity 1 x 10^{-6} over 500 mm DSV stable to 1 x 10^{-7} h^{-1}.

7.8.2 Superconducting magnets used for thermonuclear fusion

Confinement of very hot deuterium-tritium plasma using magnetic fields is thought to be best way to control thermonuclear fusion. Superconducting magnets are now an integral part of any reactor due to the relatively low power required compared with conventional magnets.

7.9 Summary

The design of a superconducting magnet is a complicated science. The performance of the magnet is affected by the constituent conductor, the self-field generated within the turns and the choice of materials used for magnet fabrication. The causes and potential consequences of a quench have been discussed and the most common forms of protection against damage to the magnet have been identified. A discussion of the methods used to increase the field homogeneity within the bore have also been presented. The principles and considerations presented in this chapter have been used in the design and fabrication of a first generation 98 mm bore Bi-2223 magnet and a state of the art 1.29 T Bi-2223 laboratory scale magnet presented in Chapters 8 and 9 respectively.

References for Chapter 7

[1] Sakuraba J, Mikami Y, Watazawa K, Watanabe K, and Awaji S 2000 *Superconductor Science and Technology* **13** 12-17

[2] Snitchler G, Kaksi S, Manlief M, Schwall R, Sid-Yekhlef A, Ige S, Medeiros R, Francavilla T, and Gubser D 1999 *IEEE Transactions on Applied Superconductivity* **9** 553-558

[3] Sato K, Kato T, Ohkura K, Kobayashi S, Fujino K, Ohmatsu K, and Hayashi K 2000 *Superconductor Science and Technology* **13** 18-22

[4] Ohkura K, Sato K, Ueyama M, Fujikami J, and Iwasa Y 1995 *Applied Physics Letters* **67** 1923-1925

[5] Inoue K, Kiyoshi T, Kosuge M, Itoh K, Takeuchi T, Maeda H, Hanai S, Tezuka M, Kojo T, Murase S, Dozono Y, and Matsutani K 1996 *Physica B* **216** 181-185

[6] Bird M, Bole S, Eyassa Y, Gao B, and Schneider-Muntau H 2000 *IEEE Transactions on Applied Superconductivity* **10** 439-442

[7] Jones H, Van Cleemput M, Hickman A, Ryan D, and Saleh P 1998 *Physica B* **246-247** 337-340

[8] Schillig J, Boenig H, Gordon M, Mielke C, Rickel D, Sims J, Martin J, and Williams R 2000 *IEEE Transactions on Applied Superconductivity* **10** 526-529

[9] Sims J, Baca A, Boebinger G, Boenig H, Coe H, Kihara K, Manzo M, Mielke C, Schillig J, Eyssa Y, Lesch B, Li L, and Schneider-Muntau H 2000 *IEEE Transactions on Applied Superconductivity* **10** 510-513

[10] Montgomery D, *Solenoid Magnet Design* (John Wiley and Sons, Inc., 1969).

[11] Wilson M, *Superconducting Magnets* (Oxford University Press Inc., New York, 1998).

[12] Zerobin F and Seeber B, in *Handbook of Applied Superconductivity*; *Vol. 1*, edited by S. Seeber (IOP Publishing Ltd., London, 1998), p. 491-512.

[13] Sneary A, Friend C, Vallier J, and Hampshire D 1999 *IEEE Transactions on Applied Superconductivity* **9** 2585-2588

[14] Sato K, Hikata T, and Iwasa Y 1990 *Applied Physics Letters* **57** 1928-1929

[15] Ekin J, Finnemore D, Li. Q, Tenbrink J, and Carter W 1992 *Applied Physics Letters* **61** 858-860

[16] Ekin J 1980 *Cryogenics* **20** 611-624

[17] Cheggour N and Hampshire D 1999 *Journal of Applied Physics* **86** 552-555

[18] Meb K, in *Handbook of Applied Superconductivity*; *Vol. 1*, edited by B. Seeber (IOP Publishing Ltd., London, 1998), p. 527-555.

[19] Markiewicz W, Bonney L, Dixon I, Eyssa Y, Swenson C, and Schneider-Muntau H 1996 *Physica B* **216** 200-202

[20] Kiyoshi T, Sato A, Wada H, Hayashi S, Shimada M, and Kawate Y 1999 *IEEE Transactions on Applied Superconductivity* **9** 559-562

[21] Markiewicz W, Dixon I, Swenson C, Marshall W, Painter T, Bole S, Cosmus T, Parizh M, King M, and Ciancetta G 2000 *IEEE Transactions on Applied Superconductivity* **10** 728-731

[22] Aubert G, Berthier C, Debray F, Horvatic M, Joss W, Martinez G, Mossang E, Picoche J, Bonito-Oliva A, Wilson M, Kramer S, and Mehring M 2000 *IEEE Transactions on Applied Superconductivity* **10** 732-735

Chapter 8

Development of High Temperature Superconducting Coils Using Bi-2223/Ag Tapes

8.1 Introduction

Since the discovery of high temperature superconductors (HTS) in 1986, significant work has gone into improving the properties of the materials. We have now reached a period when conductors can be produced over long lengths [1,2] making large scale magnet applications realistic. Multifilamentary HTS cuprates remain the most likely candidates, in particular the Bi-2223 phase due to the high J_c properties that can be produced in long lengths using powder route processing [2-4]. There are three main areas of applications development for these conductors; 1) High temperature, low field applications ($B < 1$ T) allowing relatively cheap liquid nitrogen to be used a coolant; 2) Medium field magnets ($2 \text{ T} < B < 10$ T) operating at temperatures of 20-30 K, enabling the easy use of cryocoolers and 3) Very high field inserts (> 20 T) for use at 1.8-4.2 K temperatures, taking advantage of the high J_c and B_{c2} values. For example a 1000 m Bi-2223/Ag tape was used to produce a magnet [2] which produced a self-field of 4 T at 4.2 K, 1 T in 20 T background field and 0.37 T in a 23 T background field [5]. A more detailed review of international magnet technology is presented in Chapter 9.

In this chapter the development stages of the Durham HTS coil winding project are reported. The design and fabrication of six double wound pancake coils from Bi-2223 multifilamentary tape using the react and wind route are presented. These coils were tested electrically and their performance analysed before being stacked to form a 98 mm bore HTS magnet. Although the technology presented in this chapter is no longer state of the art, the technical knowledge and experience gained from this work provided the foundations for the 1.29 T magnet project presented in Chapter 9.

The development of the fabrication technique is reflected in the different materials used during fabrication of the coils. The coils are numbered from 1 to 6 in chronological order, Coil 1 being the first to be fabricated. Coils 5 and 6 were wound after the individual electrical testing of the first four coils was complete and used in the magnet. Two of the pancakes have been impregnated with wax and four with resin. The self field generated for the coils has been calculated. The bore for these coils is 98 mm which produces a bending strain on the tape of about 0.3%. Since strain measurements on short samples show that J_c markedly decreases at strain values of typically 0.3% [6,7], the handling of the tapes during the fabrication procedure must be kept to a minimum. The voltage-current characteristics have been measured for all sections of the coils in liquid nitrogen and helium in self-field. In addition, J_c measurements have also been made on short samples of the tape used to fabricate the coils at 77 K in fields up to 300 mT and at 4.2 K in fields up to 1 T. These data allow us to assess the performance of the coils. Finally the six coils were stacked to form a magnet. We report on the electrical properties of all sections at 4.2 and 77 K in magnet operating mode and the bore field generated.

Section 8.2 describes the fabrication procedure of the pancakes and magnet. In Section 8.3 we outline the self field produced by an individual coil and the bending strain of the tape. The experimental results for the short sample and of the coils in both individual and magnet configurations are presented in Section 8.4. Finally we discuss the results and conclusions from this work.

8.2 Fabrication procedure

8.2.1 Coil Fabrication Procedure

Three different 37 filament Bi-2223/Ag tapes fabricated using the powder-in-tube route were used to fabricate the coils. Table 8.1 presents the cross-section, fill factor and I_c of the three tapes. The I_c values quoted were measured over a 100 m length of tape. The important differences between the tapes are discussed in Section 8.4.

	Tape 1	**Tape 2**	**Tape 3**
No. Filaments	37	37	37
Tape cross-section	0.854 mm^2	0.961 mm^2	0.973 mm^2
Fill factor	36.2 %	29.5 %	32.0 %
I_c of 100 m length at 77 K	20 A	25 A	27 A

Table 8.1. The main parameters and dimensions of the Bi-2223 tapes.

The basic construction of all double pancakes was similar and is shown by Figure 8.1, a photograph is presented in Figure 8.2. The Tufnol former was held in the chuck of a lathe. The superconducting tape and the insulating Mylar are co-wound onto the former from two separate spools by slowly rotating the chuck. There is little tension in the tape to minimise strain damage. However the insulator is tensioned to ensure the packing factor of the coil remains high. The former has six slots to enhance cooling for the inner turns. Each double wound pancake consists of 2 oppositely wound pancakes insulated from each other by a ring of Kapton. In Table 8.2, the total length of tape, the number of turns on each pancake and the impregnation material for each coil is shown. The individual pancakes were joined together using three electrical joints soldered to the bottom turn of each pancake, silver was used for coils 1-4 and Bi-2223 tape used for coils 5 and 6 producing a lower resistance joint. Two current leads were connected to each coil by soldering a silver strip to the top layer of each pancake. Two copper voltage taps were also connected to each coil, one on the top layer and one on the bottom layer. This

	Coil 1	**Coil 2**	**Coil 3**	**Coil 4**	**Coil 5**	**Coil 6**
Bi-2223 tape used	1	1	2	3	3	3
Total length of tape	14 m	9 m	21.2 m	17.8 m	32.1 m	31.4 m
No. turns	20 + 19	15 + 12	30 + 30	25 + 23	47 + 47	47 + 45
Impregnation	Wax	Wax	Resin	Resin	Resin	Resin

Table 8.2. The main parameters of the double wound pancakes.

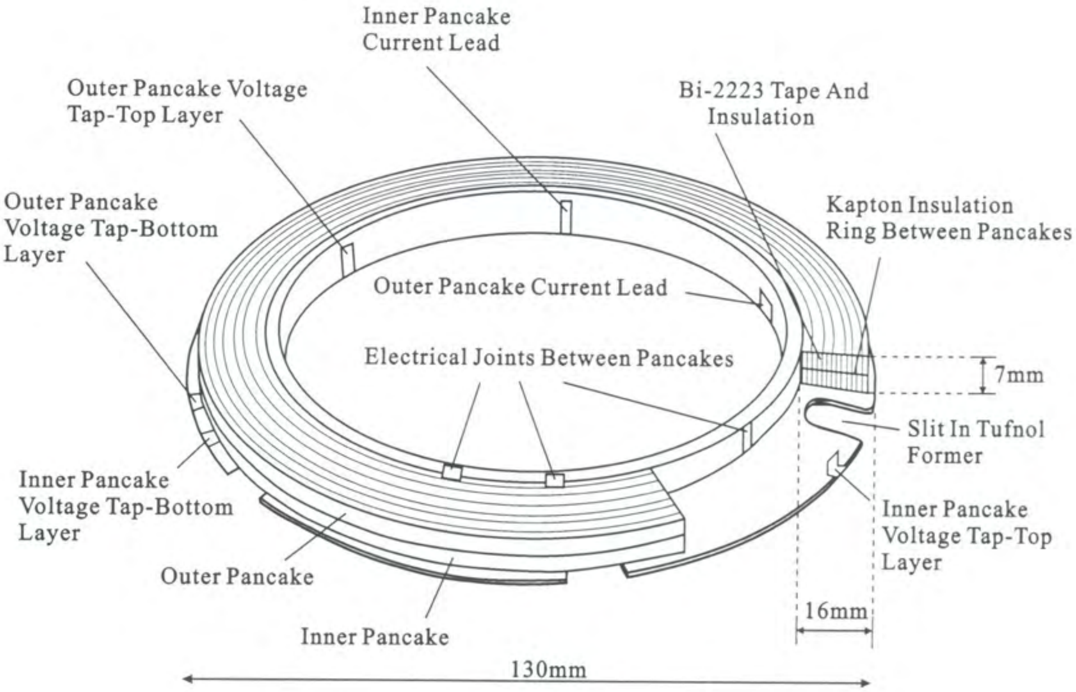

Figure 8.1. A schematic diagram of a Bi-2223/Ag double wound pancake showing a cross-section through the turns.

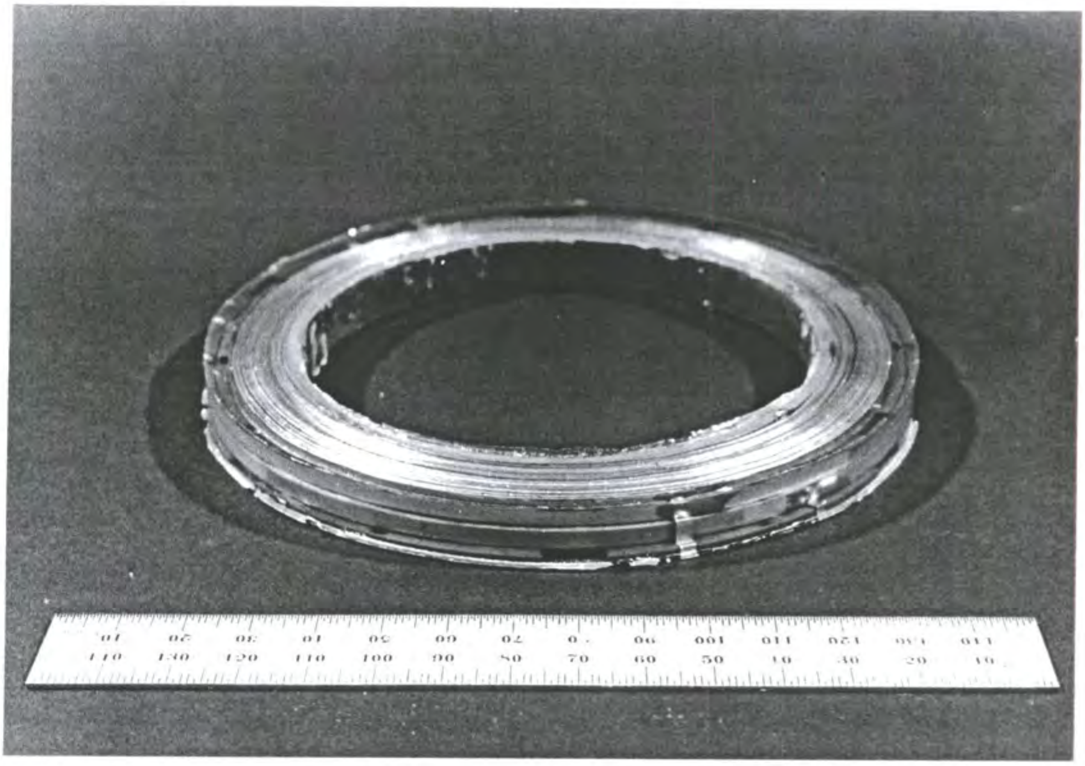

Figure 8.2. A photograph of a resin impregnated, 98 mm bore, double wound pancake.

configuration ensured that the critical current for each pancake and the joints between the pancakes could be tested individually as well as the whole coil. In making these connections, care was taken to limit mechanical damage to the tape by the soldering iron.

During impregnation the coils were held in PTFE moulds and vacuum impregnated at 0.1 mbar. Early coils were impregnated using wax. Each wax coil was heat-treated at 70^0C for 10 hours during which time the wax first melted and then impregnated the coil. Then the coil was slowly cooled to room temperature. The Ciba-Geigy resin system CY1300, HY906 and DY073 was used to impregnate Coils 3-6 due to its greater strength. First the coil and the mixed resin were out-gased for 24 hours at 50^0C. Then the resin was poured into the mould containing the coil. The temperature was ramped at 10^0C per hour up to 80^0C and the pressure increased to ambient pressure. The resin was then gelled for 18 hours at 80^0C. Then the temperature was again ramped at 10^0C per hour and finally the coil was cured for 11 hours at 120^0C. Room temperature resistivity measurements confirmed there were no short circuits in any of the coils.

8.2.2 Magnet fabrication procedure

The coils were stacked together using the room temperature curing Ciba-Geigy resin system CY1300 and HY1300. 0.5 mm thick copper plates were inserted between each coil to increase cooling. Coils were joined together electrically using Bi-2223 tape. The magnet was held together between 2 stainless steel plates and supported using stainless steel rods. Access to all voltage taps was available from the top plate. Current connections to the top and bottom of the magnet were made using Bi-2223 tape, also accessible from the top plate. The height of the magnet was 81.3 mm excluding plates with a 91 mm clearance bore. A photograph of the magnet is presented in Figure 8.3.

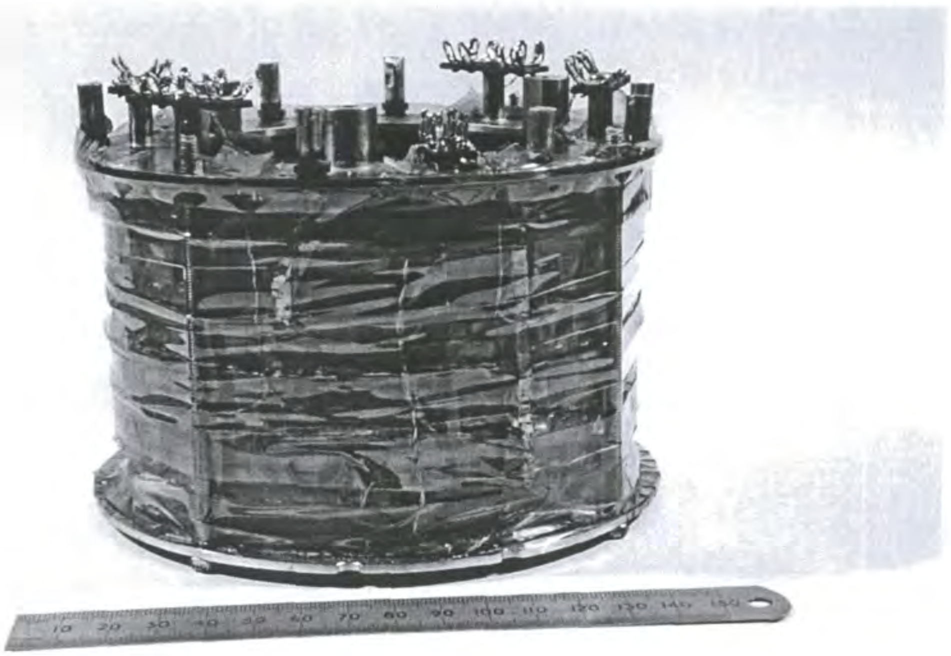

Figure 8.3. A photograph of the 98 mm bore Bi-2223 magnet containing 6 double wound pancakes.

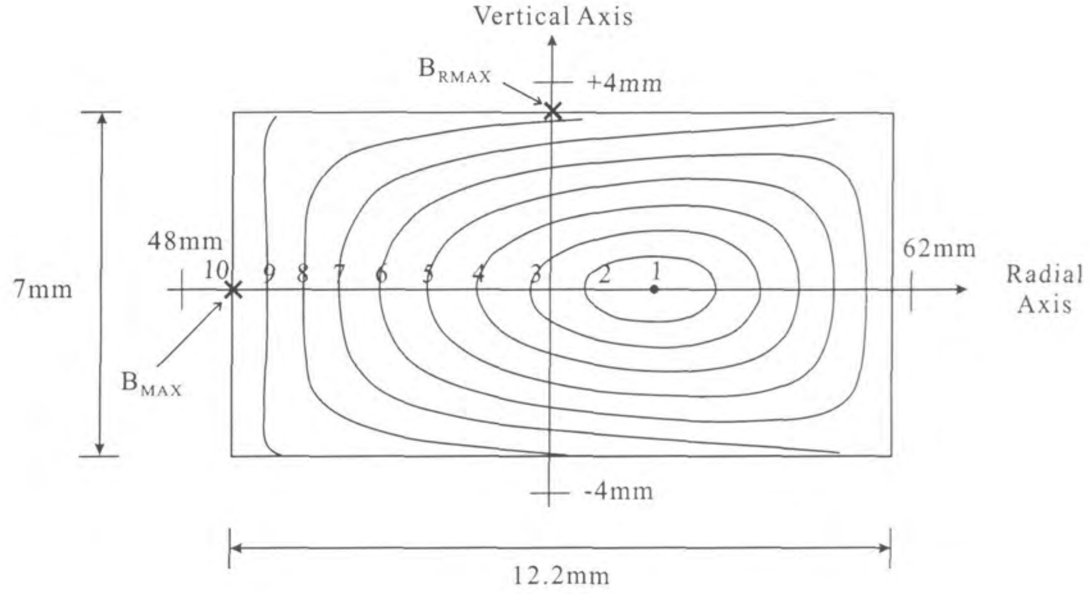

Figure 8.4. The field profile through a double wound pancake showing field line contours from zero field (contour1) up to a maximum field (contour 10).

8.3 Factors Determining Coil Performance

Two of the critical factors that affect the performance of HTS react and wind coils are the magnetic field produced by the coil and the bending strain of the tape. These are considered in turn.

The self-field profile within Coil 3 has been calculated and is presented in Figure 8.4. Similar contours occur for all the coils. The field is zero on contour 1 increasing in equal steps for subsequent contours out to a maximum at point B_{MAX} on contour 10. The distances on the radial axis are given from the centre of the pancake. Point B_{RMAX} shows the point in the coil with the highest field in the radial direction (i.e. the field parallel to the c-axis of the tape). The coil constant is 2.74 $mT.A^{-1}$ and $B_{RMAX} = 0.72 \times B_{MAX}$. The bending strain exerted on the tape has been calculated using $\varepsilon = t/D$, where t is the thickness of the tape and D is the bending diameter of the pancake. With the tape thickness of 0.33 mm and bending diameter of 98 mm the bending strain on the tape is ~0.3%.

8.4 Experimental Techniques and Results

8.4.1 Short Sample Measurements

Critical current density transport measurements were taken on short samples of Tape 1 as a function of field at 77 K from 0 T up to 300 mT and at 4.2 K up to 1 T Data was taken with the sample in 3 orientations with respect to field. Using these data we can determine the self field limitations for the coils. Samples were cut to 20 mm in length and mounted on tufnol. A four terminal measurement was used with voltage taps connected using silver paint and separated by 6 mm and the current leads soldered to the tape. A criterion of 1.5 μVcm^{-1} was used to calculate I_c. At 77 K the field was applied using a resistive copper magnet and results were taken during 1.5 field cycles - in increasing, decreasing and increasing field - to study any hysteretic effects of field on J_c. Data were taken every 10 mT up to 100 mT and thereafter every 20 mT. At 4.2 K data was taken using a 15 / 17 T superconducting magnet in increasing field only.

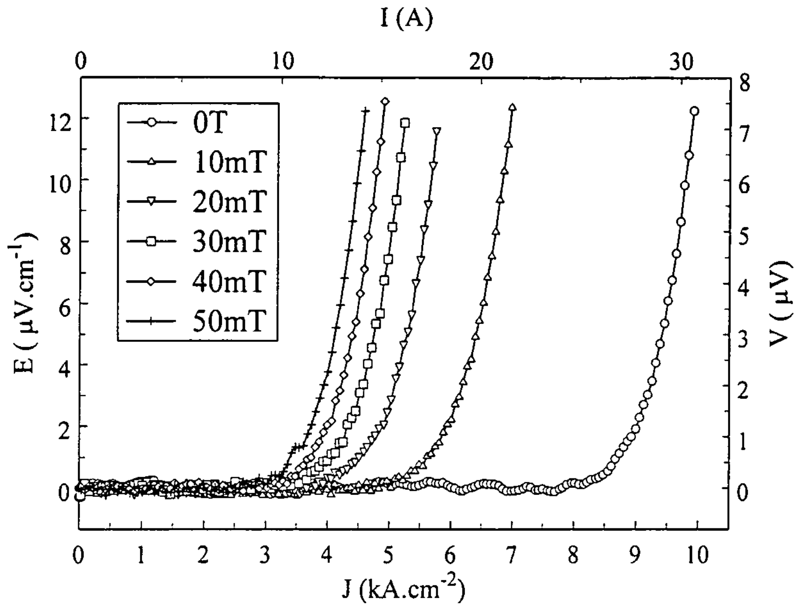

Figure 8.5. The electric field-current density characteristics of a short sample of Tape 1 every 10 mT up to 50 mT at 77 K. The field is applied parallel to the c-axis and perpendicular to current.

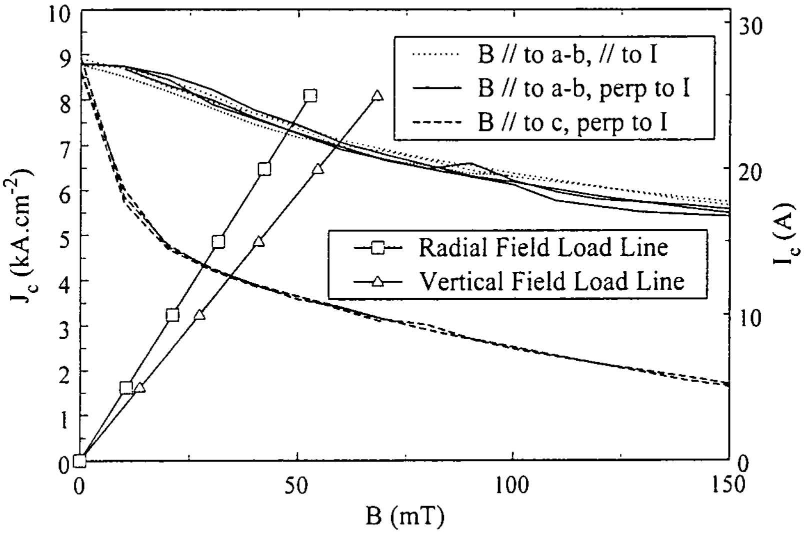

Figure 8.6. The critical current density (J_c) as a function of field at 77 K up to 150 mT for three orientations of the tape with respect to field. Measurements taken on a short sample of Tape 1. Also shown are the radial and vertical field load lines for the double wound pancakes. Data taken over 1.5 field cycles.

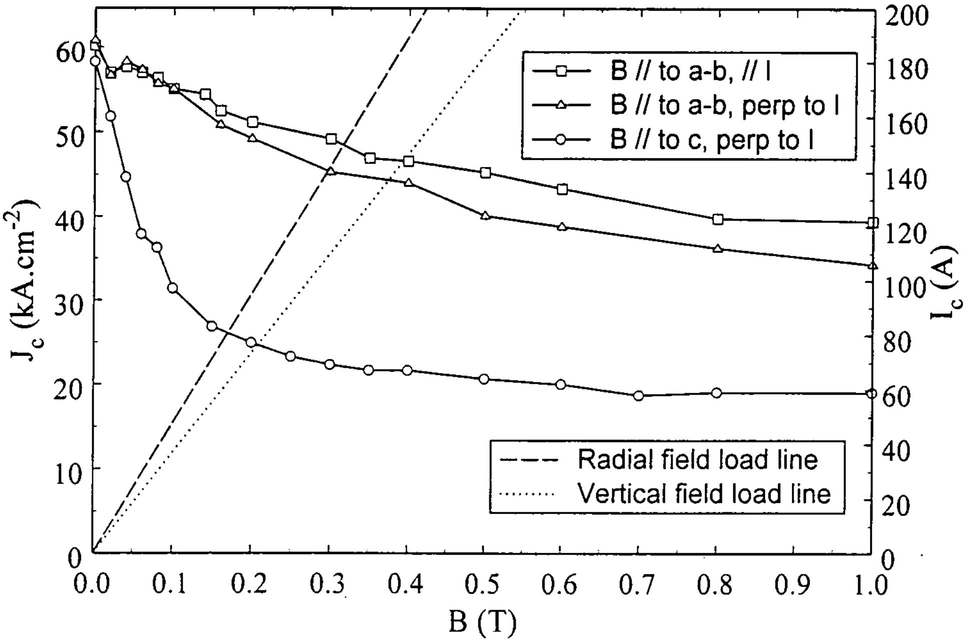

Figure 8.7. The critical current density (J_c) as a function of field at 4.2 K up to 1 T for three orientations of the tape with respect to field. Measurements taken on a short sample of Tape 1. Also shown are the radial and vertical field load lines for the double wound pancakes.

Figure 8.5 shows some detailed electric field - current density characteristics over the first 50 mT in the orientation field parallel to the c-axis. The baselines are flat to within the limits of the experiment indicating there is very little damage to the sample. The n-index has been calculated using the standard equation $V=\alpha I^n$ where n is the index of transition. From the data in Figure 8.5 it was found that in zero field at 77 K the short sample value for n is 18.7 and at 30 mT, n is 9.4. In Figure 8.6 we present the short sample data taken at 77 K, we expect the short-sample data for all three tapes to be similar. The orientation with field parallel to the c-axis shows the strongest I_c field dependence dropping from 28 A in zero applied field to 13.2 A at 30 mT. Eventually I_c dropped to 1.9 A at 280 mT. The two orientations parallel to the a-b planes are similar to each other. They have a much weaker dependence dropping to 14.5 A at 250 mT. Very little hysteresis in I_c is found in any of the data although the decreasing field values are slightly higher due to trapped flux within the superconductor. The 4.2 K data presented in Figure 8.7 shows a similarly strong $I_c(B)$ dependence in the c-axis orientated direction and again a much weaker field dependence was observed with field applied parallel to the a-b planes.

8.4.2 Double wound pancake test results

The voltage-current characteristics of each coil were measured at 4.2 and 77 K using a four terminal dc technique. A criterion of 1.5 μVcm^{-1} was used to define I_c. In Figures 8.8 and 8.9 the voltage-current characteristics are shown for the three components of Coil 3 at 77 K and 4.2 K respectively - the two individual pancakes and the joint. It can immediately be seen that the *n*-index of transition for the pancakes is similar to that of the short sample (cf. Figs 8.5, 8.6 and 8.7). In Table 8.3 we present data taken on all 6 individually energised coils at 77 K. Coils 1 to 4 were also tested individually at 4.2 K and the results shown in Table 8.4, no results are presented for Coils 5 and 6 at 4.2 K since these were fabricated after the 4.2 K testing.

8.4.3 Results of Magnet Testing

After magnet fabrication the electrical properties of the each coil was tested within the magnet configuration. Current was passed through the entire magnet (operating mode) and the voltage measured across each constituent section at both 4.2 and 77 K. The performance of each section is presented in Table 8.5. The I_c values in the magnet configuration are different from those with the coils individually energised, Tables 8.3 and 8.4, due to self field effects of the magnet, discussed further in Section 8.5 and Chapter 9. The critical current for the magnet was 90 A at 4.2 K and the maximum field constant on the bore was 3.29 mT.A^{-1}.

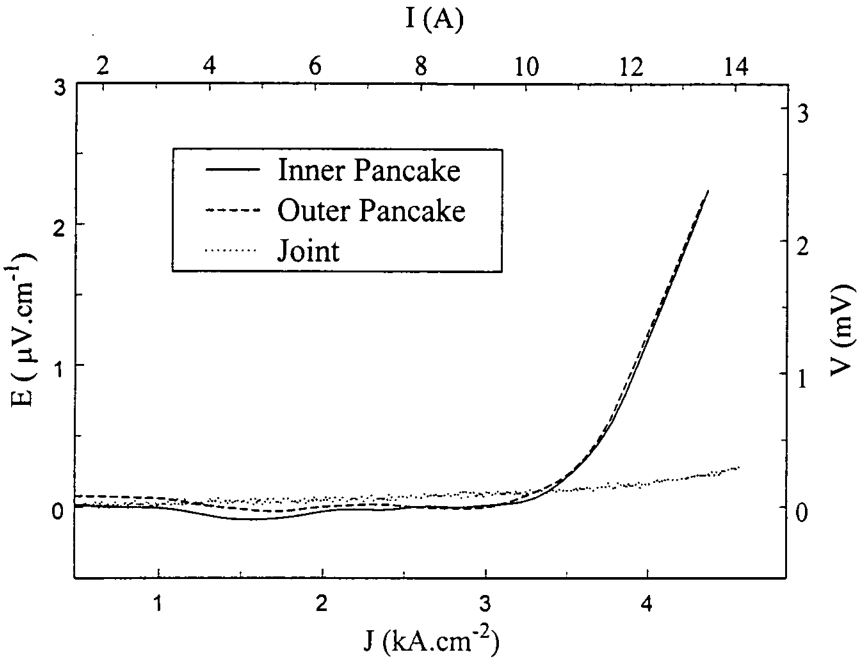

Figure 8.8. The electric field-current density characteristics at 77 K of a double wound pancake (Coil 3).

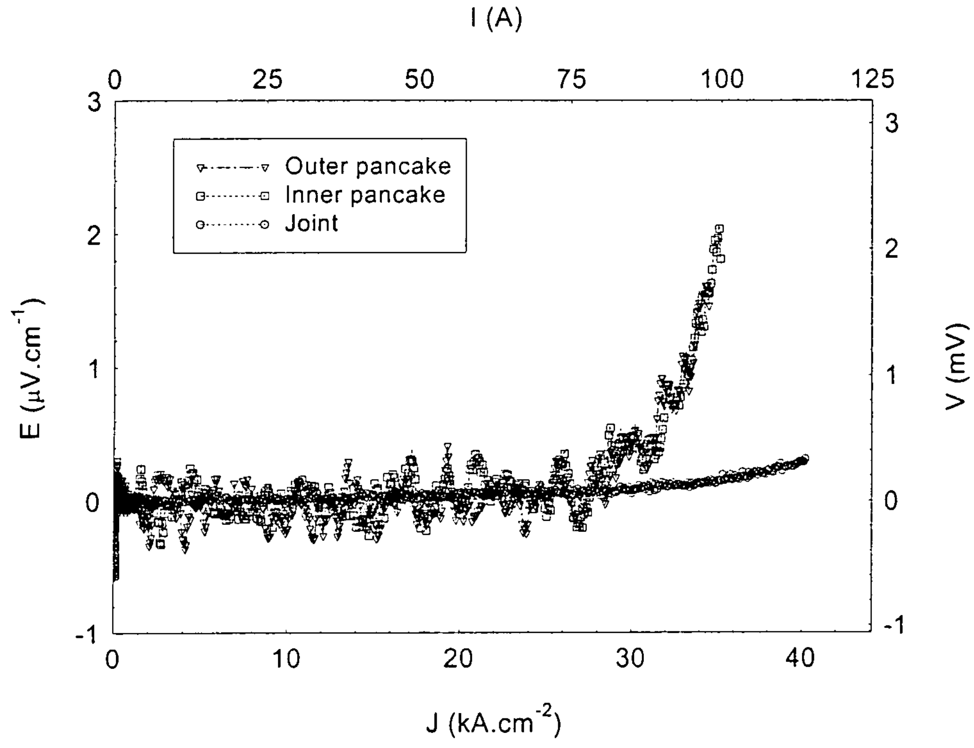

Figure 8.9. The electric field-current density characteristics at 4.2 K of the double wound pancake (Coil 3).

	Coil 1	**Coil 2**	**Coil 3**	**Coil 4**	**Coil 5**	**Coil 6**
Inner pancake I_c	13.3 A	14.5 A	12.3 A	14.5 A	14.9 A	10.7 A
n-index	3.7	6.2	11.3	10.0	11.8	-
Outer pancake I_c	13.9 A	14.5 A	12.3 A	14.4 A	10.9 A	12.1 A
n-index	2.5	6.9	11.4	9.2	-	9.1
Joint resistance	10 μΩ	22 μΩ	10 μΩ	10 μΩ	2 μΩ	4 μΩ

Table 8.3. Critical current (I_c) and n-index of the double wound pancakes at 77 K in self-field when individually energised.

	Coil 1	**Coil 2**	**Coil 3**	**Coil 4**
Inner pancake I_c	99 A	99 A	97 A	104 A
Outer pancake I_c	103 A	105 A	96 A	104 A

Table 8.4. Critical current (I_c) of the double wound pancakes at 4.2 K in self-field when individually energised.

	I_c at 4.2 K (A)			**I_c at 77 K (A)**		
	Inner	Outer	Whole	Inner	Outer	Whole
Coil 2 (Top)	73.0	72.4	72.5	10.2	11.0	10.2
Coil 6	78.2	85.2	80.2	11.4	11.2	10.9
Coil 4	113	110	109	15.1	14.6	14.9
Coil 3	99.6	96.6	89.0	12.2	12.2	12.2
Coil 5	84.7	90.8	86.3	12.2	13.3	12.5
Coil 1 (Bottom)	71.9	83.7	75.9	10.7	12.5	10.6

Table 8.5. Critical current (I_c) of the double wound pancakes at 4.2 and 77 K in the magnet configuration. The results are presented for the inner and outer pancakes and the whole coil with the coils in their respective magnet positions.

8.5 Discussion

From the calculations of the field contours within the individually energised coils (Figure 8.4), the load lines which define the field produced per Amp by the coil have been calculated for point B_{MAX} - vertical field load line and point B_{RMAX} - radial field load line. The intercept between these load lines, shown in Figures 8.6 and 8.7, and the J_c characteristics show the ideal performance were the short sample values of current density achieved throughout the turns. The intercept between the critical current data for B parallel to c-axis and the radial field load line occurs at a lower current than the intercept for B parallel to a-b and the vertical field load line. Therefore the performance of the coil is determined by the conditions at point B_{RMAX} in Figure 8.4 where the local field lines are parallel to the c-axis of the tape. The ideal critical current is predicted to be about 13.5 A at 77 K giving a B_{RMAX} of 28 mT and B_{MAX} of 39 mT, and 80 A at 4.2 K giving a B_{RMAX} of 166 mT and B_{MAX} of 231 mT. Tables 8.3 and 8.4 and the data in Figures 8.5 and 8.7 confirm that these critical current values have been achieved in practice.

The index values for the coils characterise the performance of the coils at low electric field values. It can be seen from Table 8.3 that Coils 1 and 2 have markedly lower n-values than Coils 3 -6 ($n \sim 10 - 11.8$) or the short sample ($n \sim 9.4$ at 30 mT). We suggest that this result is consistent with the relatively low I_c value for Tape 1 over long lengths (~20 A) compared to short sample currents (~28 A) and suggests damage to the tape prior to coil fabrication. The values of the n-index for the resin impregnated coils using Tapes 2 and 3, are actually slightly higher than that of the short sample. This confirms that independent of the E-field criterion used to define I_c, the coil performance is very close to that expected for undamaged turns limited by self-field.

Within the fully energised magnet the I_c values are found to vary from the individually energised coil values due to self-field effects within the magnet. In magnet operating mode the field at the top and bottom of the magnet is more closely aligned to the c-axis of a greater percentage of turns. Since the c-axis orientated field dependence is much stronger than the equivalent a-b orientated behaviour (c.f.

Figures 8.6 and 8.7) the I_c of the outermost pancakes is reduced. This can be observed in a reduction in the I_c values of Coils 1 and 2 at both 4.2 and 77 K within the magnet configuration compared with those of the same coils when individually energised. Conversely the field in the central regions of the magnet is more closely aligned to the a-b planes within an increased number of turns and hence the I_c values of Coils 3 and 4 are higher within the magnet configuration. The field profile within magnets is studied in greater detail in Chapter 9.

8.6 Conclusions

As part of the magnet technology in Durham, six large bore double wound pancakes have been fabricated from 37 filament Bi-2223/Ag tapes, produced by the powder in tube route, using the react and wind technique. The self field produced within the windings of the individually energised coils has been calculated. Measurements have also been completed on short samples to determine the dependence of I_c on the orientation and magnitude of the field at 4.2 and 77 K. Although the bending strain in the pancakes is similar to the maximum that can be sustained by these brittle materials, the performance of the coils is almost entirely self field limited. This work has provided the required technical knowledge and experience to design and fabricate a state of the art HTS magnet presented in Chapter 9.

References for Chapter 8

[1] Balachandran U, Iyer A, Jammy R, Chudzik M, Lelovic M, Krishnaraj P, Eror N, and Haldar P 1997 *IEEE Transactions on Applied Superconductivity* **7** 2207-2210

[2] Sato K, Ohkura K, Hayashi K, Ueyama M, Fujikami J, and Kato T 1996 *Physica B* **216** 258-260

[3] Sato K, Hikata T, and Iwasa Y 1990 *Applied Physics Letters* **57** 1928-1929

[4] Sato K, Hikata T, Mukai H, Ueyama M, Shibuta N, Kato T, Masuda T, Nagata M, Iwata K, and Mitsui T 1991 *IEEE Transactions on Magnetics* **27** 1231-1238

[5] Sato K, Shibuta N, Mukai H, Hikata T, Ueyama M, Kato T, and Fujikami J 1993 *Cryogenics* **33** 243-246

[6] Ekin J, Finnemore D, Li. Q, Tenbrink J, and Carter W 1992 *Applied Physics Letters* **61** 858-860

[7] Suenga M, Fukumoto Y, Haldar P, Thurston T, and Wildgruber U 1995 *Applied Physics Letters* **67** 3025-3027

Chapter 9

Design, fabrication and performance of a 1.29 T Bi-2223 magnet system

9.1 Introduction

Since the discovery of Bi-based high temperature superconducting ceramics [1,2], an enormous effort has gone into improving the critical current density (J_c) of these materials. In short samples, J_c of $6.9\text{x}10^4$ Acm^{-2} [3] and $7.3\text{x}10^4$ Acm^{-2} [4] has been achieved in zero-field at 77K. High-field applications rely on using high performance tapes of kilometre lengths. In the Bi-2223 system, this level of performance is now being realised with J_c of $1.2\text{x}10^4$ Acm^{-2} reported over 1260m [5], $1.8\text{x}10^4$ Acm^{-2} over 250m [6] and over $2\text{x}10^4$ Acm^{-2} achieved in 1200m[7], 1000m [8] and 400m [9] lengths at 77 K in self field. It is expected that J_c will increase yet further, perhaps by an order of magnitude [10], as our understanding of the tape processing improves.

The high current carrying capacity of Bi-2223 up to 30 K [7,11,12] enables production of compact cryogen-free magnet systems. Cryogen-free systems are attractive because: i) easy operation is facilitated since no cryogen is required, ii) cooling efficiency at 20K is approximately five times higher than at 4K making refrigeration more economical, iii) thermal stability and fast magnet sweep rates are possible because the specific heat of the tapes is about two orders of magnitude higher at 20K than 4K. Cryogen-free Bi-2223 systems have been fabricated using stacked pancake coils producing fields of 7.25T [13] and 7T [14] at around 20 K. The high upper critical field of Bi-2223 also facilitates the production of high-field inserts. A record field of 24 T at 4.2 K [7] was achieved from a Bi-2223 insert in a 22.54 T background field, the same magnet producing 2.3T at 4.2 K in self-field. A magnet producing 3.2 T in self-field and 1 T at 4.2 K in a background field of 20 T has been fabricated [5]. Inevitably the enormous effort producing large scale Bi-

2223 magnets and inserts has lead to the proprietary use of materials and commercial know-how.

Increasing opportunity for fabricating laboratory scale magnets in 1 - 5 T range operating at temperatures below 30 K will follow the improvements in J_C of Bi-2223 tapes. Laboratory scale magnets have been produced using both the "react-and-wind" (R+W) and "wind-and-react" (W+R) processes. Using R+W, 1 T has been generated [15] from 8 R+W double-wound pancakes at 4.2 K. At 20 K, 1.1 T was achieved from 17 R+W double-wound pancakes [16]. Using W+R, a Bi-2223 coil with a 15 mm bore generated a field of 1.34 T at 4.2 K[17] and Bi-2212 inserts have produced 2.6 T in self-field and 1.08 T in a background of 20 T at 4.2 K [18]. This paper outlines fabrication of a laboratory scale magnet produced without the use of the specialist equipment (e.g. tape winding machines).

In Section 9.2, J_c data for short samples of Bi-2223 tape to assess the effects of magnetic field, strain and anisotropy are presented. In Section 9.3, the design and fabrication procedure for the Bi-2223 magnet system consisting of six double wound pancakes is presented. Since the design parameters of any laboratory scale magnet are specific to the application including magnitude of field, field homogeneity, reinforcement of the structure and bore size, alternative available fabrication options are also discussed. In Section 9.4, J_c data for the magnet and all constituent pancakes at 4.2 K and 77 K are presented. Axial field profiles of the magnet, measured using a Hall probe, are compared with calculations. The electric field - current density (E-J) characteristics of all pancakes were measured both with each coil (i.e. double pancake) individually energised and with the magnet energised to assess the reliability of the fabrication route. In Section 9.5, the performance of the coils and pancakes is compared with calculations which together demonstrate that the magnet presented produced a field close to short-sample performance. The Discussion considers the data presented and suggests a series of experiments required to assess efficiently the suitability of a particular tape for a particular application. In this chapter, sufficient detail is included so that the non-specialist can assess the performance of available brittle superconducting tapes for magnet technology and then design and fabricate a react-and-wind laboratory scale magnet using pancake coils with equipment available in any well-founded laboratory.

9.2 Measurements on a short sample of a Bi-2223 Tape

Once the basic design parameters of magnet bore size and dimensional restrictions are determined (c.f. Section 9.4), the field strength of modern magnets is almost entirely determined by the performance of the superconducting wire or tape [19]. In our magnet, system restrictions include a minimum bore diameter of 40 mm, maximum outer diameter of 82 mm and use of the react-and-wind conductor. In this section, short samples of the Bi-2223 tape used to fabricate the magnet are characterised. The tapes used were 37 filament Bi-2223 alloy sheathed tape fabricated via the powder in tube (PIT) route with J_c of 8.3 x 10^4 A.cm^{-2} (4.2 K, 0 T) across the superconducting cross-section. The parameters of the two constituent tapes are presented in Table 9.1. In Bi-2223, it is known that J_c is strongly dependent on the magnitude of field [7,11,12], angle of applied field[20-26] and strain[27-30].

Figure 9.1 shows the effects of thermal and mechanical cycling on the critical current density of Tape 1 at 77 K and zero field using 100 mm samples. Straight sample J_c was measured as 1.18 x 10^4 A.cm^{-2} (77 K, 0 T) using criteria of 1.5

	Tape 1	Tape 2
Material	Bi-2223	Bi-2223
Sheath	Silver alloy Ni/Mg	Silver alloy Ni/Mg
Thickness (mm)	0.33	0.29
Width (mm)	3.3	3.5
No. filaments	37	37
Fill factor (%)	28	28
Length of tape (m)	120	70
I_C of sections along tape length at 77K, zero magnetic field (A)	35-38	33-35

Table 9.1. Main parameters and dimensions of the Bi-2223 tapes.

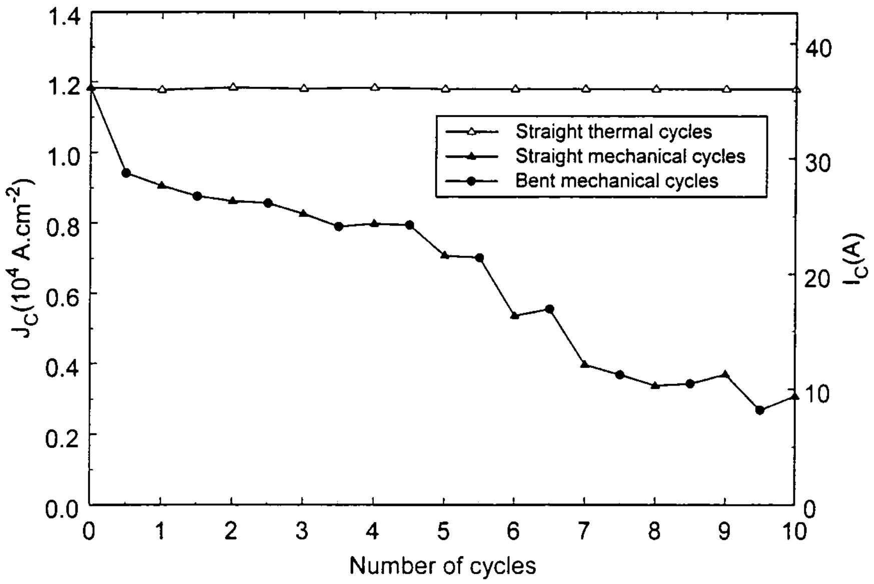

Figure 9.1. The critical current density (J_c) of thermally and mechanically cycled 100 mm samples of Bi-2223 tape at 77 K. The open symbols (Δ) are for thermally cycling alone. The closed symbols are for a tape that is bent (•) and J_C measured and then straightened (▲) and remeasured for 10 cycles.

$\mu V.cm^{-1}$. After 10 thermal cycles no degradation was observed in J_c within the experimental limits. In a second experiment, the sample was mechanically cycled by bending it around a 44 mm diameter (the diameter of the inner turn of the magnet) and re-straightened. J_c was measured in each configuration (1 thermal cycle includes two J_c measurements) during 10 mechanical cycles. The first mechanical cycle produced a permanent decrease in J_c of ~ 20 %. Eventually the J_c degraded by ~ 75 % from straight sample performance.

The field dependence of J_c was measured using 30 mm samples of Tape 1 at 4.2 K in fields up to 15 T. Measurements were taken on a straight sample (0 % strain) and a sample bent on a 44 mm diameter (0.55 % strain). Strain values quoted in this paper were calculated using $\varepsilon = t / D$ where t is the thickness of superconductor (0.24 mm) and D is the bending diameter. J_c of the tape was 8.3 x 10^4 $A.cm^{-2}$ (4.2 K,

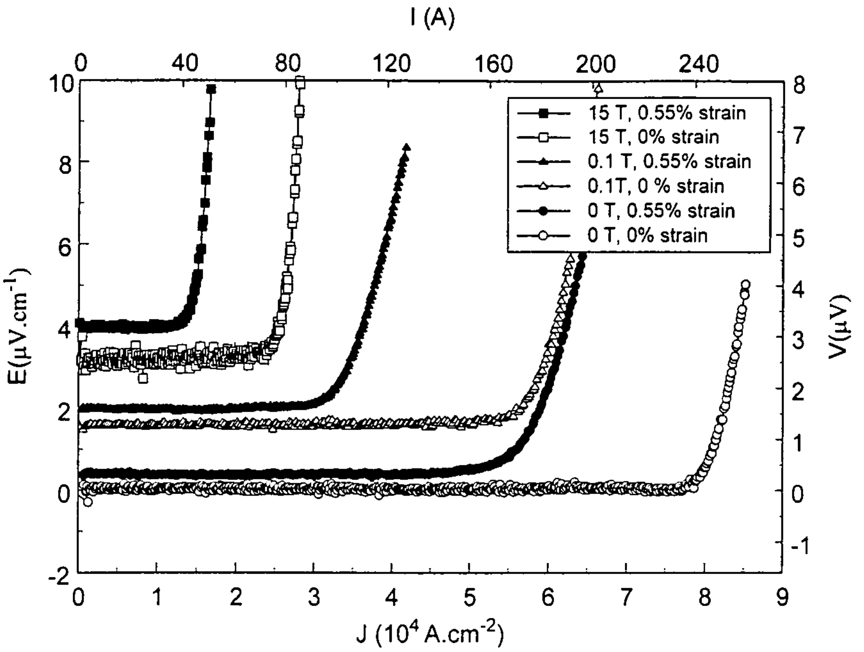

Figure 9.2. *E-J* traces for short samples of Bi-2223 tapes at 0 % and 0.55 % strain at 4.2 K in fields up to 15 T.

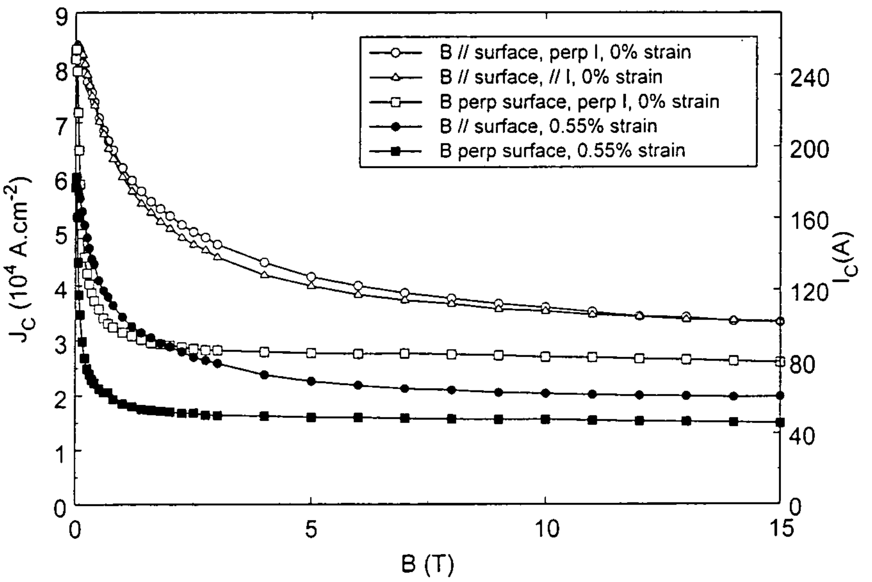

Figure 9.3. The critical current density as a function of magnetic field for a short sample of Bi-2223 Tape 1 at 0 % and 0.55 % strain with field aligned parallel and perpendicular to the tape surface. All data taken at 4.2 K.

0 T, $\varepsilon = 0$ %) and 5.82×10^4 A.cm^{-2} (4.2 K, 0 T, $\varepsilon = 0.55$ %). Data were taken with the field applied in 2 and 3 orthogonal directions with respect to the surface of the tape for the 0.55 and 0 % strained samples respectively. Typical *E-J* characteristics are presented in Fig. 9.2 for the field applied parallel to the tape surface (B parallel to a-b planes) in fields up to 15 T. At all fields the strain degrades J_c. However all traces produce flat baselines to within the noise (200 nV peak-to-peak) suggesting that undamaged filaments of zero resistance exist within the strained sample. In Fig. 9.3, the J_c for Tape 1 at 4.2 K in fields up to 15 T with field applied parallel and perpendicular to the tape surface at 0 and 0.55 % strains were determined using a criterion of 1.5 μV.cm^{-1}.

Once the short sample behaviour of the conductor has been measured the optimum performance of the magnet can be calculated prior to magnet fabrication assuming that short sample performance is achieved in long lengths. These calculations are addressed in Section 9.4.

9.3 Magnet Fabrication

9.3.1 Magnet Windings

The choice of conductor determines whether the react-and-wind (R+W), wind-and-react (W+R)[6,17,31,32] or wind, react and tighten (WRAT) [18,33] are most suitable. W+R routes have facilitated the production of pancake coils with radii ~ 5 mm showing no degradation in J_c [31]. The degradation in tape performance from the more simple R+W technique due to strain on the conductor that was used in this work, should be weighed against the high melting point insulation and accurate reaction conditions for the coils required in the W+R technique. We calculate that a ~ 20 % increase in maximum field would have occurred had a strain-free W+R technique been used.

Powder-in-tube (PIT) tape was used in this magnet. There is a continuing effort to improve processing of PIT tapes, in which precursor powders are packed into silver alloy tubes, drawn and pressed into a tape and processed in complex

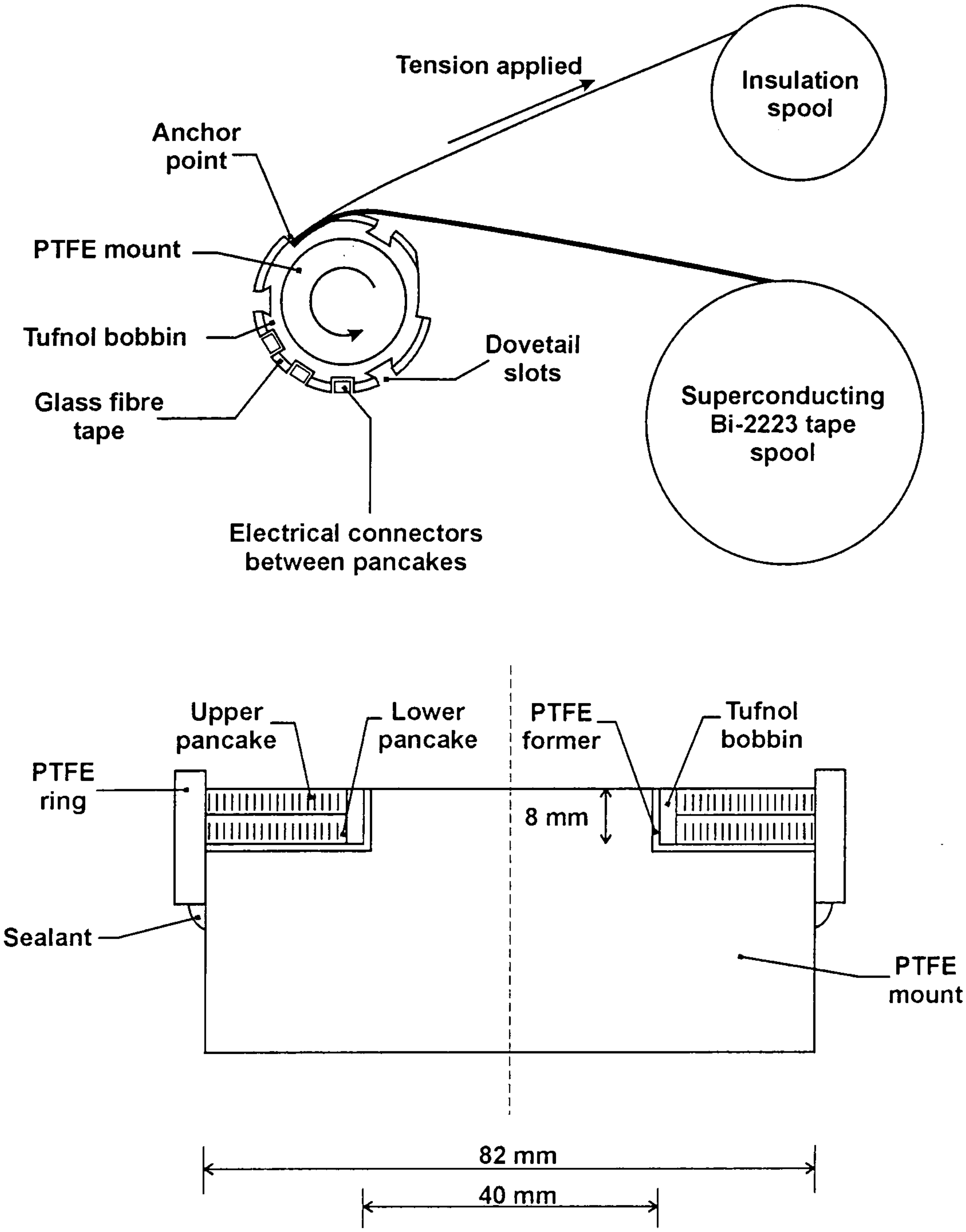

Figure 9.4. (a) The experimental arrangement for winding the tape and insulation onto the tufnol bobbin (b) The PTFE components used during the vacuum resin impregnation.

thermomechanical heat-treatment schedules [5,34-41]. Other long-length tapes include dip coating[18,33,42] and electrophoretic deposition[43].

The tape was wound onto tufnol bobbins of thickness 2 mm and inner diameter 40 mm. Tufnol was chosen primarily because of its electrically insulating properties and ease of use but also due to its adequate fracture stress and similar thermal contraction to the epoxy. Copper and other metallic based materials have been used with the advantages of higher thermal conductivity and high strength which can be important in large magnets [7,15,16]. Ceramic formers are used in W+R magnets due to their refractory properties [6,32].

The bobbins were covered by a single layer of glass fibre tape and placed on a PTFE mount as shown in Fig. 9.4(a). Each coil contained two oppositely wound pancakes joined together at the bottom turn using Bi-2223 strips. The tape was wound into anchor points in the tufnol bobbin and soldered across the short orthogonal tapes that provided electrical connections between the two pancakes. The superconducting tape was co-wound with non-adhesive polyimide (Kapton) tape of thickness ~ 60 μm to provide turn-to-turn insulation as shown in Fig. 9.4(b). The insulator was tensioned during winding to maximise the radial packing factor although the superconductor was not tensioned in order to minimise damage. Polyimide is usually selected since it is an insulating material available in thin tape form (~ 60 μm) which has a high (short period) melting point of 310°C and reasonable strength (for winding under tension) [7,14,16,44]. Alternatives include mylar, braid or a varnish coating for R+W [45,46] and alumina based slurries for W+R coils[6,17,31,32,47,48]. Two polyimide sheets were inserted to provide pancake-pancake insulation. After the first pancake was wound, the superconducting spool was turned round and repositioned so that the strain was minimised (i.e. the tape was not straightened) while winding the second pancake. Finally a Bi-2223 current lead was soldered to the outer turn of each pancake and copper voltage taps were soldered on the inner and outer turn of each pancake to facilitate diagnostic measurements on all sections of the coil. Six double-wound pancake coils were fabricated. The parameters of each coil are presented in Table 9.2.

	Coil 1 (top)			Coil 2			Coil 3			Coil 4			Coil 5			Coil 6 (bottom)		
Pancake	lower	upper	whole	lower	upper	whole	lower	upper	whole	lower	upper	whole	lower	upper	whole	lower	upper	whole
Tape	1	1	-	1	1	-	1	2	-	2	2	-	1	1	-	1	1	-
Height (mm)	-	-	8.5	-	-	8.0	-	-	8.5	-	-	8.5	-	-	8.5	-	-	9.5
Number of turns	43	41	84	43	43	86	43	50	86	50	50	100	43	43	86	43	39	82
Length of tape (m)	8.51	8.11	16.62	8.51	8.51	17.02	8.51	9.90	18.41	9.90	9.90	17.80	8.51	8.51	17.02	8.51	7.72	16.23
Packing factor (%)	-	-	64.0	-	-	69.6	-	-	65.8	-	-	66.0	-	-	65.5	-	-	55.9

Table 9.2. Main parameters of constituent coils of the Bi-2223 magnet.

The windings of a superconducting magnet system must be completely impregnated by insulating material that ensures the turns do not move when the magnet is energised. Such movement can quench the magnet and damage the brittle conductor. Ideally the impregnant should have a high fracture stress at operating temperature, have similar thermal contraction properties to the superconductor and be adhesive to the turns. Standard choices are wax (often preferred for small coils which are seldom thermally cycled) and resin (Araldite or Stycast) [46,49]. The thermal and mechanical properties vary for different resin systems but for small magnets the ease of use and pot-life are primary considerations [50-54]. To key the resin to the bobbins, dove tail slots were incorporated into the bobbin (c.f. Fig. 9.4(a)). For the magnet presented here, a Ciba-Geigy resin system CY1300 (resin), HY906 (hardener), DY073 (accelerator) mixed in the ratio 100 : 80 : 2 by weight respectively was used. During impregnation the coils and resin were held in the PTFE parts which constitute the mould shown in Fig. 4(b). PTFE was used because of its non-stick properties. The resin was degassed for 12 hours at 50°C. The coil was then impregnated with resin under vacuum at 50^0C. On completion of impregnation, the system was let up to atmospheric pressure to drive the resin into the turns. The temperature was then increased to 80^0C and held for 16 hours before curing at 120°C for 8 hours. A minimum volume of resin was used to avoid any resin-rich areas that are particularly liable to crack during thermal cycling. The coil was removed from the PTFE mould after curing.

In a solenoid the Lorentz forces act to compress the magnet axially and explode it radially. These forces act to deform the constituent materials which will modify J_c and can if excessive lead to catastrophic failure. Formulae for calculating stresses in magnets are well-established [46]. If the fracture stress of any of the constituent materials is exceeded [55], reinforcement should be included such as co-winding thin stainless steel tapes with the superconductor[7,14,17,44,56,57], reinforcing sections of the magnet [58] or a support structure around the outside of the magnet[46,58]. Fibre reinforced plastic (FRP) sheets are frequently used to insulate and reinforce the magnet in the axial direction[6,7,44]. Estimates of the maximum stress produced in our magnet are around 150 kPa, much less than typical fracture /

	Epoxy resin [46]	Tufnol (Carp)†	Polyimide [59]	Bi-2223/Ag [60]
Thermal contraction at 4.2 K (%)	1.1	0.57	0.9	0.25
Yield / fracture stress (MPa)	140	105*	155	-

Table 9.3. Mechanical properties of constituent materials of the Bi-2223 magnet. * denotes room temperature. † denotes manufacturer specification.

yield stresses of constituent materials (listed in Table 9.3). Typically no additional reinforcement is required for properly impregnated laboratory scale magnets.

Coils were stacked and glued together to form the magnet using the Ciba-Geigy room temperature curing system CY1300 (resin), HY1300 (hardener) mixed in the ratio 3 : 1 by weight. Joints between the coils were soft soldered using Bi-2223 tape. Although sophisticated jointing techniques have been developed, this is rarely necessary in small magnet systems [32,49]. The magnet was supported between two non-magnetic stainless steel plates (brass is equally good) using four support rods. A top plate was connected above the top support plate with 24 voltage terminals, to allow the voltage across any pancake to be measured. Current access to all coils was also provided via 7 current terminals on the top plate electrically connected to the coils with Bi-2223 tape which allowed any coil to be individually energised as well as the entire magnet. The dimensions of the Bi-2223 magnet are presented in Table 9.4 and a photo shown in Fig. 9.5.

9.3.2. External Components

Copper current leads were used from the top of the cryostat to the magnet current terminals. The large heat leak to the system due to the copper leads was considered acceptable during the 8 day testing period. Optimised permanent current leads are

Figure 9.5. Photo of the 1.29 T Bi-2223 magnet.

Bore (mm)	40
Magnet winding I/D (mm)	44
Magnet winding O/D (mm)	82
Magnet height (mm)	57.5
Number of double pancakes	6
Length of Bi-2223 tape (m)	103.1
Magnet packing factor (%)	58
Central bore field constant (mTA^{-1})	8.18
Maximum field constant (mTA^{-1})	8.85

Table 9.4. Dimensions and characteristic properties of the Bi-2223 magnet.

typically fabricated from tubes of brass with a current density x length product of 1.5 x10^6 Am^{-1} for operating at 4.2 K and 6 x10^6 Am^{-1} at 77K [46,60,61].

Quench protection is an essential component in large superconducting magnets because of the large potential energy stored when energised (~1 - 10 MJ). Critical parameters include the maximum temperature (θ_{MAX}) and the maximum voltage (V_{MAX}) together with the characteristic decay time for the current decay following a quench. A maximum temperature of 100 K is normally considered safe enough to ensure that the local expansion in the region of the (hot) quench does not damage the windings, although 500 K can be tolerated in some systems without mechanical damage or the insulation or resin melting. The breakdown voltage for polyimide is 120 kV.mm^{-1} and for polymer resins is typically tens of kV.mm^{-1}. The basic approach to protecting a large magnet if θ_{MAX} or V_{MAX} are too large is to subdivide the magnet. Choices include active and passive systems either within or outside the cryostat[46,62]. Basic calculations suggest that no sub-division (and protection) is required if the magnet, as is the case here, consists of less than 2 km of wire or tape[19].

The inclusion of iron pole pieces[63,64] or copper coils[65] has been shown to reduce the magnitude of the radial field component in the outer coils and therefore increase the field produced by the magnet. This approach is only applicable for low field systems where the iron does not saturate. It has been suggested that the maximum radial component may be reduced by ~ 40 % [64]. Calculations suggest that such a reduction may have produced up to ~ 15 % increase in maximum field.

9.4 Performance of coils and magnet

After each coil was fabricated, it was tested at 77 K to identify any damage of electrical problems. The I_c values obtained after initial cool-down using 1.5 μV.cm^{-1} criterion are presented in Table 9.5. There is relatively large variation from coil to coil primarily because the number of turns and geometry of the coils are not the same. In addition after the first pancake of a coil is tested, subsequent measurements on the second pancake and joints are affected by remnant field and possibly because the coil had not cooled back to 77 K. However, since these "quality control" experiments showed that there were no pancakes which had been seriously damaged, all coils were stacked to form the magnet.

E-J measurements were taken for each coil when individually energised (to identify any damaged pancakes) at 4.2 K and 77 K (not shown), with the whole magnet energised and with the magnet energised in a background field at 4.2 K and 77 K. The background field of 296 mT at 4.2 K and 40 mT at 77 K was provided using a large bore Bi-2223 system which has been previously reported [66]. Comparing the I_C values for any pairs of pancakes in a given coil when individually energised, one finds that for Tape 1 the variation in I_c is ~ 7 % and Tape 2 is ~ 5 %. These variations are consistent with long-length variations in I_C in the original tape of up to ~ 10%.

The *E-J* characteristics obtained from Coil 1 individually energised at 4.2 K and its component pancakes are presented in Fig. 9.6 and for Coil 5 with the whole magnet energised at 4.2 K in Fig. 9.7. In both cases the baselines are flat (consistent with the short sample data in Fig. 9.2), the superconducting joint resistance remains low for $I < I_c$ and the *E-J* characteristics of the whole coil is the sum of the pancakes and connecting joint. When the whole magnet is energised, the top and bottom coils exhibit the lowest I_c at both 4.2 (90 and 92 A) and 77 K (12.6 and 11.7 A) consistent with other work in the literature [65-67]. Typical joint resistances between pancakes are below 2 μΩ at 100 A at 4.2 K. The I_c of the magnet in self-field was measured to be 104 A at 4.2 K and 12.8 A at 77 K.

The axial field profile along the central bore axis was measured using a Hall probe at room temperature with the magnet energised at 1.0 A. The field profile within the magnet was calculated to high precision by taking into account the precise number of turns on each pancake, the packing factor and the position and geometry of each pancake [68]. In Fig. 9.8, the excellent agreement found between the calculated and measured profiles provides evidence that there are no short circuited turns within the magnet. The measured maximum field constant of 8.18 mT.A^{-1} at 4.2 K and 8.20

	Coil 1 (top)			Coil 2			Coil 3			Coil 4			Coil 5			Coil 6 (bottom)		
Pancake	lower	upper	whole	lower	upper	whole	lower	upper	whole	lower	upper	whole	lower	upper	whole	lower	upper	whole
4.2 K I_c for individually energised coils (A)	115	123	124	120	127	127	115	103	111	104	108	105	130	128	130	123	120	-
n-index	14.7	20.0	-	16.7	16.7	-	16.1	14.9	-	15.2	17.3	-	16.3	15.9	-	15.1	15.3	-
I_c for magnet energised (A)	99	90	95	112	110	111	-	110	114	107	117	110	107	115	111	92	100	94
I_c for whole magnet energised in 296 mT background field (A)	96	88	95	109	109	109	119	106	113	107	117	112	108	115	109	88	97	95
77 K I_c for individually energised coils (A)	18.3	14.9	15.8	20.1	16.4	17.2	19.1	13.7	14.8	17.7	14.7	15.3	19.2	16.0	16.9	17.5	15.3	16.0
n-index	9.7	9.0	8.6	10.5	10.2	9.2	10.5	10.3	9.8	11.5	11.3	10.9	10.3	10.3	9.6	9.8	9.1	9.1
I_c for whole magnet energised (A)	13.5	12.6	13.3	16.0	15.2	15.8	17.9	15.7	16.5	15.3	17.6	15.8	14.7	16.1	15.9	11.7	14.0	12.5
I_c for magnet energised in 40 mT background field (A)	12.7	12.2	12.6	15.3	14.6	14.8	16.7	14.9	15.4	14.6	16.3	15.0	14.0	15.5	14.7	11.3	13.0	12.1

Table 9.5. I_C test results of all constituent pancakes and coils of the Bi-2223 magnet at 4.2 and 77 K. At 77K, each coil was individually energised and tested before stacking whereas at 4.2 K the equivalent measurement was taken after stacking. The electric field criterion used for I_c was 1.5 μV.cm^{-1}.

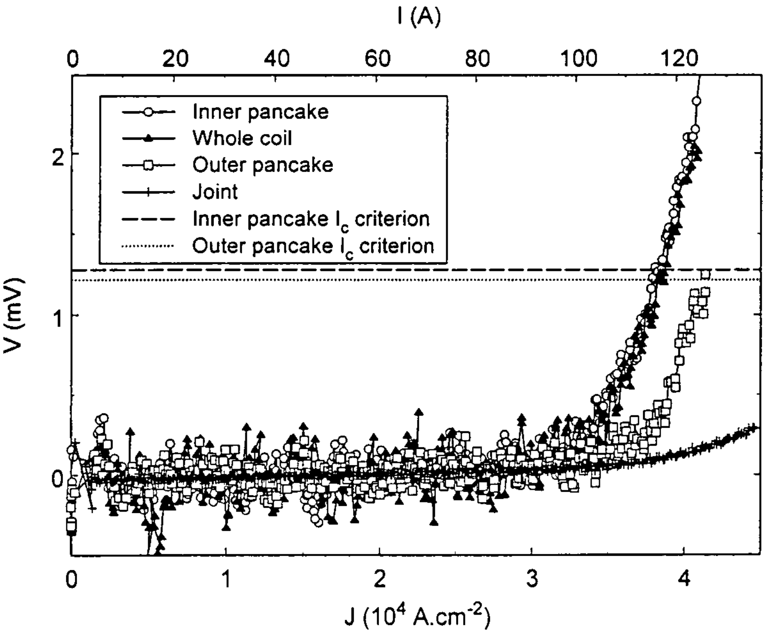

Figure 9.6. Electric field - current density characteristics of the components of Coil 1 with the coil individually energised at 4.2 K.

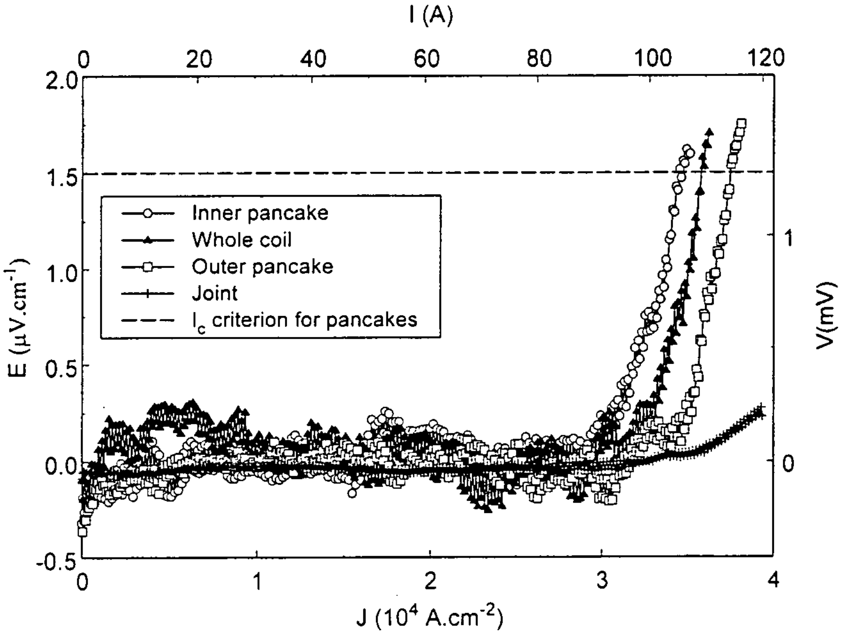

Figure 9.7. Electric field - current density characteristics of the components of Coil 5 with the whole magnet energised at 4.2 K.

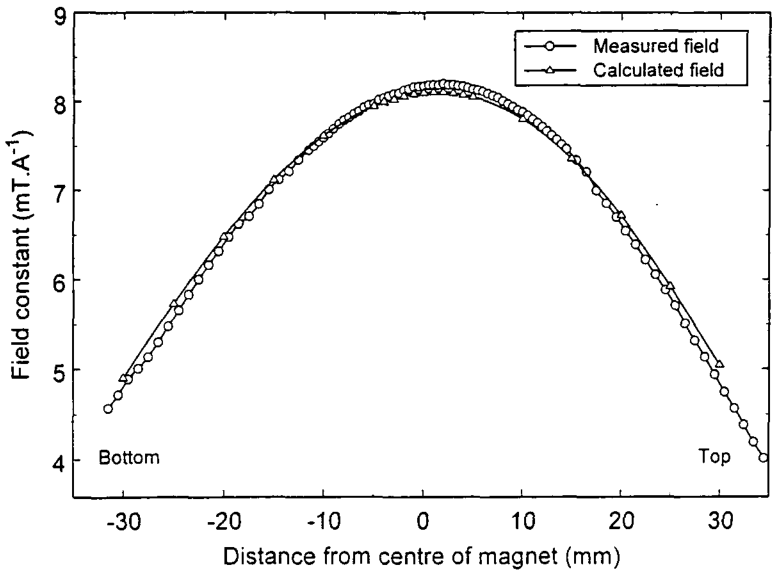

Figure 9.8. Comparison between measured and calculated axial field profile within the Bi-2223 magnet.

mT.A^{-1} at room temperature agree to better than 1 % with the calculated value of 8.11 mT.A^{-1}. The axial field is homogeneous to ~ 1.5 % over 1 cm about the centre.

The optimum shape for small magnets is a (well-documented) compromise between the magnitude of the field produced, the homogeneity of the magnetic field profile and the length of conductor [46]. A coil that has a minimum weight of wire for a given field will produce a homogeneity of ~ 1 part in 10^3 over a 1 cm diameter sphere volume. For higher homogeneity up to 1 part in 10^5, notch, compensation or shim coils may be added [19,69]. The maximum magnet constant for our magnet is calculated as 8.85 mT.A^{-1}, positioned on the inner winding at 2 mm above the centre. This maximum is offset from the centre due to the asymmetry of the number of turns. The maximum current passed through the magnet in self-field was 146 A at 4.2 K, limited by a 10 V power supply, corresponding to a maximum bore field of 1.19 T and a maximum magnet field on the turns of 1.29 T. In a background field at

4.2 K the maximum measured bore field was 1.470 T (including 296 mT contribution from the large bore magnet).

9.5. Calculations of magnet performance

The I_c of any turn in any pancake is determined by the local angle and magnitude of the magnetic field and the local strain state. The magnitude and direction of field throughout the magnet has been calculated using standard formulae. The field profile of the magnet was generated using the precise dimensions of each coil. The geometry and number of turns of Coil 2 was used in calculations for the individually energised coils. The strain state was calculated from the bending radius.

It is a very large experimental task to determine the magnetic field, temperature and strain dependence of J_C for a short sample. To approximate the functional form of J_C over the required range, we have chosen to linearly interpolate the variable magnetic field J_C data in Fig. 9.3 obtained at two different orientations of the field and two different strains. Comparison with the literature shows that these interpolations give a reasonable first approximation to the observed Bi-2223 J_c dependence on strain[27-30] and angle[20-26] as discussed in Section 9.6.

The positions of the turns with the lowest I_c (i.e. the performance limiting turn) were identified at r = 36 mm (105 A) for the individually energised coils and on the top and bottom pancake at r = 38 mm (94 A) for the fully energised magnet. The J_c dependencies and corresponding load lines for the performance limiting turns are presented in Fig. 9.9. The change in the normalised current density within the top pancake when the magnet is energised is presented in Fig. 9.10 where calculations for J_C were made at 2 mm intervals radially along the pancake. The change in magnitude and direction of field experienced by the turns are presented in the same figure. On moving radially outwards from the bore the magnitude of field decreases by 50 %, the strain decreases by 45 % and the angle of field becomes more closely aligned with the c-axis of the tape by 60^0. The combined effect of these factors results in only a 10 % variation in I_c across the pancake. The calculated I_c of the top

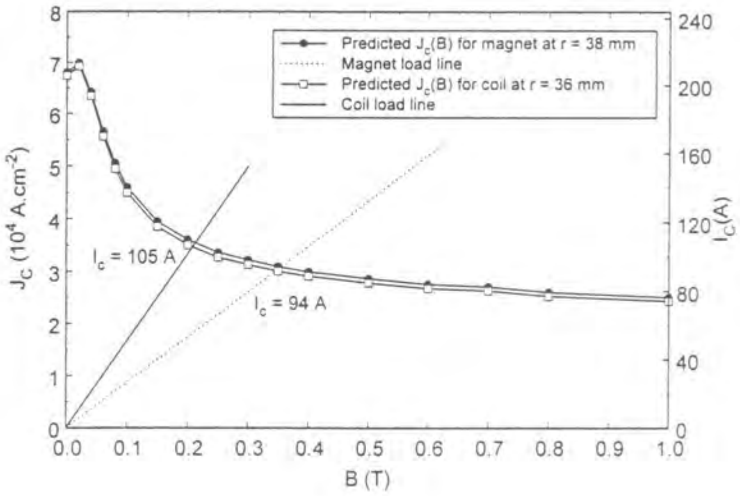

Figure 9.9. The field dependence of the critical current density calculated for the turn at r = 36 mm in an individually energised coil and for the turn at r = 38 mm on the outermost pancake with the magnet energised. The associated load lines are also shown.

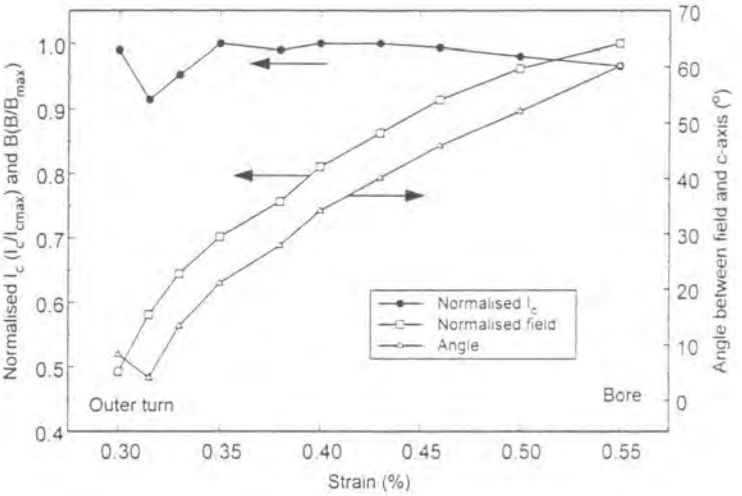

Figure 9.10. The change in the normalised critical current (•), normalised magnetic field (□) and angle of field (Δ) from the c-axis as a function of strain for turns across the outermost pancake with the magnet energised. I_c is normalised to the value of the turn with $\varepsilon = 0.35$ % and the field is normalised to the field experienced by the inner turn.

pancake is 94 A. Above 94 A, heat will start to be generated locally. An average value of $I_C(av)$ for the pancakes has also been calculated using a length average defined by $I_C(av)=\sum I_c l/\sum l$ where l is a length of tape with a particular I_c. For an individually energised coil $I_C(av)$ is 115 A and with the magnet energised I_c(av) across the top pancake is 101 A. The measured I_c values of 90 and 92 A for the top and bottom pancakes with the magnet energised (c.f. Table 9.5) are in very good agreement calculated value of 94 A.

The performance of the magnet has also been calculated assuming a W+R approach had been used. Necessarily, there is no degradation in the tape performance due to strain. In the case of the individually energised coil, the performance limiting turn is positioned at r = 36 mm with an I_c value of 133 A. With the magnet energised, the performance limiting turn is positioned at r = 38 mm on the outermost pancake with an I_c of 117 A. Hence the maximum field could be increased by ~ 20 %.

9.6. Discussion

We estimate the uncertainty in the predicted J_c due to the anisotropy and field interpolation to be less than ~ 5 % since the field at the performance limiting turn is aligned with the c-axis to ~ 5 degrees (c.f. Fig. 9.10). The interpolation to determine the strain dependence of J_c within the magnet is more complex. Our experience measuring the strain dependence of J_c in brittle Bi-2223 tapes is that there is considerable statistical variation in short sample measurements [70], probably because of the variation in porosity of the tapes along their length [10]. It is therefore difficult to obtain variable strain short sample data that are representative of long lengths. Nevertheless, in light of the ~ 10% variation in I_c over long lengths in the tapes and the ~20 % degradation in I_c due to strain intrinsic to the R+W technique, there is very good agreement between the calculations and the final magnet performance. We conclude that a reliable fabrication process has been developed for laboratory scale magnets which produces minimal additional damage due to handling.

We suggest fabrication of a laboratory scale magnet as follows; measure J_c of the tape as a function of field with the field applied parallel and orthogonal to the tape surface in the unstrained state and at the strain state equal to that on the bore of the proposed magnet; measure J_c after many thermal cycles to ensure no degradation occurs; calculate the performance of the proposed magnet; if necessary a third interpolation point can be obtained on a short sample as a function of field at the strain state and orientation of magnetic field for the turn with the lowest I_c and the expected performance of the magnet double-checked; construct the coils; test the coils in self-field at 77 K and replace any damaged ones; finally stack the coils to form the magnet.

9.7. Conclusions

In this chapter, the design and fabrication of a 1.29 T laboratory sized Bi-2223 magnet operating at 4.2 K has been described. The magnet was fabricated from 6 resin impregnated double wound pancakes of inner diameter 40 mm wound via the react-and-wind route using Bi-2223/Ag tape with critical current density 8.3 x 10^4 A.cm^{-2} (4.2 K, 0 T). Design considerations actually used and other possible options in fabricating a similar sized magnet with different operational requirements or restrictions have been discussed.

The measured performance of the magnet and all constituent coils has been compared with calculated values obtained using field profile calculations and short sample J_C data. Good agreement between calculation and experiment has been found which show that the top and bottom pancakes limit the performance of the magnet. The performance of the magnet is reduced by ~ 20 % due to the strain on the superconductor produced during the R+W technique. We conclude that a reliable fabrication technique has been described for the non-specialist to produce a R+W High Temperature Superconducting Laboratory scale magnet.

References for Chapter 9

[1] Bednorz J and Muller K 1986 *Z. Phys. B - Condensed Matter* **64** 189-193

[2] Wu M, Ashburn J, Torng C, Hor P, Meng R, Gao L, Huang Z, Wang Y, and Chu C 1987 *Phys. Rev. Lett.* **58** 908-910

[3] Li Q, Brodersen K, Hjuler H, and Freltoft T 1993 *Physica C* **217** 360-366

[4] Malozemoff A, Carter W, Fleshler S, Fritzemeier L, Li Q, Masur L, Miles P, Parker D, Parrella R, Podtburg E, Riley G, Rupich M, Scudiere J, and Zhang W 1999 *IEEE Transactions on Applied Superconductivity* **9** 2469-2474

[5] Balachandran U, Iyer A, Jammy R, Chudzik M, Lelovic M, Krishnaraj P, Eror N, and Haldar P 1997 *IEEE Transactions on Applied Superconductivity* **7** 2207-2210

[6] Zeng R, Lui H, Beales T, and Dou S 1999 *IEEE Transactions on Applied Superconductivity* **9** 2605-2608

[7] Ohkura K, Sato K, Ueyama M, Fujikami J, and Iwasa Y 1995 *Applied Physics Letters* **67** 1923-1925

[8] Kaneko T, Hikata T U, M., Mikumo A, Ayai N, Kobayashi S, Saga N, Hayashi K, Ohmatsu K, and Sato K 1999 *IEEE Transactions on Applied Superconductivity* **9** 2465-2468

[9] Leghissa M, Fischer B, Roas B, Jenovelis A, Wiezoreck J, Kautz S, Neumuller H, Reimann C, Nanke R, and Muller P 1997 *IEEE Transactions on Applied Superconductivity* **7** 355-358

[10] Larbalestier D and Lee P 1999 *Proceedings of the 1999 Particle Accelerator Conference* 177-181

[11] Sneary A, Friend C, Vallier J, and Hampshire D 1999 *IEEE Transactions on Applied Superconductivity* **9** 2585-2588

[12] Sato K, Hikata T, and Iwasa Y 1990 *Applied Physics Letters* **57** 1928-1929

[13] Snitchler G, Kaksi S, Manlief M, Schwall R, Sid-Yekhlef A, Ige S, Medeiros R, Francavilla T, and Gubser D 1999 *IEEE Transactions on Applied Superconductivity* **9** 553-558

[14] Sato K, Kato T, Ohkura K, Kobayashi S, Fujino K, Ohmatsu K, and Hayashi K 2000 *Superconductor Science and Technology* **13** 18-22

[15] Zeng R, Zhou Y, Hua P, Fu X, Ye B, Zhou M, Yuan G, Lui H, and Dou S 1998 *Superconductor Science and Technology* **11** 535-539

[16] Kumakura H, Kitaguchi H, Togano K, Wada H, Ohkura K, Ueyama M, Hayashi K, and Sato K 1998 *Cryogenics* **38** 639-643

[17] Verges P, Fischer K, Hutten A, and Fuchs G 1998 *Cryogenics* **38** 607-611

[18] Tomita N, Arai M, Yanagisawa E, Morimoto T, Kitaguchi H, Kumakura H, Togano K, and Nomura K 1996 *Cryogenics* **36** 485-490

[19] Kerley N, in *Handbook of applied superconductivity*; *Vol. 2*, edited by B. Seeber (IOP Publishing Ltd., 1998), p. 1067-1089.

[20] Rabara M, Takeuchi T, and Miya K 1999 *Physica C* **313** 213-218

[21] Oota A and Tanaka M 1996 *Physica C* **268** 295-299

[22] Fuller-Mora W 1996 *Physical Review B* **54** 11977-11980

[23] Han G, Han H, Wang Z, Wang S, Wang F, Yuan W, and Chen J 1994 *Cryogenics* **34** 613-616

[24] Hensel B, Grivel J, Jeremie A, Lerin A, Pollini A, and Flukiger R 1993 *Physica C* **205** 329-337

[25] Hu Q, Weber H, Lui H, Dou S, and Neumuller H 1995 *Physica C* **252** 211-220

[26] Kovak P, Husek I, Rosova A, and Pachla W 1999 *Physica C* **312** 179-190

[27] Ekin J, Finnemore D, Li. Q, Tenbrink J, and Carter W 1992 *Applied Physics Letters* **61** 858-860

[28] Polak M, Parrell J, Polyanskii A, Pashitski A, and Larbalestier D 1997 *Applied Physics Letters* **70** 1034-1036

[29] Suenga M, Fukumoto Y, Haldar P, Thurston T, and Wildgruber U 1995 *Applied Physics Letters* **67** 3025-3027

[30] Huang Y, ten Haken B, and ten Kate H 1999 *IEEE Transactions on Applied Superconductivity* **9** 2702-2705

[31] Kovac P, Cesnak L, Melisek T, Husek I, Bukva P, Pitel J, Kopera L, Pachla W, and Bucholtz W 1999 *Superconductor Science and Technology* **12** 507-513

[32] Vo N 1998 *Journal of Magnetism and Magnetic Materials* **188** 145-152

[33] Newson M, Ryan D, Wilson M, and Jones H 2000 *IEEE Transactions on Applied Superconductivity* **10** 468-471

[34] Hellstrom E, in *High-temperature superconducting materials science and engineering*, edited by D. Shi (Elsevier Science Ltd., 1995), p. 383-440.

[35] Dou S and Liu H 1993 *Superconductor Science and Technology* **6** 297-314

[36] Flukiger R, Graf T, Decroux M, Groth C, and Yamada Y 1991 *IEEE Transactions on Applied Superconductivity* **27** 1258-1263

[37] Grasso G, Jeremie A, and Flukiger R 1995 *Superconductor Science and Technology* **8** 827-832

[38] Marti F, Grasso G, Grivel J-C, and Flukiger R 1998 *Superconductor Science and Technology* **11** 485-495

[39] Zeng R, Beales T, Lui H, and Dou S 1998 *Superconductor Science and Technology* **11** 299-303

[40] Han Z, Skov-Hansen P, and Freltoft T 1997 *Superconductor Science and Technology* **10** 371-387

[41] Vo N, Willis J, Peterson D, Liu H, and Dou S 1998 *Physica C* **299** 315-326

[42] Picard J, Zouiti M, Livillain C, Wilson M, Ryan D, Marken K, Herrmann P, Beghin E, Verhaege T, Parasie Y, Bock J, Baecker M, Perenboom J, and Paasi J 1999 *IEEE Transactions on Applied Superconductivity* **9** 535-540

[43] Yang M, Goringe M, Grovenor C, Jenkins R, and Jones H 1994 *Superconductor Science and Technology* **7** 378-388

[44] Ohmatsu K, Hahakura S, Kato T, Fujino T, Ohkura K, and Sato K 1999 *IEEE Transactions on Applied Superconductivity* **9** 924-927

[45] Tupper M, Fabian P, and Beavers F 2000 *IEEE Transactions on Applied Superconductivity* **10** 1350-1353

[46] Wilson M, *Superconducting Magnets* (Oxford University Press Inc., New York, 1998).

[47] Celic E, Mutlu I, Avci E, and Hascicek Y 2000 *IEEE Transactions on Applied Superconductivity* **10** 1329-1332

[48] Celic E, Mutlu I, and Hascicek Y 2000 *IEEE Transactions on Applied Superconductivity* **10** 1341-1344

[49] Collings E, *Applied Superconductivity, Metallurgy and Physics of Titanium Alloys*, Vol. 2 (Plenum Press, New York, 1986).

[50] Evans D and Morgan J, in *Cryogenic Engineering*, edited by B. Hands (Academic Press Inc., London, 1986), p. 271-292.

[51] Lee H and Neville K, *Handbook of Epoxy Resins* (McGraw-Hill Inc., 1982).

[52] Baldan C, Shigue C, and Filho E 2000 *IEEE Transaction s on Applied Superconductivity* **10** 1347-1349

[53] Jones H and Hickman A 2000 *IEEE Transactions on Applied Superconductivity* **10** 1345-1346

[54] Brennan A, Miller T, Arnold J, Huang K, Gephart N, and Markewicz W 1995 *Cryogenics* **35** 783-785

[55] Hands B, in *Cryogenic Engineering*, edited by B. Hands (Academic Press Inc., London, 1986), p. 241-270.

[56] Sakuraba J, Mikami Y, Watazawa K, Watanabe K, and Awaji S 2000 *Superconductor Science and Technology* **13** 12-17

[57] Kitaguchi H, Kumakura H, Togano K, Okada M, Tanaka K, and Sato J 1998 *Cryogenics* **38** 181-186

[58] Jones H, Van Cleemput M, Hickman A, Ryan D, and Saleh P 1998 *Physica B* **246-247** 337-340

[59] Gerhold J, in *Handbook of Applied Superconductivity*; *Vol. 1*, edited by B. Seeber (IOP Publishing Ltd., London, 1998), p. 1121-1137.

[60] Keys S and Hampshire D, in *Handbook of Applied Superconductivity* (IOP Publishing Ltd., London, to be published).

[61] Herrmann P, in *Handbook of Applied Superconductivity*; *Vol. 1*, edited by B. Seeber (IOP Publishing Ltd., London, 1998), p. 801-843.

[62] Meb K, in *Handbook of Applied Superconductivity*; *Vol. 1*, edited by B. Seeber (IOP Publishing Ltd., London, 1998), p. 527-555.

[63] Selvaggi J, Mathewson W, Laughman R, Francavilla T, Gubser D, and Miller M 1996 *Cryogenics* **36** 555-558

[64] Fabbricatore P, Priano C, Testa M, Musenich R, Kovac P, Martone A, Petrillo E, and Ariante M 1998 *Superconductor Science and Technology* **11** 304-310

[65] Pitel J and Kovac P 1997 *Superconductor Science and Technology* **10** 847-852

[66] Sneary A, Friend C, Richens P, Jones H, and Hampshire D 1999 *IEEE Transactions on Applied Superconductivity* **9** 936-939

[67] Daumling M and Flukiger R 1995 *Cryogenics* **35** 867-870

[68] Montgomery D, *Solenoid Magnet Design* (John Wiley and Sons, Inc., 1969).

[69] Tschopp W and Laukien D, in *Handbook of applied superconductivity*; *Vol. 2*, edited by B. Seeber (IOP Publishing Ltd., 1998), p. 1191-1212.

[70] Hamid H and Hampshire D 1998 *Cryogenics* **38** 1007-1015

Chapter 10

Future Work

Future work in this area should be directed towards measuring the transport properties of single filaments from the Bi-2223 tapes. In particular, effort should be put into extracting filaments from the centre regions of the tapes reported to carry up to 10 × the current of the outer filaments. The calculations in Chapter 6 suggest that these filaments may perform close to equivalent thin film values. There is little data on single filaments in the literature possibly because of the many problems associated with the sample preparation. However these measurements may be the most critical measurement in identifying the mechanisms limiting J_c in the polycrystalline tapes. The tape measurements are affected by the shunt resistance and single crystals and films do not represent industrially 'useful' forms of the material. The statistics of successful sample preparation are low using the techniques described in Chapter 5 however the technique of heating the samples before making contacts took a step towards increasing the probability of a low resistance contact. A further improvement may be to heat the sample during gold contacting. Another improvement may be to use the more robust silver epoxy for contacts. Silver paint was used since it ran around the sample to optimise the contact but if the heated gold can produce low resistance contacts to the sample, the epoxy may be more reliable during thermal cycling. Using the VTI / high field magnet system in place in Durham, currents from tens of nA up to hundreds of mA could be measured in fields up to 15 T in accurate temperatures up to T_c. $J_c(B,T)$ measurements within these ranges could accurately measure the decrease in J_c towards B_{c2} and possibly take a step towards distinguishing between the pinning mechanisms. The change in curvature observed in the c-axis orientated *E-J* filament characteristics in Chapter 5 should definitely be investigated further. Measurements should be taken close to the melting line at different temperatures and fields over many orders of magnitude in current and voltage to investigate this further.

The most comprehensive of $J_c(B,T)$ data sets reported has been presented in Chapter 4 but is unable to distinguish pinning models. Although the data are extremely attractive to magnet manufacturers unless the J_c performance of the tapes can be increased by about a factor 5 I feel nothing new will be concluded about the pinning mechanisms in the tapes from pursuing these measurements.

The react and wind magnet project has been successfully completed and the laboratory scale technology is now firmly in place. The next step would be to build a magnet of size around 5 T to compete with the largest magnets on the international stage. Although possible with the expertise gained through this thesis a project of that magnitude would require more manpower and is probably better placed in industry than the research laboratory. A wind and react project may be useful to the group for fabrication of inserts, however this technology is becoming increasingly established and would not offer anything new to the international community.

Appendix 1 Publications

1. Design, fabrication and performance of a 1.29 T Bi-2223 magnet system
   Sneary AB, Friend CM and Hampshire DP
   Submitted for publication in Superconductor Science and Technology

2. The Useful Limit for the Critical Current Density in Bi-2223 tapes
   Sneary AB and Hampshire DP
   To be submitted to Superconductor Science and Technology

3. Development of High Temperature Superconducting Coils Using Bi-2223/Ag tapes
   Sneary AB, Friend CM, Richens P, Jones H and Hampshire DP
   IEEE Transactions on Applied Superconductivity **9** 936-939 (1999)

4. Critical Current Density of Bi-2223/Ag Multifilamentary Tapes from 4.2 K up to 90 K in Magnetic Fields up to 23 T
   Sneary AB, Friend CM, Vallier JC, and Hampshire DP
   IEEE Transactions on Applied Superconductivity **9** 2585-2588 (1999)

Appendix 2 Conferences and Courses

Conferences Attended

April 2000	University of Birmingham	Superconductivity meeting
December 1999	University of Leicester	CMMP 99
April 2000	University of Birmingham	Superconductivity meeting
September 1998	Palm Springs, California	ASC 98

Courses Attended

1999	CRAC Research Councils' Graduate Schools Programme
2000	Maple V for beginners (Durham University ITS)
1998	Mechanical workshop course (Durham University)
1997	Low temperature techniques course (Aston University)

Appendix 3 Computer programs

Maple V

Jc(B,T,theta).mws	Generates the angular dependence of J_c for a thin film in Chapter 6.
mapsoln(B)2.mws	All the $J_c(B,T)$ predictions for the curved film model in Chapter 6 were generated using this program.
inmag.mws	This program was used to calculate the field profile within the coils and magnets.

ASYST V-I programs

120trace.abs, 120trace.var

> V-I characteristics were measured up to 120 A using the Oxford Instruments IPS and the Keithley 182 nanovoltmeter.

120field.abs, 120field.var

> V-I characteristics at varying field up to 120 A using the Oxford Instruments IPS and the Keithley 182 nanovoltmeter.

500trace.sk1, 500trace.var

> V-I characteristics up to 500 A. The voltage output from the Oxford Instruments IPS is used to ramp the 500 A supply.

500field.sk1, 500trace.var

> V-I characteristics at varying field up to 500 A. The voltage output from the Oxford Instruments IPS is used to ramp the 500 A supply.

FILGLASS.ABS

V-I characteristics for single filament experiments. Current is automatically ramped using Glassman power supply. Voltage read across Keithley 182 nanovoltmeter.

FIL_TR_1.ABS

V-I characteristics for single filament experiments. Current is manually ramped current using Glassman power supply.